Universiteit Leiden
The Netherlands

H0 from first principles

Reichel, Valentin

Citation
Reichel, V. (2026). *H0 from first principles*.

Version:	Not Applicable (or Unknown)
License:	License to inclusion and publication of a Bachelor or Master Thesis, 2023
Downloaded from:	https://hdl.handle.net/1887/4262180

Note: To cite this publication please use the final published version (if applicable).

H_0 from first principles

Thesis

submitted in partial fulfillment of the
requirements for the degree of

Master of Science
in
Physics

Author :	Valentin Reichel
Student ID :	4101456
Supervisor :	Prof. Dr. Alessandra Silvestri
External Supervisor:	Dr. Fabrizio Renzi
Second corrector :	Prof. Dr. Henk Hoekstra

Leiden, The Netherlands, August 31, 2025

H_0 from first principles

Valentin Reichel

Instituut-Lorentz, Leiden University
P.O. Box 9500, 2300 RA Leiden, The Netherlands

August 31, 2025

Abstract

The Hubble constant, H_0, sets the absolute scale for distances and ages in our Universe, yet its precise value remains debated, as local measurements and indirect approaches do not agree at a significant level. This thesis develops the idea by Renzi and Silvestri [2023] for a calibration-free and model-independent framework for estimating H_0 directly from cosmological observations. The analysis combines uncalibrated Type Ia supernovae from the Pantheon+ and DES-SN 5YR samples, unanchored baryon acoustic oscillation (BAO) data from SDSS and DESI, and 33 cosmic chronometer measurements for a model independent estimate of the expansion rate. Combining this data using the distance-duality relation, yields a direct measurement of the absolute magnitude of the supernovae, which can be compared to the locally calibrated value. Assuming an FLRW expansion at low redshift this magnitude can than be transferred into a measure of H_0. Gaussian process regression is used to non-parametrically reconstruct both the supernova magnitude-redshift relation and the cosmic expansion history from chronometers. In this way, no assumptions about a cosmological model, the sound horizon, or local distance calibration are required. The reconstructed $H(z)$ from chronometers agrees with ΛCDM within 1σ across $0 \lesssim z \lesssim 2.5$, and angular diameter distances obtained from the combination of BAO and CC are mutually consistent across all datasets. The results for Pantheon+ and DES-SN 5YR supernovae are statistically compatible, but exhibit a systematic offset in apparent magnitudes that propagates into a catalog difference of $\Delta M_B \simeq -0.04\,\mathrm{mag}$, with Pantheon+ being brighter. The difference in magnitudes leads to a $\sim 2\%$ shift in the inferred H_0, with DES being higher. The resulting absolute magnitudes, $M_B \simeq -19.36$ to $-19.42\,\mathrm{mag}$, are consistent with the required magnitude from the inverse distance ladder and are in 2-3% tension with the locally calibrated magnitude from SH0ES. Since this framework excludes systematics of the distance ladder itself, the remain-

ing source of systematic uncertainty is primarily the supernova calibration. In light of other local probes, which give $h \sim 0.73$, that do not depend on M_B, the discrepancy is more plausibly interpreted as a systematic offset of the entire local distance ladder at low redshift. Furthermore, these findings limit the explanatory power of early-universe solutions to the Hubble tension, since the purely data driven M_B is consistent with the indirect distance ladder (i.e. with the ΛCDM sound horizon), raising H_0 by altering the sound horizon cannot explain the full set of data. Across dataset combinations the joint likelihood analysis yields $H_0 \simeq 66.5$-$68.5\ \mathrm{km\,s^{-1}\,Mpc^{-1}}$ with 2.0-2.7% precision, and $q_0 \simeq -0.57 \pm 0.08$.

Acknowledgments

I am especially grateful to Fabrizio Renzi and Alessandra Silvestri for their many insightful comments, stimulating discussions, and the valuable lessons I have learned from them. I would also like to thank Adrianna Favale, Gen Ye, Sofie Marie Koksbang, Daniela Grandón Silva, and Henk Hoekstra for their helpful feedback and inspiring ideas.

Contents

1 Introduction **1**

2 Geometry & Cosmography of the Expanding Universe **3**
2.1 FLRW Space-Time and Kinematics 3
2.2 Redshift 4
2.3 Cosmological Distance Measures 5
2.3.1 Radial Null Geodesic and the Line-of-Sight Comoving Distance 6
2.3.2 Transverse (or Proper Motion) Comoving Distance 7
2.3.3 Angular Diameter Distance 8
2.3.4 Luminosity Distance 9
2.4 Apparent Magnitude and Distance Modulus 12
2.4.1 Snapshot of the Modern Distance Ladder 13
2.5 Etherington's Distance-Duality Relation 15
2.6 Low-Redshift Cosmography 17

3 Chasing H_0 **20**
3.1 Origins and Interpretations of H_0 20
3.2 Measuring H_0 22
3.2.1 Direct Measurements using the Distance Ladder 22
3.2.2 Inverse Distance Ladder: Sound Horizon Based H_0 Measurements 29
3.2.3 One-Step Methods towards H_0 31
3.3 Measured values of H_0 and the Hubble Tension 39
3.4 Resolutions to the Tension 43
3.4.1 Experimental/Methodological Approaches 44
3.4.2 Theoretical Solutions 48

4 Measuring H_0 from first principles **55**

5 Data sets **59**
5.1 BAO 59
5.2 Cosmic Chronometer 61
5.3 SNe Ia 64

6 Gaussian Processes **66**
6.1 Fundamentals 66
6.1.1 Prior and Likelihood 66
6.1.2 Posterior and Predictions 67
6.1.3 Kernels 68
6.2 Kernel Optimization: Objective Functions 69
6.2.1 Log Marginal Likelihood (LML) Method 69
6.2.2 Gaussian Process Monte Carlo (GPMC) 70
6.3 Implementation 74
6.3.1 Choice of Method 74
6.3.2 Kernel selection 75
6.4 Changes in Methodology 81

7 Results and Discussion **82**
7.1 Results of this Work 82
7.2 Comparison to Similar Methodologies 96
7.3 Connection to the Hubble Tension 97

8 Conclusion **100**

1 Introduction

> ”Night is an element of love; like fog. It liberates space, lets freshness cross it... With or without stars and galaxies, the sky becomes a private territory - the imagination’s own scope.”
> — Etel Adnan in *The Cost for Love We are Not Willing to Pay*

This image of the sky as a private territory reminds us that the cosmos, though vast, touches our imagination intimately. To enter the night is to be reminded of the depth of the universe and of our own fragility within it. To understand the cosmos is a way of understanding parts of ourselves: our curiosity, our place within that expanse, and the tools we use to trace its contours.

Adnan’s words evoke a space where immensities and intimacies meet. The sky is not only an expanse of stars and galaxies, but also a terrain of thought and memory, a field where imagination confronts reality. Cosmology grows out of this same tension: the universe appears immense and unreachable, yet it soaks into our most immediate experience, compelling us to measure, to compare, and to weave fragments of light into a coherent map of our world.

Since the earliest measurements of the Earth and the Moon, our horizon has steadily expanded, first to the Sun and the planets, then to the stars, to other galaxies and eventually attempting to map the large scale structure of our observable universe. Each step outward depended on the notion of distance, which continues to underlie how we situate ourselves in the cosmos. To do this, the Hubble constant H_0 is among the most important parameters of our current cosmological model, as it sets the absolute scale for cosmic distances and ages.

For almost a century, measuring H_0 precisely and consistently has been a central challenge in cosmology. Today, two main approaches dominate: local determinations of the expansion rate via the local distance ladder, and an inverse route that combines observations of the cosmic microwave background with the cosmological standard model. With evolving measurement techniques, percent level accuracy in H_0 has been achieved, yet the two approaches do not agree. Two prominent determinations are the local measurements from the SH0ES collaboration, based on Cepheid calibrated Type Ia supernovae, which yield $H_0 = 73.04 \pm 1.04\,\mathrm{km\,s^{-1}\,Mpc^{-1}}$ [Riess et al., 2022],

and the inference from the cosmic microwave background observed by Planck within the ΛCDM model, which gives $H_0 = 67.36 \pm 0.54\,\mathrm{km\,s^{-1}\,Mpc^{-1}}$ [Planck Collaboration, 2018]. The origin of this Hubble tension, at the level of 5σ, remains an open puzzle.

But the Hubble tension is not simply about the value of a single number. At its core it reflects the challenge of reconciling an array of distance measurements at low redshifts with the global cosmological model. The local route depends on calibration of the absolute magnitude of Type Ia supernovae, but is largely independent of the cosmological model, while the inverse route does not require calibration, but is dependent on early-universe physics and the choice of a model. This can make it difficult to disentangle whether the discrepancy comes from the data or from the theoretical framework used to interpret them.

The motivation of this thesis is to take a step back and ask how far one can proceed without such assumptions of calibration, anchoring and a cosmological model. By combining uncalibrated Type Ia supernovae, unanchored baryon acoustic oscillations, and cosmic chronometer data under the distance duality relation, it develops the idea by Renzi and Silvestri [2023] for a calibration-free and model-independent route towards H_0. The aim is to establish a transparent reference built directly from data, against which the consistency of late universe probes can be tested. In doing so, the work contributes to the broader effort of clarifying what ingredients are needed to reach a self consistent picture of the universe's expansion.

This thesis is organized as follows. Chapter 2 introduces the general geometrical and kinematical framework of the expanding Universe, covering redshift, cosmological distances, and the distance duality relation, as well as the low-redshift cosmographic expansion. Chapter 3 provides a historical and methodological overview of the Hubble constant, reviewing its interpretations, measurement techniques, and the current Hubble tension with some possible solutions. Chapter 4 covers the methodological approach of determining H_0 from first principles in a model-independent way, without relying on local calibration of an absolute magnitude or anchoring with the sound-horizon. The observational datasets used in the analysis are described in Chapter 5. Chapter 6 discusses Gaussian process regression and its implementation for the non-parametric reconstruction of cosmological observables. The main findings of this work are presented and compared to related approaches in Chapter 7, which also discusses them in the broader context of the Hubble tension. Finally, Chapter 8 summarizes the conclusions.

2 Geometry & Cosmography of the Expanding Universe

This chapter introduces the purely kinematic framework, built on large-scale homogeneity, isotropy, and standard photon propagation,that underlies the model independent determination of H_0. Dynamic assumptions (e.g. the Friedmann equation or a specific energy budget) are not invoked.

2.1 FLRW Space-Time and Kinematics

The most general (and hence, up to trivial re-labellings, the unique) line element compatible with spatial homogeneity and isotropy - i.e. the assumption of the cosmological principle - is the Friedmann-Lemaître-Robertson-Walker (FLRW) metric. On large scales the universe is therefore maximally symmetric in its spatial sections (slices of constant cosmological time): every point and every direction are statistically equivalent. In *reduced circumference coordinates* the FLRW metric reads

$$ds^2 = -c^2\,dt^2 + a^2(t)\left[\frac{dr^2}{1 - k\,r^2/R_0^2} + r^2 d\Omega^2\right], \tag{2.1}$$

with $d\Omega^2 = d\theta^2 + \sin^2\theta\,d\phi^2$. Imposing spatial homogeneity and isotropy strips the ten free components of the symmetric four metric $g_{\mu\nu}$ down to only two quantities, the time-varying scale factor $a(t)$ and a length scale R_0 that fixes the constant spatial curvature [Baumann, 2022, p. 25]. The following conventions are adapted throughout:

- $k \in \{+1, 0, -1\}$: dimensionless curvature index (closed, flat, open);
- $a(t)$: dimensionless scale factor, normalised to $a(t_0) \equiv 1$;
- r: *comoving* radial coordinate (units of length);
- R_0: physical spatial curvature radius (units of length) set by the curvature density today $\Omega_{k,0} \equiv 1 - \Omega_0$.

Where the rescaling freedom of Eq. (2.1), i.e. $a \to \lambda a,\ r \to r/\lambda,\ R_0 \to R_0/\lambda$, is used to set the present-day scale factor to unity [Baumann, 2022, p. 25].

In this convention the discrete index $k \in \{+1, 0, -1\}$ retains its usual values while R_0 becomes the physical curvature radius today. Alternatively, some authors fix $R_0 = 1$ and leave $a(t_0)$ arbitrary; both choices are equivalent but one cannot impose both conditions at once.[1]

From the radial comoving coordinate r one can define the *proper (physical) separation*

$$\begin{aligned} D_{\mathrm{p}}(t) &= a(t)\, r, \\ \dot{D}_{\mathrm{p}}(t) &= \dot{a}\, r + a\, \dot{r} = H(t)\, D_{\mathrm{p}} + v_{\mathrm{pec}}, \\ H(t) &\equiv \frac{\dot{a}}{a}, \end{aligned} \tag{2.2}$$

where, henceforth, an overdot denotes d/dt. Here $H(t)$ is the *Hubble parameter*, and $v_{\mathrm{pec}} \equiv a\, \dot{r}$ is the peculiar velocity relative to the uniform Hubble expansion.

Instead of *reduced circumference coordinates* one can also write the metric of Eq. (2.1) in *hyperspherical coordinates*:

$$\begin{aligned} ds^2 &= -c^2 dt^2 + a^2(t) \Big[d\chi^2 + S_k^2(\chi)\, d\Omega^2 \Big], \\ \text{where} \quad S_k(\chi) &= \begin{cases} R_0 \sin(\chi / R_0), & k = +1, \\ \chi, & k = 0, \\ R_0 \sinh(\chi / R_0), & k = -1. \end{cases} \end{aligned} \tag{2.3}$$

The radial coordinate χ has units of length and is introduced by setting $dr \equiv d\chi \sqrt{1 - kr^2 / R_0^2}$ in Eq. (2.1) [Baumann, 2022, p. 25].

2.2 Redshift

With the partial exception of recent neutrino and gravitational-wave detections, almost all empirical information about the cosmos reaches us in the form of electromagnetic radiation. When a photon is emitted at cosmic time t_{e} and observed at t_0, the expansion of space stretches its wavelength and

[1] If one instead adopts the normalisation $R_0 = 1$, the numerical value of the curvature is transferred into the sign parameter itself; one then writes $k > 0$, $k = 0$ or $k < 0$ for closed, flat and open spatial slices, with $|k| = \sqrt{|\Omega_K|}\, c / H_0$.

lowers its frequency. The redshift describes a fractional change in photon energy,

$$z = \frac{\lambda_0 - \lambda_e}{\lambda_e} = \frac{\nu_e - \nu_0}{\nu_0} = \frac{a_0}{a_e} - 1, \tag{2.4}$$

and thus provides a direct link between observation and the scale-factor history.

For non-relativistic motions ($v \ll c$) one has the familiar linear approximation $z \simeq v/c$, but the exact special-relativistic Doppler relation reads

$$1 + z = \sqrt{\frac{1 + v/c}{1 - v/c}}, \tag{2.5}$$

valid in the local rest frame of the source. The observed redshift z_0 is usually decomposed into a cosmological part, $z_{\rm cos}$, produced by the Hubble flow, and a peculiar component, $z_{\rm pec}$. For $v_{\rm pec} \ll c$ the two are related by

$$v_{\rm pec} \simeq c\,\frac{z_0 - z_{\rm cos}}{1 + z_{\rm cos}}, \tag{2.6}$$

as shown by Hogg [2000, eqs. 9-10].

2.3 Cosmological Distance Measures

In everyday geometry one quotes a single, unambiguous number for the distance between two points. In our expanding Universe the situation is more complicated. The radial coordinates r and χ that appear in the FLRW metrics Eq. (2.1) and Eq. (2.3) are merely labels on the comoving grid, which are fixed by conventions and by themselves have no direct observational meaning. Only when χ is tied to an observed redshift - giving the *line-of-sight comoving distance* $\chi(z)$ - does it acquire physical content (see sec. 2.3.1). Even the *proper distance* introduced in Eq. (2.2) is not a directly measurable quantity, because it refers to the length of a ruler laid out instantaneously along a spatial hypersurface of constant cosmic time [Baumann, 2022, p. 35].[2]

What can be measured are separations encoded in the light that reach us today. All practical distance indicators - whether geometric, standard candles

[2] Any attempt to measure that length would be troubled by the fact that light from one end of the ruler must travel to the other, and during that time interval the scale factor would change.

(objects of known luminosity), or standard rulers (objects of known physical size) - rely on the properties of photons that travel on radial null paths and terminate at the observer [Hogg, 2000]. In this sense all cosmological distance measures are different ways of quantifying the spacing between two events (t_{em}, t_{obs}) that lie on a single light ray.

For sufficiently small redshift $z \ll 1$, equivalently $v/c \ll 1$ or $D \ll c/H_0$, the expansion may be approximated by the famous linear Hubble law,

$$D \simeq cz/H_0 \quad \Big(\text{or } v \simeq H_0 D\Big), \tag{2.7}$$

and every distance measure - i.e. luminosity, angular-diameter, comoving, etc. - agree on the same value within a few percent. [Hogg, 2000] This approximation must be applied with care, because it remains valid only at very low redshift; once higher order terms become non-negligible $z \gtrsim 0.05$ the different distance definitions begin to diverge.

2.3.1 Radial Null Geodesic and the Line-of-Sight Comoving Distance

For light rays $ds^2 = 0$ propagating radially $d\Omega^2 = 0$ the FLRW metric Eq. (2.3) gives

$$d\chi = \frac{c\,dt}{a(t)} = \frac{c\,dz}{H(z)}.$$

Integrating from reception $z = 0$ to emission z yields the *line-of-sight comoving distance*

$$\begin{aligned} \chi(z) &= \int_0^z \frac{c\,dz'}{H(z')} = D_{H_0} \int_0^z \frac{dz'}{E(z')}, \\ \text{where} \quad D_{H_0} &\equiv \frac{c}{H_0} \quad \text{and} \quad E(z) \equiv \frac{H(z)}{H_0}. \end{aligned} \tag{2.8}$$

The Hubble distance $D_{H_0} = c/H_0 \simeq 3000\,h^{-1}\,\mathrm{Mpc} = 9.26 \times 10^{25}\,h^{-1}\,\mathrm{m}$, where $h \equiv H_0/(100\,\mathrm{km\,s^{-1}Mpc^{-1}})$ [Hogg, 2000, Eq. 4], sets the absolute distance scale. Whereas $E(z)$ is the dimensionless Hubble parameter that describes the redshift dependence of the cosmic expansion. The distances D_{H_0} and $\chi(z)$ serves as cosmography's baseline, since they appear as building block in all the other distance definitions. The line-of-sight distance $\chi(z)$ is the current-epoch spacing, along our line of sight, between us and the source if both simply move with the Hubble flow [Hogg, 2000].

2.3.2 Transverse (or Proper Motion) Comoving Distance

Suppose two galaxies have the same redshift z but appear on the sky with an angular separation $\delta\theta \ll 1$. Their comoving separation orthogonal to the line of sight is defined as $D_M(z)\,\delta\theta$ [Hogg, 2000]. In the hyperspherical coordinates of Eq. (2.3) this is obtained by replacing the radial coordinate in the curvature function $S_k(\chi)$ with the line-of-sight comoving distance $\chi(z)$ from Eq. (2.8):

$$
\begin{aligned}
D_M(z) \;&\equiv\; S_k\Big[\chi(z)\Big],\\
\text{where}\quad S_k\Big[\chi(z)\Big] &= \begin{cases} \dfrac{D_{H_0}}{\sqrt{\Omega_{k,0}}}\sinh\Big(\sqrt{\Omega_{k,0}}\;\chi(z)/D_{H_0}\Big), & \Omega_{k,0} > 0,\\ \chi(z), & \Omega_{k,0} = 0,\\ \dfrac{D_{H_0}}{\sqrt{|\Omega_{k,0}|}}\sin\Big(\sqrt{|\Omega_{k,0}|}\;\chi(z)/D_{H_0}\Big), & \Omega_{k,0} < 0. \end{cases}
\end{aligned}
\tag{2.9}
$$

Here $S_k(\chi)$ is rewritten by substituting $R_0 = D_{H_0}/\sqrt{|\Omega_{k,0}|}$; this eliminates the explicit curvature radius in favor of the observationally convenient parameter $\Omega_{k,0} \equiv 1 - \Omega_{\text{tot},0}$.[3][4] Since the hyperbolic sinus is a complete function a compact way of writing Eq. (2.9) is

$$
D_M(z) = \frac{D_{H_0}}{\sqrt{\Omega_K}}\sinh\Big(\sqrt{\Omega_{k,0}}\;\chi(z)/D_{H_0}\Big), \tag{2.10}
$$

which holds for all real values of $\Omega_{k,0}$.[5]

The *transverse comoving distance* D_M has the same value like the *proper-motion distance*, which compares an object's physical transverse speed with its observed angular drift [Weinberg, Steven, 1971, pp. 423-424].

[3]The choice of the trigonometric versus hyperbolic function in S_k depends on the sign of the spatial curvature: a closed universe ($\Omega_K < 0$) bends separations on a 3-sphere and brings in the sine term, an open universe ($\Omega_K > 0$) bends them on a 3-hyperboloid and requires the hyperbolic sine, while the flat case ($\Omega_K = 0$) collapses to the identity. Note, however, that "spatial curvature" itself is not coordinate-invariant, one can always choose spatial coordinates that locally flatten a given time slice, the invariant quantity is the four dimensional space-time curvature tensor fixed by the stress-energy content.

[4]For $x > 0$ we have $\sinh x > x > \sin x$, it follows that $D_M^{\text{open}} > D_M^{\text{flat}} > D_M^{\text{closed}}$ for the same comoving χ.

[5]Where the identity $\sin(x) = \sinh(ix)/i$ is used.

Equation (2.9) will be related to the definitions of the *angular diameter distance* and *luminosity distance* in the following subsections.

2.3.3 Angular Diameter Distance

In a static, Euclidean space a simple way to define distance is to compare the angular size θ (in radians) of an object with its intrinsic physical size R, objects whose size R is known a priori are referred to as *standard rulers*. For sufficiently small angles[6] the basic Euclidean relation

$$\theta \;=\; \frac{R}{D} \tag{2.11}$$

identifies the distance D to the object.[7] To preserve the familiar Euclidean relation, one defines the *angular diameter distance*

$$D_A \;\equiv\; \frac{R}{\theta}\,, \tag{2.12}$$

so that Eq. (2.11) holds by construction even in an expanding FLRW universe.

If one considers two light rays that leave the source simultaneously at emission time t_e, separated by an infinitesimal angle $\delta\theta \ll 1$ in the (θ, φ) plane and sharing the same comoving radial coordinate χ (see Fig. 2.1). At emission their physical transverse separation is obtained from Eq. (2.3) with $\mathrm{d}\chi = \mathrm{d}\varphi = 0$:

$$\delta\ell_\perp(t_\mathrm{e}) = a(t_\mathrm{e})\, S_k(\chi)\, \delta\theta\,. \tag{2.13}$$

Identifying $\delta\ell_\perp(t_\mathrm{e}) \equiv R$ and $\delta\theta \equiv \theta$ in the small-angle limit gives the angular diameter distance

$$D_A(z) = \frac{R}{\theta} = a(t_\mathrm{e})\, S_k(\chi). \tag{2.14}$$

Utilizing the earlier result from Eq. (2.9) one finds

$$D_A(z) \;=\; a(t_\mathrm{e})\, S_k(\chi) \;=\; \frac{D_M(z)}{1+z}. \tag{2.15}$$

[6] Assuming $\theta \ll 1\,\mathrm{rad}$ so that $\sin\theta \simeq \theta$.

[7] Here, the generic label D is used for distance without a subscript, as the definitions of distances in static Euclidean space is unambiguous.

Due to the $1/(1+z)$ term, the growth of D_M is eventually suppressed so that D_A increases with redshift only up to approximately $z_{\max} \sim 1.5$ (ΛCDM) and then decreases, so standard rulers of identical size subtend larger angles on the sky at very high z. At the redshift $z_{\max}$ the cross-sectional area of the past light-cone is the biggest (refocussing of the past light-cone), i.e. our Universe is acting as a giant lens. This reflects cosmic expansion: the Universe, and hence the proper separation between us and the source, was smaller at the time of emission than it is today [Baumann, 2022, p. 40].

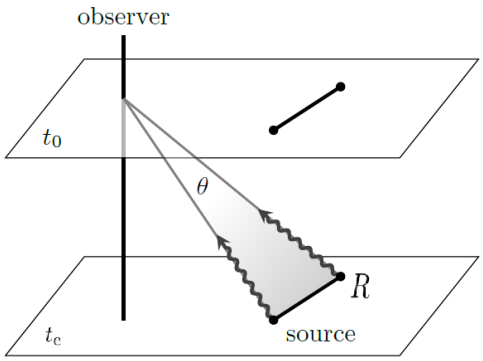

Figure 2.1: *Illustration of the geometry of angular diameter distance. A source of physical size R at emission time t_e subtends an angle θ at the observer at time t_0. Figure taken from Baumann [2022, Fig. 2.7, p. 40].*

2.3.4 Luminosity Distance

In observational cosmology, one of the most powerful methods for estimating the distance to astronomical objects is the use of *standard candles* - sources whose intrinsic (bolometric) luminosity L is known or can be reliably inferred. By measuring the received energy flux F the distance can be inferred. In non-expanding Euclidean space the inverse square law

$$F = \frac{L}{4\pi D^2} \tag{2.16}$$

identifies the physical distance D to the object. *Luminosity distance* D_L gets defined so that Eq. (2.16) still holds by definition, i.e.

$$D_L \equiv \sqrt{\frac{L}{4\pi F}}. \tag{2.17}$$

It is important to note that in an expanding space, this generally will not be equal to the proper distance.

If we assume that the source in Fig. 2.2 releases photons at time t_e with frequency ν_e, then in a short time interval δt_e, the number of released photons will be $N = L\,\delta t_\mathrm{e}/h\,\nu_\mathrm{e}$. Utilizing the cosmological principle, one conveniently chooses the source to be at radial coordinate $\chi = 0$, and the observer at χ. [Schutz, 2009, pp. 349-350] The photons will spread across a spherical surface and at time t_0 the proper area over they will have spread will be equal to the integral over the solid angle part of the line element in Eq. (2.3), i.e.

$$S = 4\pi\, a^2(t_0)\, S_k^2(\chi) = 4\pi\, D_M^2, \tag{2.18}$$

where the normalization of the scale factor, isotropy and Eq. (2.9) was used. Additionally, the energy of the arriving photons is decreased by a factor of $1/(1+z)$, since the photon's emission frequency ν_e is redshifted to a lower observed frequency $\nu_0 = \nu_\mathrm{e}/(1+z)$ (or equivalently to a higher wavelength). At last, also the arrival rate of photons is smaller by another factor of $1/(1+z)$ compared to when they were emitted. [Schutz, 2009, pp. 349-350] So the observed flux at time t_0 is

$$F = L/(S\,(1+z)^2) = L/(4\pi\, D_M^2\,(1+z)^2). \tag{2.19}$$

Alternatively, one may express this result locally in terms of infinitesimal beam properties: from the conservation of photon phase space density and assuming isotropic emission, it follows that

$$F\,dS = \frac{L}{4\pi}\frac{d\Omega}{(1+z)^2}, \tag{2.20}$$

where dS is the cross-sectional area of the beam at the observer and $d\Omega$ is the solid angle it subtends at the source. For an isotropic source emitting equally into all directions, $dS/d\Omega = S/(4\pi)$, recovering the same expression for the flux above. [Ellis et al., 2012, p. 163]

Comparing the result of Eq. (2.19) with the definition of luminosity distance in Eq. (2.17), one obtains

$$D_L = (1+z)\,D_M. \tag{2.21}$$

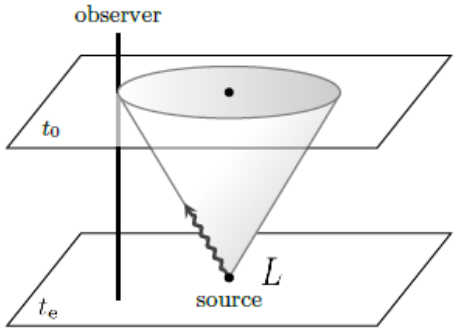

Figure 2.2: *Illustration of how light emitted by a source at time t_e with luminosity L travels through expanding space to reach the observer at time t_0. As the wavefront expands spherically, only a small portion intersects the detector, and the signal arrives stretched in both wavelength and arrival time due to cosmic expansion by a factor of $(1+z)^2$. Figure taken from Baumann [2022, Fig. 2.5, p. 36].*

Besides electromagnetic standard candles, recently detected gravitational wave signals from compact binary mergers now provide *standard sirens*, offering an exciting new route to measuring luminosity distance. In general relativity the strain amplitude of a GW signal decreases proportionally to $1/D_L$, so matching the observed chirp to a template gives the luminosity distance directly, without any intermediate flux calibration. A gravitational wave detection on its own, however, supplies no redshift; an electromagnetic counterpart or a statistical host-galaxy association is therefore essential to locate the siren on the $D_L(z)$ relation. [Baumann, 2022, p. 36]

Cosmological distances respond directly to the expansion history encoded in $E(z)$. In particular, when a cosmological constant is present the early Universe expansion rate is lower than in a purely matter-dominated model. The slower growth of the scale factor lets photons travel for a longer interval, so D_M,D_A and D_L all come out larger. Consequently, equally distant sources appear dimmer in a Λ-dominated Universe than they would if only matter were present. [Dodelson and Schmidt, 2020, p. 37]

2.4 Apparent Magnitude and Distance Modulus

Type Ia supernovae (SNe Ia) act as *standardizable candles*, whose absolute band magnitude M can be inferred with tight scatter. The observed flux from any source of luminosity L at luminosity distance D_L follows Eq. (2.16). In the B band, the *apparent magnitude* is defined as

$$m_B \;=\; -2.5\,\log_{10} F_B + \text{const.}\,. \tag{2.22}$$

The *distance modulus* is the difference between the apparent magnitude measured at redshift z and the absolute magnitude the object would have at a fiducial distance of 10 pc:

$$\begin{aligned}\mu_B \;\equiv\; m_B - M_B &= -2.5\log_{10}\left[\frac{F_B(D_L}{F_B(D_L{=}10\,\text{pc})}\right] \\ &= 5\log_{10}\left[\frac{D_L(z)}{10\,\text{pc}}\right] = 5\log_{10}\left[\frac{D_L(z)}{1\,\text{Mpc}}\right] + 25. \end{aligned}\tag{2.23}$$

So μ_B is just a logarithmic distance measure.

Therefore, one can write the measured apparent magnitude as follows,

$$m_B(z) = M_B + 5\log_{10}\left[\frac{D_L(z)}{\text{Mpc}}\right] + 25 \tag{2.24}$$

$$= \left[M_B - 5\log_{10} H_0\right] \;+\; 5\log_{10}\left[\frac{H_0 D_L(z)}{\text{Mpc}}\right] + 25, \tag{2.25}$$

so only the combination $\mathcal{M} \;\equiv\; M_B \;-\; 5\log_{10} H_0$ enters. Consequently, supernova data alone cannot separate the absolute magnitude from the Hubble constant; the product $\mathcal{D}_L \equiv H_0 D_L(z)$ is often called the Hubble-free luminosity distance, since $D_L \propto H_0^{-1}$.

For any filter X one generally writes

$$\mathrm{m}_X - M_X \;=\; \underbrace{\mu(z)}_{\text{band independent}} \;+\; \underbrace{K_X(z) + A_X}_{\text{band corrections}}, \tag{2.26}$$

where $K_X(z)$ is the k-correction accounting for the fact that an observer centered filter at frequency ν_X samples rest-frame $(1+z)\nu_X$:

$$K_X(z) \;=\; -2.5\log_{10}\left[(1+z)\,\frac{L_{(1+z)\nu_X}}{L_{\nu_X}}\right]$$

[Hogg, 2000, Eq. 27]; and $A_X = R_X\, E(B-V)$ is the dust extinction term, with $R_V \simeq 3.1$ for the Milky Way.

The supernova catalogues analysed here provide rest-frame, k-corrected and extinction corrected B-band magnitudes. So that throughout this work $\mu_B = m_B - M_B$ is used, with all band corrections already absorbed in the reported m_B.

2.4.1 Snapshot of the Modern Distance Ladder

This subsection provides a brief overview of some principal techniques currently used to determine cosmological distances. Most techniques rely on one (or a combination) of four underlying principles - geometry, standard candles, standard rulers, and (for gravitational waves) standard sirens. Typically one builds up a distance ladder, where each rung is calibrated by the one below it, but there are also some one-step methods who skip having to climb the ladder.

Primary (geometric) rungs:

- *Solar System radar*: Echo times to planets define the astronomical unit that underlies parallax.
- *Trigonometric* and *secular parallax*: Annual (or long-baseline) stellar parallaxes give distances to $\lesssim 10$ kpc.
- *Statistical parallax*: Using uniform stellar populations and comparing proper motions and radial velocity dispersions gives a mean distance measurement.
- *Moving-cluster geometry*: Proper motion convergence and radial velocities fix cluster distances.
- *Maser orbits*: Water masers moving in Keplerian disks enable geometric distance measurements by combining VLBI proper motions, Doppler shifts, and orbital geometry.
- *Main-sequence fitting*: To determine a cluster's distance by aligning its color-magnitude diagram with a calibrated reference, using the shift in brightness as a distance indicator.
- *Eclipsing binaries*: Light curves and radial velocities give stars' radii and temperatures, enabling an inference of luminosity and therefore distance.
- *Baade-Wesselink method*: Combining a pulsating star's radius change from spectroscopy with its brightness variations gives its

distance.

- *Sunyaev-Zelâdovich + X-ray*: Combining SZ and X-ray data gives a cluster's physical depth (along LOS); assuming symmetry, this and its angular size yield the angular diameter distance.

Secondary (calibrated) rungs:

- *Cepheid* and *RR-Lyrae variables*: Their period-luminosity relation gives distances to $\sim$40 Mpc.
- *Mira variables*: Long-period AGB stars allow distance measurements to $\sim$100 kpc.
- *Tip of the red giant branch (TRGB)* and *JAGB stars*: The sharp luminosity cut-off of RGB stars and the J-band asymptotic giant branch tip both serve as standardizeable candles in the $\sim 1-20$ Mpc range.
- *Large Magellanic Cloud anchor*: At $\sim$50 kpc the LMC provides a very important step in the ladder, with its distance measured by various calibrators.
- *Planetary-nebula luminosity function*: The bright end cutoff provides distances to $\sim$20 Mpc.
- *Globular-cluster luminosity function*: The peak absolute magnitude is nearly universal and distance independent.
- *Surface-brightness fluctuations*: Pixel-to-pixel variance scales with $1/D$ and works for smooth early-type galaxies.
- *Brightest-cluster galaxies*: Their relatively uniform luminosities make them useful as standard candles for distance estimates out to $\sim$300 Mpc.
- *Tully-Fisher, Faber-Jackson, D_n-σ*: Galaxy scaling relations link luminosity to rotation speed or velocity dispersion.
- *Type Ia supernovae*: Light curve shape standardises peak luminosity, giving D_L to $z \gtrsim 1$.
- *Type II supernovae*: The photospheric expansion (Baade-Wesselink) supplies distances independent of luminosity calibration.

One-step (ladder independent) distances:

- *Strong-lens time delays*: Differences in light travel time between multiple quasar images give the "time-delay distance" $D_{\Delta t}$, a single geometric scale that depends on the separations among observer, lens, and source.
- *Gravitational-wave standard sirens*: The strain amplitude and phase of a compact binary waveform fix the luminosity distance D_L without any photometric calibration.
- *Megamaser discs*: VLBI proper motions and Keplerian rotation curves of H_2O masers in discs yield geometric distances to individual galaxies at 3-30 Mpc.
- *Baryon Acoustic Oscillations (BAO)*: The comoving sound horizon r_s imprinted in large-scale structure acts as a standard ruler, providing $D_M(z)/r_s$ and $D_H(z)/r_s$ over $0.1 \lesssim z \lesssim 2.5$.

The list above is most likely not complete and has been configured using the lecture notes from Bartelmann [2022] and Bouwens [2024].

2.5 Etherington's Distance-Duality Relation

In the previous sections several cosmological distance measures were introduced, including the transverse comoving distance D_M, the luminosity distance D_L and the angular diameter distance D_A. Although they appear distinct, it can be shown that they are not independent: under very general assumptions, there exists a unique relation between them. This *distance duality relation* (DDR) is a purely geometric result discovered by Etherington [1933], valid in any spacetime, regardless of curvature, anisotropy, or inhomogeneity, provided that photons travel along null geodesics, their number is conserved and a metric theory of gravity holds. [Renzi and Silvestri, 2023]

To derive the relation, one can consider a bundle of light rays connecting a source and an observer. There are two natural ways to define an area distance, depending on the viewpoint:

- From the **observer's viewpoint**: a *past-directed* (incoming) bundle of null rays subtends a solid angle $d\Omega_0$ on the observer's sky at time t_0, and the bundle's cross-sectional area at the source is dS_0 (see Fig. 2.1.

This defines an area distance, that is the *angular diameter distance*[8], as

$$D_A^2 \equiv \frac{dS_0}{d\Omega_0}. \tag{2.27}$$

- From the **source's viewpoint**: a *future-directed* (outgoing) bundle of null rays subtends a solid angle $d\Omega_G$ at the emitter (source), and has a cross-sectional area dS_G at the observer at time t_0 (see Fig. 2.2). This defines a different notion of area distance

$$D_M^2 \equiv \frac{dS_G}{d\Omega_G}, \tag{2.28}$$

which one can associate with the *transverse comoving distance*[9] already defined earlier.

After defining both area distances, one finds that they are not independent but are in fact just different by a redshift factor. As first shown by Etherington [1933], the incoming and outgoing bundles of light rays described above share the same null geodesics, and their associated cross-sectional areas and solid angles obey the reciprocity condition

$$dS_G\, d\Omega_0 = (1+z)^2\, dS_0\, d\Omega_G, \tag{2.29}$$

where z is the redshift of the source as measured by the observer. Combining this result with the definitions of area distances in Eq. (2.27) and Eq. (2.28) from above, one obtains

$$D_M = (1+z)\, D_A. \tag{2.30}$$

Substituting the relation in Eq. (2.21) for D_M yields the familiar form of the DDR:

$$D_L = (1+z)\, D_M = (1+z)^2\, D_A. \tag{2.31}$$

This redshift dependence arises because the solid angle under which a source is observed transforms under the relative motion of source and observer, following the special-relativistic transformation of angles. As a result, the

[8] This area distance goes by many different sometimes confusing names including *area distance*, *observer area distance*, *distance by apparent size* or *corrected luminosity distance*.

[9] This area distance is also called *galaxy area distance, effective distance, angular size distance* or *proper motion distance*.

apparent asymmetry between D_A and D_M is fully accounted for by the redshift factor. In cases like gravitational lensing, where light rays are bent and can refocus, a source may appear both unusually large and unusually bright, so that apart from redshift effects, an object far away can produce the same observed flux in a given solid angle as one that is much nearer. [Ellis et al., 2012, p. 166] There is only **one independent cosmological distance measure**.

Testing the DDR is a powerful consistency check between independent datasets that probe different cosmological distance measures. Since the DDR relies only on minimal and well-motivated assumptions, any observed violation is more likely to signal systematics or inconsistencies in the data. Nevertheless, a confirmed breakdown of Eq. (2.31) would have profound implications, potentially pointing to new physics such as photon absorption or scattering, or exotic effects like photon-axion conversion or deviations from a metric theory of gravity.

To quantify potential deviations from the distance duality relation, the dimensionless parameter

$$\eta(z) \equiv \frac{D_L(z)}{(1+z)^2 D_A(z)} = 1 \tag{2.32}$$

is introduced, which equals unity if the DDR holds exactly. Any redshift-dependent departure $\eta(z) \neq 1$ would signal either unaccounted observational systematics or a breakdown of the underlying physical assumptions.

2.6 Low-Redshift Cosmography

For sources at small redshifts ($z \lesssim 1$), one can use the analytical properties of the scale factor $a(t)$ near the present time t_0 to expand cosmological observables in powers of z. This model-independent approach relies solely on the assumption of a homogeneous and isotropic FLRW geometry, without invoking the Friedmann equations or a specific energy content. [Visser, 2004]

Following Visser [2004], one defines the first three time derivatives of the

scale factor as

$$H(t) \equiv \frac{1}{a}\,\dot{a}, \tag{2.33}$$

$$q(t) \equiv -\frac{1}{a}\,\ddot{a}\left(\frac{\dot{a}}{a}\right)^{-2} = -\frac{\ddot{a}}{aH^2}, \tag{2.34}$$

$$j(t) \equiv \frac{1}{a}\,\dddot{a}\left(\frac{\dot{a}}{a}\right)^{-3} = \frac{\dddot{a}}{aH^3}. \tag{2.35}$$

These parameters are all dimensionless and describe the kinematics of expansion: H is the Hubble rate, q the deceleration parameter, and j is called the jerk parameter. Around t_0, the scale factor can be expanded as

$$\begin{aligned} a(t)\Big|_{t_0} &= 1 + H_0\,(t-t_0) - \frac{1}{2}q_0\,H_0^2\,(t-t_0)^2 + \\ &\quad + \frac{1}{6}j_0\,H_0^3\,(t-t_0)^3 + \mathcal{O}\Big((t-t_0)^4\Big), \end{aligned} \tag{2.36}$$

where a_0 is set to unity and all parameters with subscript zero (i.e. H_0, q_0, j_0) refer to their present day values.

Using the definition of redshift in Eq. (2.4) one can invert the expansion in Eq. (2.36) to obtain redshift as a function of lookback time $\Delta t = t_0 - t$:

$$\begin{aligned} z &= H_0\,\Delta t + \frac{1}{2}(1+q_0)\,H_0^2\,\Delta t^2 \\ &\quad + \frac{1}{6}\left(j_0 + 3q_0 + 3q_0^2\right)\,H_0^3\,\Delta t^3 + \mathcal{O}(\Delta t^4), \end{aligned} \tag{2.37}$$

This can be inverted to express lookback time in terms of z:

$$\begin{aligned} H_0\,\Delta t &= z - \frac{1}{2}(1+q_0)\,z^2 + \\ &\quad + \frac{1}{6}\left(1 + q_0 + 3q_0^2 - j_0\right)\,z^3 + \mathcal{O}(z^4). \end{aligned} \tag{2.38}$$

The line-of-sight comoving distance χ is given by

$$\chi(z) = c\int_t^{t_0}\frac{dt'}{a(t')} = c\Delta t + \frac{1}{2}H_0 c\Delta t^2 + \mathcal{O}(\Delta t^3), \tag{2.39}$$

which becomes, upon substituting $\Delta t(z)$,

$$\begin{aligned} \chi(z) &= \frac{c}{H_0}\Big[z - \frac{1}{2}(1+q_0)z^2 + \\ &\quad + \frac{1}{6}(1+q_0+3q_0^2-j_0)z^3 + \mathcal{O}(z^4)\Big]. \end{aligned} \tag{2.40}$$

Equations (2.36)-(2.40) follow the approach of Baumann [2022, Eqs. (2.71)-(2.75)].

For a flat universe ($k = 0$), the luminosity distance is related to χ by $D_L(z) = (1+z)\,\chi(z)$. Plugging in the expansion yields

$$D_L(z) = \frac{c\,z}{H_0}\Bigg[1 + \frac{1}{2}(1-q_0)\,z - \\ - \frac{1}{6}\left(1 - q_0 - 3q_0^2 + j_0\right)\,z^2 + \mathcal{O}(z^3)\Bigg]. \tag{2.41}$$

In the case $k \neq 0$ curvature enters at third order in z:

$$D_L(z) = \frac{c\,z}{H_0}\Bigg[1 + \frac{1}{2}(1-q_0)\,z - \\ - \frac{1}{6}\left(1 - q_0 - 3q_0^2 + j_0 - \Omega_{k,0}\right)\,z^2 + \mathcal{O}(z^3)\Bigg], \tag{2.42}$$

where $\Omega_{k,0} \equiv -\frac{k\,c^2}{H_0^2\,a_0^2}$ [Visser, 2004, Eq. (46)].

The expansions of angular diameter distance $D_A(z)$ and transverse comoving distance $D_M(z)$ can be easily obtained using Eq. (2.31).

3 Chasing H_0

In our physical theories, fundamental constants serve as essential bridges between theoretical models and the empirical reality we observe. Among these, the Hubble constant holds a central role in cosmology, setting the scale for the age of the Universe, providing the basis for distance measurements, and anchoring our understanding of cosmic evolution. Accurately measuring H_0 has been a challenge for over nearly a century, and today, the tension between different measurements suggests that our current cosmological standard model may be missing important pieces or there are unaccounted systematics in some of the measurements.

3.1 Origins and Interpretations of H_0

The concept of the Hubble constant emerged during a revolutionary period in early 20th–century astronomy. In 1912, Henrietta Swan Leavitt's discovery of the period–luminosity relation for Cepheid variable stars [Leavitt and Pickering, 1912] set an important basis for extragalactic distance measures. Shortly after, Vesto Slipher systematically measured redshifts of spiral nebulae, showing that most galaxies recede from Earth [Slipher, 1917]. Building upon Einstein's general relativity, Georges Lemaître independently theorized in 1927 that galaxies' recession reflects the expansion of space itself, deriving a linear velocity–distance relation (see Eq. (2.7)) [Lemaître, 1927]. In 1929, Edwin Hubble empirically confirmed this relation [Hubble, 1929], applying Leavitt's period–luminosity relation and Slipher's redshifts, establishing the observational basis for what became known as Hubble's law (see Fig. 3.1).[1] He measured H_0 to be approximately $570\,\mathrm{km\,s^{-1}\,Mpc^{-1}}$, a value nearly an order of magnitude higher than current estimates. [2]

[1] Notably, Hubble cited neither Leavitt nor Slipher in his 1929 paper.

[2] Due to miscalibrated Cepheid distances, having mistakenly included fainter W Virginis stars, which led to underestimated distances and an inflated H_0 [Bartelmann, 2022].

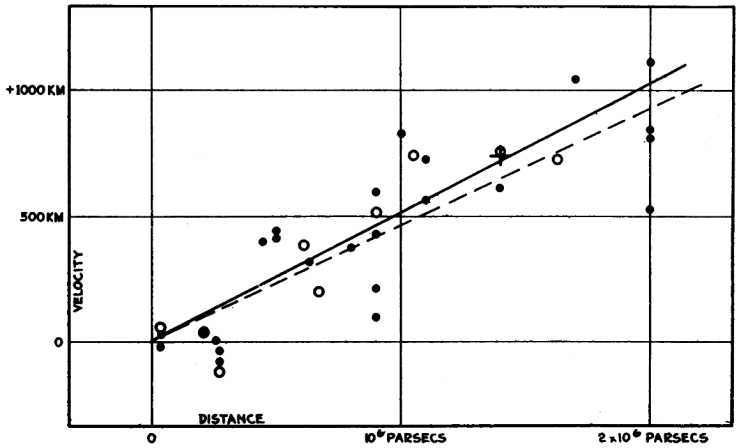

Figure 3.1: *Recession velocity versus distance for nearby galaxies, as presented in Fig. 1 of Hubble [1929]. The black dots and a solid line represent individual nebulae, open circles and a dashed line show the result from grouping them, and the cross indicates the average velocity of 22 nebulae whose individual distances were not determined [Hubble, 1929]. Hubble also omitted data points that did not support the linear trend he was aiming to demonstrate.*

The Hubble constant sets the characteristic time scale for cosmic expansion. In the simplest case of constant expansion, the age of the Universe is $t_0 \propto 1/H_0$. [3]

There are two principal ways to interpret the Hubble constant H_0:

- **Geometric interpretation:** From a geometric perspective, H_0 sets the absolute distance scale in the Universe. This follows from the generalized Hubble law:

  $$\chi(z) = c \int_0^z \frac{dz'}{H(z')},$$

  where $\chi(z)$ is the line-of-sight comoving distance introduced in Sec. 2.3.1. In the low redshift limit $z \ll 1$, this expression reduces to $\chi(z) \approx cz/H_0$ (see Eq. (2.7)). When properly calibrated this approach allows for a *model–independent* determination of cosmic distances, once $H(z)$ is known observationally. This approach is used for late time determinations of H_0, such as those from the local distance ladder.

[3] In a matter–dominated universe, gravity decelerates the expansion, leading to $t_0 < 1/H_0$. In contrast, a dark energy dominated universe experiences accelerated expansion, yielding $t_0 > 1/H_0$. The precise age of the Universe thus depends on the relative contributions of matter (Ω_m) and dark energy (Ω_Λ) in the Friedmann equations.

- **Dynamical interpretation:** Dynamically, H_0 describes the speed of cosmic expansion at low redshift, appearing in the Friedmann equation:

$$H(z)^2 = H_0^2 \left[\Omega_{m,0}(1+z)^3 + \Omega_{r,0}(1+z)^4 + \Omega_{\mathrm{X},0}\, X(z)\right], \tag{3.1}$$

  where $\Omega_{m,0}$, $\Omega_{r,0}$, and $\Omega_{\mathrm{X},0}$ are the present-day density parameters for matter, radiation, and any additional energy components beyond the standard matter and radiation content. The function $X(z)$ encodes the redshift dependence of such contributions, e.g. dark energy, curvature or modified gravity, with $X(z) = 1$ corresponding to a cosmological constant [Renzi and Silvestri, 2023].

There is usually a tradeoff between calibration and model dependence in determining H_0. Early time approaches, such as those based on the CMB sound horizon, are calibration free but usually rely on cosmological model assumptions. In contrast, late time methods, including the local distance ladder, are model independent but require careful calibration. The next section will explore the variety of paths towards H_0.

3.2 Measuring H_0

3.2.1 Direct Measurements using the Distance Ladder

The cosmic distance ladder is the direct or local route towards H_0, but to measure the Hubble constant one must observe distant enough objects, whose recession velocities are dominated by the cosmic expansion, i.e. galaxies in the Hubble flow ($z \gtrsim 0.01$), where peculiar velocities ($\sim 300-600\,\mathrm{km/s}$) contribute less than about ten per cent to their redshift [Bartelmann, 2022]. Since direct geometric measurements to such high redshift objects are not possible with current measurement technology, a ladder of distance indicators needs to be climbed. Each rung of the ladder extends further into the cosmos and relies on calibration from the rung below. The modern distance ladder usually consists out of three rungs (see Figure 3.2).

3.2.1.1 Overview of the 3 Rungs

First Rung: The first rung is the basis for the distance ladder and builds upon geometrical methods such as parallax, eclipsing binaries and observations of masers to set the zero point of the ladder [Riess et al., 2022]. The

objective of the first rung is the calibration of secondary distance indicators like Cepheid and Mira variables, TRGB, and JAGB stars. Precise measurements from GAIA give parallax distances to nearby galactic cepheids [Riess et al., 2021]. The Large Magellanic Cloud (LMC), at a distance of about 50 kpc, serves as a key anchor galaxy, where detached eclipsing binaries (DEBs) enable an independent geometric distance measurement with 1% precision [Pietrzyński et al., 2019]. Another important anchor is NGC 4258, located at 7.6 Mpc, where VLBI observations of water-maser orbits yield a similarly precise geometric distance [Humphreys et al., 2013]. Early-type DEB programmes in M31 and M33 promise two further geometric anchors within the coming years [Di Valentino et al., 2025]. The first rung extends until redshifts of $z \lesssim 0.002$ or distance of a few Mpc [Perivolaropoulos, 2024].

The secondary distance indicators can be seen in more distant galaxies, each of them comes with its own characteristics and systematics.

- **Cepheids** are young, bright and massive, pulsating stars.[4] They show a clear relation between pulsation period and luminosity, making them adequate standard candles. Cepheids are typically found in star forming regions of late type galaxies. Their main systematics include a dependence on metallicity, crowding in dense fields, and extinction effects because of dust.[Freedman and Madore, 2010, Gieren et al., 2018, Riess et al., 2016]. Additional challenges include the complexity of the calibration process, which involves multiple choices, such as period cuts, completeness thresholds, and artificial star corrections, and the fact that Cepheids are not simple standard candles, but require detailed modelling and multi step standardization. [Freedman et al., 2025]
- **Miras** are pulsating stars with a long period on the asymptotic giant branch (AGB) and are particularly bright in the near infrared. They can be found in older and intermediate-age stellar populations. Current challenges include distinguishing between carbon- and oxygen-rich types, limited calibration to short-period O-rich Miras, and larger scatter among long-period or C-rich Miras due to effects like hot-bottom burning[5]. [Huang et al., 2020, 2024]

[4] The pulsation is driven by the κ-mechanism: in regions where helium is partially ionized, compression increases the opacity, trapping radiation and raising local temperature and pressure. That leads to an expansion of the outer layers, which leads to cooling and a drop in opacity, allowing heat to escape, leading to contraction.

[5] Hot-bottom burning occurs in massive AGB stars when the base of the convective envelope reaches temperatures high enough for hydrogen fusion, increasing luminosity and changing the P-L relation.

- **Tip of the Red Giant Branch (TRGB)** stars show a sharp luminosity cutoff at the onset of helium burning in low mass red giant stars.[6] They can be found in the outer halos of both early and late type galaxies, often in regions with low extinction. The TRGB magnitude is the inflection point of a red giant branch luminosity function, usually measured with edge detection algorithms or a maximum likelihood fit. In the Cousins I band (HST/ACS F814W, JWST/NIRCam F090W) the corresponding absolute magnitude M_I is nearly independent of metallicity for old, metal-poor stars [Di Valentino et al., 2025]. After geometric calibration TRGB distances can set the absolute scale for SNe Ia or surface-brightness fluctuations (SBF)[7], allowing for two independent routes to H_0. Recent JWST observations extend the method to $\sim 50\,\mathrm{Mpc}$. Important systematics come from stellar population effects, photometric precision, and edge detection algorithms. [Beaton et al., 2016, Freedman et al., 2019, Madore et al., 2009]
- **J-band AGB (JAGB)** stars are rich in carbon, thermally pulsing AGB stars that show a narrow luminosity distribution in the near infrared J band. They are identified by their infrared colors, and can be found in intermediate age stellar populations across diverse types of galaxies. They are about a magnitude brighter than TRGB stars and require only single epoch photometry observations. The method measures the peak of the "J-region" luminosity function in an outer-disk field to minimise crowding and reddening [Di Valentino et al., 2025]. Systematic effects such as metallicity, star formation history, population selection appear to have a relatively small impact. Remaining challenges are, next to the novelty of the method, internal reddening, and the need for careful population selection. [Freedman and Madore, 2023, Freedman et al., 2025]

Second Rung: The purpose of the second rung is to use stellar distance indicators (cepheids, TRGB/JAGB, etc.), calibrated via geometric methods in the first rung, to in turn calibrate **Type Ia supernovae (SNe Ia)**, which can then act as bright standardizeable candles far into the Hubble flow. Sne Ia originate in binary systems where a carbon-oxygen white dwarf accretes mass from a companion. When the white dwarf gets close to the Chandrasekhar limit of approximately 1.4 $M_\odot$, the electron degeneracy pressure in the core

[6] This helium flash occurs at nearly the same luminosity for all such stars, making the cutoff a reliable standard candle.

[7] An important advantage over Cepheids, which are absent in the old stellar populations of early-type galaxies used for SBF measurements.

can no longer stabilize it, leading to a collapse that burns roughly half of the star's mass into iron group elements (mainly ^{56}Ni). Because the explosion always stars close to this critical mass, the peak luminosity lies in a narrow range. With some residual differences, e.g. brighter events trap radiation longer and therefore fade more slowly.[8] Correcting each SN Ia for light curve stretch and color residues reduces the intrinsic scatter from 0.5 mag to less than 0.1 mag, making them standardizeable candles, once an external zero point is set. The procedure usually involves three steps:

1. **Anchor selection:** Identify galaxies that host both SNe Ia and secondary distance indicators (Cepheids, TRGB, Miras, or JAGB). The calibrated indicators provide a distance modulus, $\mu_{\rm cal}$, accurate to a few percent at typical distances of approximately $10-40$ Mpc ($0.002 \lesssim z \lesssim 0.01$) [Perivolaropoulos, 2024].

2. **Light-curve standardization:** Fitting the SN Ia light curve (e.g., with SALT3 [Kenworthy et al., 2021]) to obtain the peak magnitude m_B, the stretch parameter x_1 and the color parameter c. The apparent magnitude is then "standardized" with the Tripp relation, [Tripp and Branch, 1998]

$$m_B^{\rm corr} = m_B + \alpha\, x_1 - \beta\, c\,, \tag{3.2}$$

   where the parameters α and β describe empirical correlations of luminosity with stretch and color, respectively, and are fitted simultaneously with the anchor sample. Additional corrections for selection effects and host galaxy biases are applied separately, typically as part of a distance bias correction term derived from simulations.[9] [Brout et al., 2022]

3. **Absolute magnitude calibration:** For each anchor galaxy the fiducial absolute magnitude is

$$M_B^0 \;=\; m_B^{\rm corr} - \mu_{\rm cal}, \tag{3.3}$$

   where $m_B^{\rm corr}$ is the stretch- and color-corrected peak magnitude from Eq. (3.2). By fitting all anchor SNe Ia together, one obtains best fit values for the standardisation parameters α, β, and the fiducial absolute magnitude M_B^0. Once these three parameters are fixed, any SN Ia with

[8] This width-luminosity connection is quantified by the Philips relation, $L \propto \tau^{1.7}$ [Phillips, 1993].

[9] In practice, the standardization model also applies a host mass correction, often written as a term $\gamma\,\Theta(M_\star - 10^{10}\,M_\odot)$, and a simulation based bias correction $\delta\mu_{\rm bias}$ that accounts for selection effects, light curve sampling, and survey calibration. Both terms are folded into the distance modulus estimate, see Kessler et al. [2019] for details.

a well measured light curve gives a distance modulus and thus extends the ladder deep into the Hubble flow.

An important assumption is that any dependence on dust, metallicity, or redshift has been absorbed by the empirical corrections applied to the SNe Ia magnitudes, so that the global standardization parameters α, β, and the fiducial absolute magnitude M_B^0 can be treated as universal across the full SN Ia sample.

Third Rung: With the fiducial absolute magnitude M_B^0 now calibrated by the second rung, one can determine the Hubble constant from SNe Ia magnitudes in the Hubble flow ($0.023 \lesssim z \lesssim 0.15$; following Riess et al. [2016]) by combining the observed, standardized magnitudes to the theoretical model derived from the cosmographic expansion of the luminosity distance in Eq. (2.42),

$$m_{B,\mathrm{th}}(z) = M_B^0 - 5\log_{10}(H_0) + 5\log_{10}\left[\mathcal{D}_L(z; q_0, j_0)\right] + 25, \quad (3.4)$$

where $\mathcal{D}_L$ is the cosmographic expansion of the Hubble free luminosity distance introduced in Sec. 2.4. Here, the degeneracy between H_0 and M_B is evident, requiring the external calibration of the absolute magnitude via the distance ladder. The best fit parameters are obtained by minimizing the quadratic form

$$\chi^2(H_0, q_0, j_0) = \left(\mathbf{m}_B^{\mathrm{corr}} - \mathbf{m}_{B,\mathrm{th}}\right)^{\mathrm{T}} \mathbf{C}^{-1} \left(\mathbf{m}_B^{\mathrm{corr}} - \mathbf{m}_{B,\mathrm{th}}\right), \quad (3.5)$$

where $\mathbf{m}_B^{\mathrm{corr}}$ is the vector of corrected magnitudes, $\mathbf{m}_{B,\mathrm{th}}$ the model vector evaluated at the redshifts z_i, and $\mathbf{C}$ is the full covariance matrix. Using the full covariance ensures that photometric calibration errors, model uncertainties, and sample selection correlations are propagated into the final uncertainty on H_0. [Riess et al., 2022]

Since each rung carries its own systematics, the overall uncertainty accumulates from multiple sources: (i) imperfect corrections or residual trends in the standardization of SNe Ia, (ii) uncertainties in the calibration of secondary distance indicators, (iii) influence of peculiar velocity corrections, especially at lower redshifts, (iv) dependence on the chosen redshift limit of the Hubble flow sample. The distance ladder requires calibration, but is in principle model independent, it just relies on the cosmological principle, without requiring a specific model for the expansion history.

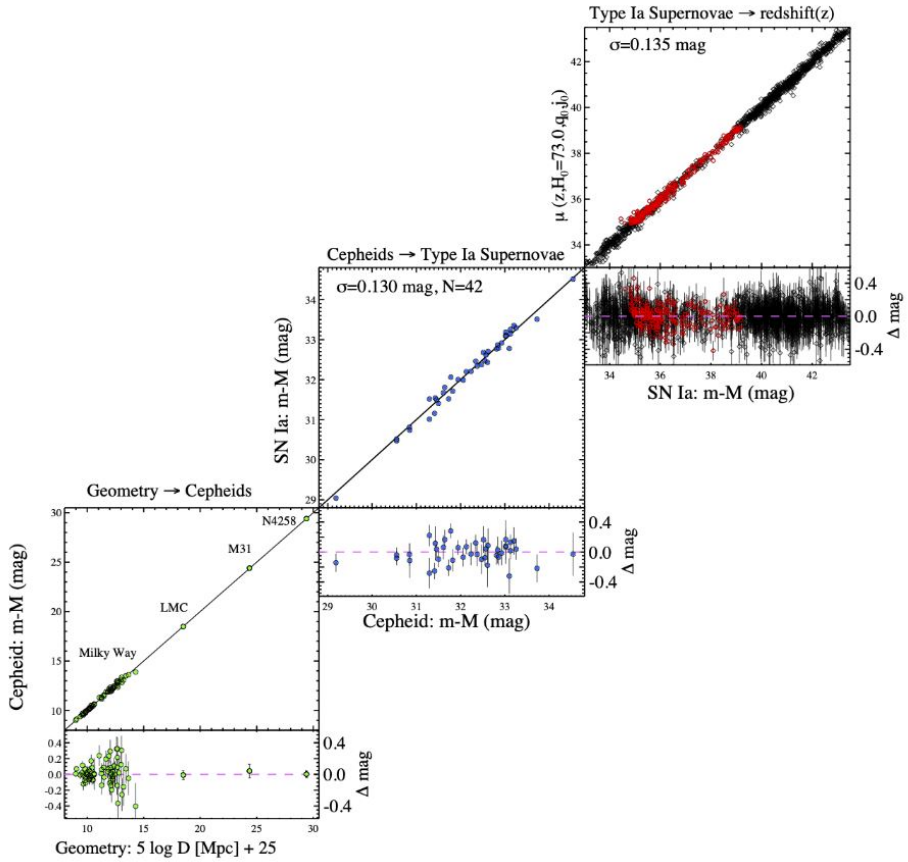

Figure 3.2: *Three-rung Cepheid based distance ladder from the SH0ES collaboration used to determine H_0. On the bottom left are the geometric distance anchors (Milky Way, LMC, M31, NGC 4258) to calibrate Cepheid absolute magnitudes. In the middle panel the calibrated Cepheid distances set the absolute magnitude of SNe Ia observed in the same host galaxies (42 hosts). In the top right the calibrated SNe Ia are used to trace the magnitude-redshift relation in the Hubble flow ($0.023 < z < 0.15$). Figure taken from Riess et al. [2022, Fig. 12].*

3.2.1.2 Complementary Distance Indicators

Within the local, direct route to determining H_0, several secondary techniques complement the SN Ia ladder, offering independent cross checks and refinements to supernova based distances.

Surface Brightness Fluctuations (SBF): SBFs use how grainy a galaxy appears as a measure of distance. The mean surface brightness is dominated by the brightest red giant stars. In more distant galaxies more individual

stars can crowd into each pixel of the detector. The surface brightness per pixel stays the same, but the Poisson granularity is smoothed out. Every time the distance doubles, approximately four times as many stars fall into each pixel. The fluctuation signal therefore scales as $1/D$.[10] One can measure the amplitude of the fluctuations in the image power spectrum and calibrate it with nearby Cepheid or TRGB anchor galaxies. This gives an absolute distance measurement. Combining this distance with measures of the recession velocity, give a point in the Hubble diagram. The method works best in dust free, early type galaxies. It is mainly limited by sky subtraction, precise modelling of the point-spread function, residual globular cluster and background variance, internal extinction, and a color dependent zero point connected to the metallicity of the red giant branch. [Cantiello and Blakeslee, 2023, Freedman and Madore, 2023]

Tully-Fisher (TF): The TF relation is an empirical correlation between the rotational velocity of spiral galaxies and their luminosity, giving a model independent way to estimate distances. The more recent Radial TF (RTF) relation generalizes this by showing that TF-like correlations hold at multiple radii within spiral galaxies. Using a large local galaxy sample, the RTF method allows for constraints on possible spatial variations in the local expansion rate. Recent work shows that within the distance range of 10-140 Mpc, deviations in the locally inferred Hubble parameter are limited to just a few percent, this puts strong bounds on the possibility of local structure significantly biasing expansion rate measurements. [Haridasu et al., 2024] The TF relation requireds calibration using intermediate distance indicators to set the zero point. Similar scaling relations also exist for early type galaxies, i.e. the **Fundamental Plane (FP)**, which links the size, surface brightness, and velocity dispersion. The FP typically shows larger scatter than the TF relation and is more sensititve to stellar population effects like age and metallicity variations. [Graves et al., 2009]

Planetary Nebula Luminosity Function: Evolved low mass stars go through the planetary nebula phase, producing a luminosity function whose bright end shows a sharp cut off. The brightest nebulae emit strong and narrow emission lines, that stand out in narrow band images. This makes it possible to detect them even in distant galaxies. Since the cut off lumi-

[10] Each star's flux scales as $F \propto 1/D^2$, and the number of stars in a pixel scale as $N \propto D^2$. Hence, the mean surface brightness is $\langle S \rangle = NF \propto$ const. Poisson statistics give a variance $\sigma^2 = NF^2 \propto D^{-2}$, so the rms fluctuation is $\sigma \propto 1/D$. The SBF signal is $\sigma/\langle S \rangle$, and therefore scales as $1/D$.

nosity can be calibrated, the apparent magnitude of the brightest planetary nebulae can be converted into a distance. [Bartelmann, 2022] Sources of uncertainty for the method are metallicity and age dependence of the cut off, internal dust extinction, and contamination with HII regions or photometric incompleteness.[Ciardullo, 2022]

L-σ Scaling for HII galaxies: Young, compact HII galaxies host intense starbursts in massive stellar clusters, which leads to strong emission lines. A tight empirical correlation exists between the luminosity of the Balmer lines and the gas velocity dispersion, called the L-σ relation. This scaling makes them promising standard candles, independent of redshift, for measuring cosmic distances. But, the relation also requires a zero point calibration from independently known distance measures. Then, the method can trace the Hubble flow even at high redshift, offering a complementary measurement to SNe Ia. [Chávez et al., 2014]

3.2.2 Inverse Distance Ladder: Sound Horizon Based H_0 Measurements

An alternative to the local, direct determination of H_0 is the inverse distance ladder, which infers the Hubble constant by anchoring cosmological distance measures using the sound horizon scale.

3.2.2.1 The Sound Horizon at Recombination

The sound horizon r_* refers to the maximum (comoving) distance acoustic waves could have propagated in the early universe baryon–photon plasma before recombination (last scattering) at redshift z_*. It acts as a *standard ruler*, whose imprint can be found in the CMB power spectrum and the late time clustering of galaxies. It is formally given by

$$r_* = \int_{z_*}^{\infty} \frac{c_s(z)}{H(z)}\, dz, \tag{3.6}$$

where c_s is the sound speed in the photon–baryon plasma.[11] Importantly, here the expansion history $H(z)$ enters at early times. In standard ΛCDM cosmology the speed of sound c_s is given by

$$c_s(z) = \frac{c}{\sqrt{3(1+\frac{3\Omega_{b,0}}{4\Omega_{r,0}(1+z)})}}, \tag{3.7}$$

[11] Because baryons are tightly coupled to photons by Thomson scattering until recombination, the effective sound speed in the primordial plasma remains below c.

where $\Omega_{b,0}$ and $\Omega_{r,0}$ refer to the present day baryon and radiation content respectively. Given the results of Planck Collaboration [2018] one obtains

$$r_* \approx (147.09 \pm 0.26)\,\mathrm{Mpc}. \tag{3.8}$$

3.2.2.2 H_0 from the CMB

The angular scale of the first acoustic peak in the CMB temperature power spectrum directly reflects the sound horizon at last scattering, since these modes have undergone exactly one compression cycle by z_*. The observed angular scale

$$\theta_* \;=\; \frac{r_*}{D_M(z_*)}\,, \tag{3.9}$$

relates the comoving sound horizon r_* to the transverse comoving distance

$$D_M(z_*) \;=\; \frac{c}{H_0}\int_0^{z_*}\frac{dz}{E(z)}\,, \tag{3.10}$$

here a flat geometry is assumed and the expansion history of late times enters the integral. One then can combine a precise measurement of θ_* with a model for $D_M(z_*)$, which depends on H_0, to infer H_0. But, if one rewrites the observable θ_* as

$$\theta_* = \frac{r_* H_0}{c}\left(\int_0^{z_*}\frac{dz}{E(z)}\right)^{-1}\,, \tag{3.11}$$

the degeneracy between r_* and H_0 becomes obvious. A bigger H_0 can be accounted for by a smaller r_* and vice versa. To break the degeneracy, either additional data has to be added, or one has to theoretically predict r_* from a model for early universe physics.

In practice the θ_* measurement is extremely robust, cross checks between Planck, Atacama Cosmology Telescope (ACT) and South Pole Telescope (SPT) show sub-percent agreement in the acoustic peak positions [Aiola, 2020, Planck Collaboration, 2018]. The remaining uncertainty on the CMB inferred H_0 is dominated by modelling assumptions rather than instrumental effects (foreground residuals, beam calibration and lensing systematics), which shift θ_* by $\lesssim 0.2\%$ [Planck Collaboration, 2018]. The largest changes arises from early Universe parameters that set the physical sound horizon r_* [Addison et al., 2018, Efstathiou and Gratton, 2021]. Consequently the quoted systematic error on CMB H_0 is below $1\,\mathrm{km\,s^{-1}\,Mpc^{-1}}$, to change the result the underlying cosmological model would need to be changed.

3.2.2.3 H_0 from BAO

Baryonic acoustic oscillations offer an independent confirmation of the sound horizon at late times, which can be observed as a peak in the two-point correlation function of galaxy clustering. BAO measurements constrain the combination of a distance and the sound horizon. Along the line-of-sight BAO data yield D_H/r_d and the transverse BAO scale gives D_M/r_d. [12] When the line-of-sight and transverse BAO scales cannot be resolved individually, a volume-averaged distance measurement is reported. In the BAO observables a similar degeneracy between the sound horizon and H_0 becomes apparent,

$$\frac{D_M(z)}{r_d} = \frac{c}{r_d\, H_0} \int_0^z \frac{dz}{E(z)} \,, \tag{3.12}$$

$$\frac{D_H(z)}{r_d} = \frac{c}{r_d\, H(z)} \,. \tag{3.13}$$

In both cases only the combination $r_d\, H_0$ appears, making it difficult to disentangle them without external constraints or model assumptions. Although these indirect soundhorizon-based approaches achieve a high precision in the inferred Hubble constant, they are sensitive to the cosmological model used.

Although sound horizon methods have sub-percent statistical precision, they remain model dependent. The value of the standard ruler r_d is computed assuming ΛCDM, so any change to early time physics (extra relativistic species, early dark energy episodes, non standard recombination) rescales r_d and shifts the inferred H_0 by the same factor [Bernal et al., 2016, Knox and Millea, 2020, Poulin et al., 2019]. BAO analyses carry additional uncertainties in their distance measurements coming from (i) nonlinear evolution and scale dependent bias; (ii) tracer dependent halo occupation variations; (iii) observational effects such as fibre assignment, imaging depth or redshift failures; (iv) and from the specific template cosmology adopted in the model fit. [DESI Collaboration, 2025b]

3.2.3 One-Step Methods towards H_0

Instead of having to climb the local distance ladder, several one-step methods aim to measure H_0 directly by determining absolute distances at high redshifts. These methods don't rely on the calibration of intermediate distance

[12] BAO are sensitive to a slightly later epoch than the CMB power spectrum, namely the drag epoch ($z_d \approx 1059$), when baryons decoupled from the Compton drag of photons. This occurs after recombination ($z_* \approx 1090$). Consequently, the sound horizon at the drag epoch r_d is approximately two percent larger than that at recombination r_*.

indicators (Cepheids, TRGB, etc.), and thus are free from the associated systematics and astrophysical assumptions. As a tradeoff they therefore have larger uncertainties, but provide crucial independent cross checks of the ladder based measurements. Several one-step methods were briefly introduced in Chapter 2 as part of the modern distance ladder classification. In this section, the focus is on how these techniques are used to directly determine H_0, outlining their strengths, limitations, and current constraints.

3.2.3.1 Strong Lensing Time Delays

This method requires a variable background source, which is usually a quasar, and a strong enough gravitational lens. The light connected to the multiple images has to travel different paths in spacetime and reaches the observer at different times. Originally, Refsdal [1964] showed that the measured time delay

$$\Delta t_{AB} = \frac{D_{\Delta t}}{c}\,\Delta\phi_{AB}, \tag{3.14}$$

where $D_{\Delta t}$ is the time-delay distance, and $\Delta\phi_{AB}$ is the Fermat potential difference between images A and B. The Fermat potential consists of a geometric and a potential term,

$$\phi(\boldsymbol{\theta}) = \tfrac{1}{2}\left(\boldsymbol{\theta} - \boldsymbol{\beta}\right)^2 - \psi(\boldsymbol{\theta}), \tag{3.15}$$

where $\boldsymbol{\beta}$ is the source's angular position without lensing, $\boldsymbol{\theta}$ is the position with lensing, and ψ is the gravitational potential of the lens. The time-delay distance is given by

$$D_{\Delta t} = (1 + z_{\mathrm{d}})\,\frac{D_{\mathrm{d}}\,D_{\mathrm{s}}}{D_{\mathrm{ds}}}, \tag{3.16}$$

here D_{d}, D_{s} and D_{ds} are the angular diameter distances of the lens, source, and between lens and source, respectively. [Birrer et al., 2024] Since $D_{\Delta t}$ is an absolute distance measure, the Hubble constant can be inferred via $D_{\Delta t} \propto H_0^{-1}$.

The method uses the thin lens and single plane approximation of general relativity, the entire light deflection is caused by a two dimensional potential from the lens, and light rays are assumed to make only small angles with the optical axis. Inference of $D_{\Delta t}$ requires three practical steps [Birrer et al., 2024, Kochanek, 2002]: (1) high cadence photometry to measure the time delays precisely, (2) deep imaging and stellar velocity dispersion spectroscopy to fix the lens mass profile, and (3) a characterization of foreground and background

structure to estimate the external convergence κ_{ext}, which encapsulates the mass along the line of sight.
The principal degeneracy, the mass-sheet degeneracy (MSD) [Falco et al., 1985], arises because a uniform rescaling of the projected mass density leaves image positions unchanged, but rescales the predicted delays and hence also H_0. Combining imaging with stellar kinematics constrains the internal MSD, whereas wide-field spectroscopy or weak lensing maps help constrain κ_{ext}. Secondary systematics include microlensing, halo substructure, and various sources of measurement noise.[Birrer et al., 2024]

3.2.3.2 Gravitational Waves Standard Sirens

Mergers of neutron star (BNS) or black hole binaries (BBH) act as standard sirens. The observed strain h obeys

$$h \propto \frac{\mathcal{M}^{5/3} f^{2/3}}{D_L}, \tag{3.17}$$

where $\mathcal{M} \equiv (m_1 m_2)^{3/5}(m_1 + m_2)^{-1/5}$ is the chirp mass, the combination of the component masses that controls the frequency evolution of the inspiral, and f the GW frequency. The accumulated phase over many GW cycles depends primarily on $\mathcal{M}$, in GWTC-1 the fractional uncertainty on the chirp mass ranges from $\sim 0.1\%$ for the BNS GW170817 up to $\sim$ 15-18% for the most massive systems such as GW170729, with typical BBH events measured at the $\sim$ 3-10% level [LIGO and Virgo Collaboration, 2019]. With the chirp mass determined from the waveform, the overall amplitude contains essentially a single unknown scale. To leading order, and accounting for the detector network geometry, it provides a direct measurement of the luminosity distance D_L, although in practice it is partially degenerate with the binary's inclination [Schutz, 1986]. The luminosity distance is less constrained, with fractional uncertainties typically in the $\sim$ 25-50% range for BBH mergers and $\sim$ 20-35% for the BNS event GW170817 [LIGO and Virgo Collaboration, 2019].

To test the Hubble law one also needs a redshift. Three complementary approaches are used:

Bright sirens: If a merger produces an electromagnetic (EM) counterpart (e.g. the kilonova of GW170817), the host galaxy can be identified spectroscopically, providing a direct redshift and a single siren H_0 estimate [LIGO and Virgo Collaboration, 2017].
Dark sirens: For the more numerous BBH mergers that lack an EM signal

the redshift is obtained statistically. One may (i) correlate the GW localisation volume with a galaxy catalogue [Borghi et al., 2024] or (ii) fit a population model whose source frame mass distribution is mapped to detector frame masses through the cosmology [Farr et al., 2019]. Combining several bright and dark sirens already improves the posterior over GW170817 alone [LIGO and VIRGO Collaboration, 2021].
Spectral sirens: A sharp feature in the source frame mass spectrum of binary black holes (e.g. the pair-instability cutoff) shifts with redshift, so fitting its position across many mergers provides a redshift estimate directly from GW data and thus an independent H_0 constraint [Ezquiaga and Holz, 2022].

Systematic errors mainly come from: (i) the inclination-distance degeneracy for bright sirens [Vitale and Chen, 2018], (ii) incompleteness and photometric redshift uncertainties in host galaxies catalogues for dark sirens [Gray, 2020], (iii) uncertainty in detector strain calibration [Viets, 2018], and (iv) assumptions about the binary mass- and spin population that enter dark siren analyses [Borghi et al., 2024].

Standard sirens are among the most promising methods to independently constrain H_0, as detectors become more sensitive and the event rate (especially of bright sirens) increases.

3.2.3.3 Water Megamaser as Standard Rulers

Some active galaxies host bright water megamaser[13] moving in edge-on, nearly Keplarian disks. VLBI trace the orbital motion of the maser giving both their angular size on the sky and their line of sight velocities. For a maser spot at true radius r, the orbital velocity and centripetal acceleration follow from Newtonian dynamics,

$$v_{\parallel}(r) = \sqrt{\frac{GM_\bullet}{r}} \sin i, \qquad a(r) = \frac{GM_\bullet}{r^2}, \tag{3.18}$$

where $M_\bullet$ is the black hole mass and i the disk inclination. By combining velocity and acceleration measurements from spectral monitoring one gets the the physical radius r of the orbit. Combined with the angular separation θ from VLBI the angular diameter distance can be estimated via $D_A = r/\theta$. [Pesce and et al., 2020] Each maser galaxy therefore supplies a direct, ladder free distance measurement, which one can combine with its CMB frame recession velocity for a point in the Hubble diagram.

[13] These masers come from microwave emission due to rotational transitions of excited water molecules in dense, warm gas near active galactic nuclei.

Some important systematics include: (i) peculiar velocities of the host galaxies; (ii) disk-model systematics such as warps and inclination gradients; (iii) the small sample size of masers; and (iv) uncertainties from environmental effects if a maser galaxy is in a galaxy group whose dynamics are not well understood. [Pesce and et al., 2020]

3.2.3.4 Sunyaev-Zel'dovich (SZ) + X-Ray Cluster Distances

Inverse Compton scattering from CMB photons off hot electrons in the intracluster medium of galaxy cluster, leads to a frequency dependent change in the CMB spectrum.[14] This is called the thermal SZ effect. The actual observable is the integrated Compton parameter,

$$Y = \int d\Omega\, y(\boldsymbol{\theta}) = \frac{1}{D_A^2} \int dV\, \frac{k_B\, T_\mathrm{e}\, n_\mathrm{e}\, \sigma_T}{m_\mathrm{e} c^2}, \tag{3.19}$$

which is the line-of-sight electron pressure[15] summed over the projected area of the cluster. Here T_e and n_e are the electron temperature and density, σ_T is the Thomson cross-section [Bartelmann, 2022]. One can also observe the X-ray surface brightness of the same cluster, which is given by

$$I_X = \frac{1}{4\pi(1+z)^4} \int dl\, j_X. \tag{3.20}$$

Here, the bremsstrahlung emissivity j_X scales as $j_X \propto n_e^2 \sqrt{T_e}$.[16] If one assumes a model for the electron temperature and density profiles, the two observables from Eqs. (3.19) and (3.20) can be combined to get a measurement of angular diameter distance, and therefore the Hubble constant [Bartelmann, 2022].

The method is observationally interesting because the amplitude of the thermal SZ effect is independent of redshift, allowing high redshift cluster to contribute equally to the signal. The main systematics come from the dependence on the model of the cluster's geometry and thermodynamics. Additional complications come from gas clumping, substructure, or line-of-sight contamination, which are difficult to fully correct.[Reese, 2004]

[14] Below 217 GHz the scattering removes photons from the CMB line of sight (a temperature decrement), whereas at higher frequencies there is an increment in temperatures.

[15] Since, $n_\mathrm{e}\, \sigma_T\, dl$ is the scatter probability and $k_B\, T_\mathrm{e}/m_\mathrm{e} c^2$ is the energy gain per scatter.

[16] Bremsstrahlung is a two body process involving electrons and ions, in a fully ionized plasma, the ion density is proportional to the electron density.

3.2.3.5 Cosmic Chronometer (CC)

CC are an interesting direct cosmological probe of the Hubble function $H(z)$. CC data is also used in this work and will be dealt with in some more detail in later chapters. The method, pioneered by Jimenez and Loeb [2002], relies on the fact that one can write the Hubble parameter as

$$H(z) = -\frac{1}{1+z}\frac{dz}{dt}, \tag{3.21}$$

which shows that determining $H(z)$ reduces to estimating the differential age evolution dt of the Universe as a function of redshift dz. Since redshift is directly observable, the challenge is a reliable measure of dt, which requires a sample of astrophysical objects that act as standard clocks, or "cosmic chronometers". [Moresco et al., 2022] Then one can either parametrically or non-parametrically reconstruct $H(z=0)$ to infer the Hubble constant.

Massive ($\log M_\star/M_\odot \gtrsim 10.6$), passively, evolving galaxies make ideal CC. They formed rapidly at $z \gtrsim 2$ and have evolved quietly, so the age difference between two narrow redshift bins reflects the cosmic look-back time with minimal internal scatter. Galaxy ages are inferred from age, sensitive spectral features, most commonly the 4000 Å break, Balmer absorption lines, or full spectral fitting, calibrated against stellar-population synthesis (SPS) models. [Moresco et al., 2022]

The CC technique assumes (i) homogeneity and isotropy and (ii) that the selected galaxies share a common, nearly coeval formation epoch. The principal sources of systematic uncertainty are the degeneracy between SPS models, metallicity and the assumed initial mass function (IMF). Additional biases can arise if the supposedly passive spectra still contain even a small fraction of light from young stars, and if "progenitor bias"[17] is present. [Moresco et al., 2020a, 2018]

Future high-S/N surveys (X-Shooter, MOONS, Euclid, ATLAS Probe) promise large, uniform CC datasets and better metallicity/SPS calibration. This can lead to a model-independent H_0 measurements at the $\lesssim 3\%$ level.[Moresco et al., 2022]

3.2.3.6 Expanding Photosphere Method (EPM)

The EPM uses time-resolved spectroscopy and photometry of a single Type II SN (SN II) and converts these into a luminosity distance. The method as

[17] That is when galaxies selected at high redshift do not evolve directly into those observed at lower redshift because their star formation histories differ.

explained by Vogl et al. [2025] treats a SN II as an approximately spherically expanding shell. At each time the specific flux $f_{\lambda,\mathrm{obs}}$, from multi-band photometry, is measured, as well as the photospheric velocity v_{ph}, from the blueshift of emission features in the SN spectra. Radiative transer models are used to reproduce the observed spectrum and give the surface photospheric flux $f_{\lambda,\mathrm{em,ph}}$. Assuming spherical symmetry one can relate luminosity to radius via

$$L_{\lambda,\mathrm{em}} = 4\pi\, R_{\mathrm{ph}}^2\, f_{\lambda,\mathrm{em,ph}}. \tag{3.22}$$

In a self-similar(homologous) expansion, each layer moves at constant speed, the radius grows linearly with time and velocity,

$$R_{\mathrm{ph}}(t) = \frac{v_{\mathrm{ph}}\,(t - t_0)}{1+z}, \tag{3.23}$$

where t_0 is the time of the explosion, usually not known. It can be eliminated by defining the photospheric angular size $\theta = R_{\mathrm{ph}}/D_L = (f_{\lambda,\mathrm{obs}}(1+z)/f_{\lambda,\mathrm{em,ph}})^{1/2}$. In the end one has multiple measurements at different times of the rate of growth $\theta/v_{\mathrm{ph}} = D_L^{-1}\,(t-t_0)/(1+z)$. The slope of a fit straight line is inversely proportional to the luminosity distance and the intercept gives the explosion time t_0. Therefore, this method gives a direct distance measure and does not require external calibrators. The luminosity distance, is connected to the Hubble constant via the cosmographic expansion of Eq. (2.42). [Vogl et al., 2025] The main advantages of the EPM are, next to the one step approach, its independent systematics compared to observations of SN Ia, making it a valuable cross check. Furthermore, the EPM does not rely on any cosmological model assumptions.

The main uncertainties of the EPM come from approximations in the radiative transfer modelling and in the SN's geometry. Interactions outside the SN, assumptions about the host galaxy extinction, calibration or passband errors in the photometric system, can influence the inferred luminosity distance and therefore also H_0 at roughly few percent level. [Vogl et al., 2025]

3.2.3.7 Gamma-Ray Attenuation

Gamma-ray attenuation refers to the dimming of high-energy photons (from gamma-ray bursts or blazars) as they move through intergalactic space and collide with photons from the extragalactic background light (EBL), which is in the ultraviolet to infrared part of the spectrum. Each collision between a γ-ray and an EBL-photon produces an electron-positron pair. Therefore, the

gamma-ray signal gets dimmer, depending on the photon energies, the density of the EBL, and the distance traversed by the gamma rays. The opacity of pair production reflects the line-of-sight integral of the EBL photon field, so the energy-redshift pattern of the dimming encodes the cosmic expansion. A faster expansion shortens path lengths and reduces opacity, while the matter density shapes the redshift evolution of the EBL. [Domínguez et al., 2019] Observed blazar spectra are translated into optical depths and compared with semiempirical EBL templates embedded in a flat ΛCDM background. The energy at which the optical depth reaches unity defines the cosmic gamma-ray horizon, i.e. the distance beyond which the universe becomes opaque to gamma-rays due to the damping of EBL. With a Bayesian approach, varying H_0 and $\Omega_{m,0}$, and marginalizing over nuissane parameters describing the evolving EBL emissivity, one can constrain the Hubble constant that best fits the observed pattern.[Domínguez et al., 2019] The method can probe very high redshifts (up to $z \approx 5$). The main systematics stem from the accurate modelling of the EBL, and the assumptions on the source's spectra. Currently, there is only a limited number of events, but future gamma-ray telescopes like the Cherenkov Telescope Array will improve statistics and energy reach. [Perivolaropoulos, 2024].

3.2.3.8 Sound Horizon at Matter-Radiation Equality

Instead of using the sound horizon at recombination one can also use the sound horizon at a different epoch, e.g. the matter radiation equality at z_{eq}. The method uses the fact that the comoving wavenumber k_{eq} fixes the turnover of the linear matter power spectrum. In ΛCDM this scale obeys $k_{\mathrm{eq}} \propto \Omega_{m,0}^{1/2} H_0$. By fitting the shape of the galaxy power spectrum, marginalizing over the oscillatory BAO component, one isolates k_{eq}, and for $\Omega_{m,0}$ complementary SN data is used, this in combination fixes H_0. [Philcox et al., 2022]

Because the matter radiation equality horizon is fixed by the background expansion once radiation stops to dominate, its scale is largely immune to modifications of pre-recombination physics. The method assumes a flat ΛCDM model. Observationally, the turnover wavenumber must be isolated from galaxy power spectra on quasi-linear scales: perturbative corrections, scale-dependent bias, redshift-space distortions and survey window effects all have to be controlled. Wrongly modelled non-linear behavior can shift k_{eq} and therefore H_0. [Philcox et al., 2022].

3.2.3.9 Breaking the BAO $r_d - H_0$ Degeneracy

In recent years there has been efforts to break the $r_d - H_0$ degeneracy in BAO data, by using complementary cosmological probes. Krolewski et al. [2025] developed a method to measure H_0 independently from the sound horizon by a bunch of energy density measurements. They combine Big Bang Nucleosynthesis (BBN) for an estimate of $\Omega_b h^2$. For the baryon-to-matter ratio they look at the amplitude of the baryonic wiggles in the small scales of the galaxy power spectrum. And they obtain Ω_m from Alcock-Paczynski data from BAO combined with cosmic void shapes. These four measurements of energy densities can be inserted into the relation for the critical density $3c^2 H_0^2/8\pi G = \epsilon_{\gamma,0}\,(\epsilon_b/\epsilon_\gamma)\,(\epsilon_m/\epsilon_b)\,\Omega_m^{-1}$ to constrain H_0. Pogosian et al. [2024] use the transverse BAO scale at multiple redshifts and assume a flat ΛCDM cosmology. Then they use an additional prior on $\Omega_m h^2$ from CMB data to break the $r_d - H_0$ degeneracy. Liu et al. [2025] combine BAO data with strong lensing distances for a model independent reconstruction of the sound horizon, which then can be used to infer H_0. Schöneberg et al. [2019] use data from BBN to infer the sound horizon as an independent anchor of the BAO data. Heavens et al. [2014] break the degneracy by anchoring the BAO data with Cosmic Chronometers.

For an extensive review of H_0 measurements and more details see Di Valentino et al. [2025].

3.3 Measured values of H_0 and the Hubble Tension

Figure 3.3 provides an overview of the current state of H_0 measurements, that were discussed in previous section. The results are plotted in the order in which they were discussed in section 3.2. The most striking feature of Figure 3.3 is the systematic offset between the locally measured values of H_0 and the values inferred from the indirect, model-dependent methods, a discrepancy known as the **Hubble tension**. Two particular measurements are highlighted. Firstly, the value obtained by Riess et al. [2022] (R22) (orange vertical band in Fig. 3.3) using Cepheid calibrated SN gives

$$H_0^{\mathrm{R22}} = 73.04 \pm 1.04\,\mathrm{km\,s^{-1}\,Mpc^{-1}}, \tag{3.24}$$

secondly the CMB value by Planck Collaboration [2018] (P18) (blue vertical band in Fig. 3.3) under the assumption of ΛCDM yields

$$H_0^{\mathrm{P18}} = 67.4 \pm 0.5\,\mathrm{km\,s^{-1}\,Mpc^{-1}}. \tag{3.25}$$

These two values famously differ by over 5σ. It is widely discussed in literature and some possible solutions to the tension will be reviewed in the next section.

Another clear trend in the H_0 measurements is the variation in uncertainty across different methodological categories (see Tab. 3.1). The model dependent, indirect methods typically have the largest error bars, with relative uncertainties below 1%. The distance ladder estimates are intermediate in precision, with uncertainties around $1-4\%$ depending on the calibration and anchoring technique used. One-step methods generally show the largest uncertainties, with relative errors of $4-20\%$, but they benefit from independent systematics and are largely free from calibration and model dependencies.

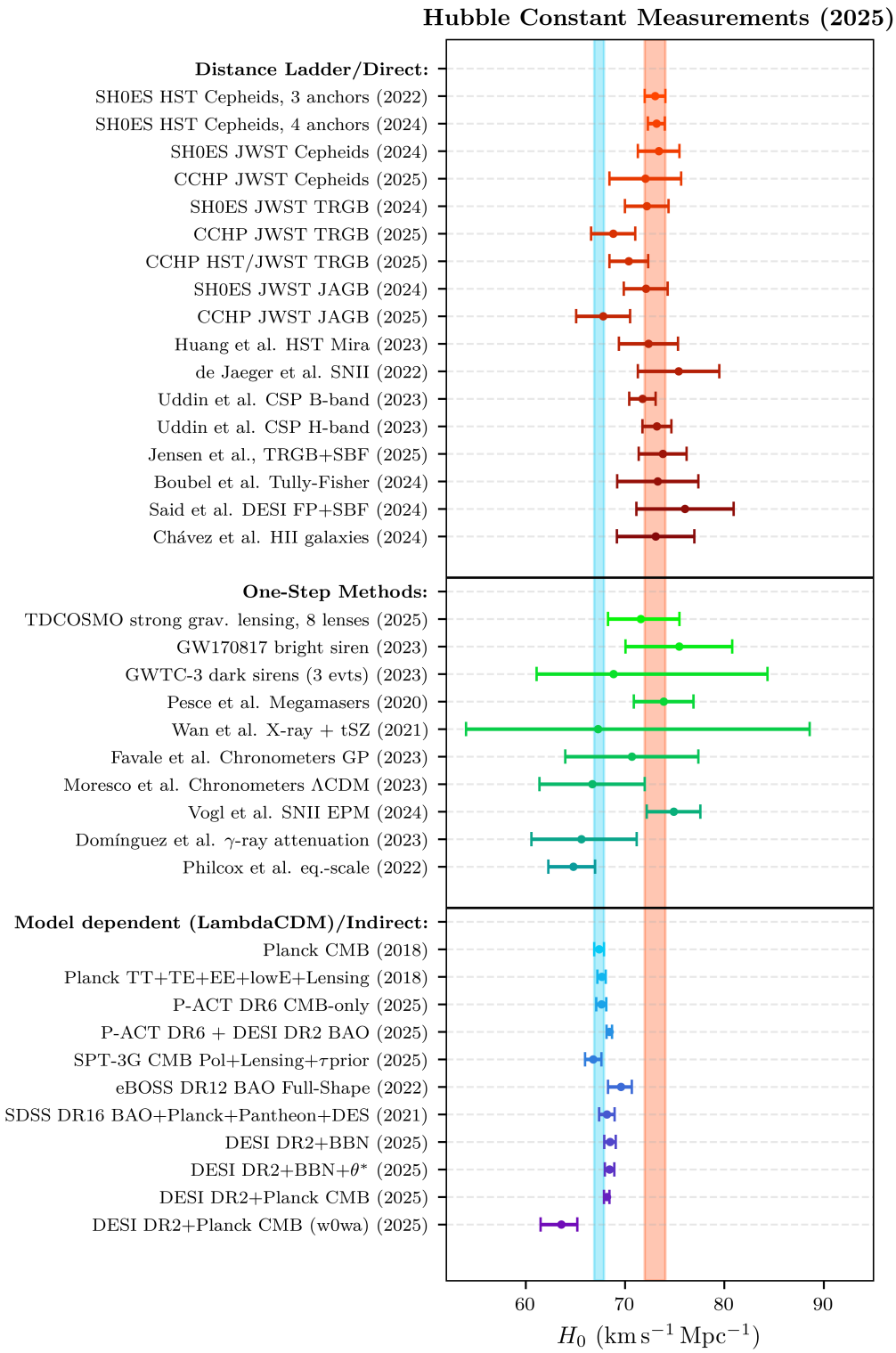

Figure 3.3: *Overview of the most recent H_0 measurements discussed in this work.*

Measurement (Year)	H_0 [$\mathbf{km\,s^{-1}\,Mpc^{-1}}$]	**Source**
Distance Ladder / Direct		
SH0ES HST Cepheids, 3 anchors (2022)	73.04 ± 1.04	Riess et al. [2022]
SH0ES HST Cepheids, 4 anchors (2024)	73.2 ± 0.9	Riess et al. [2024]
SH0ES JWST Cepheids (2024)	73.4 ± 2.1	Riess et al. [2024]
CCHP JWST Cepheids (2025)	72.05 ± 3.60	Freedman et al. [2025]
SH0ES JWST TRGB (2024)	72.2 ± 2.2	Riess et al. [2024]
CCHP JWST TRGB (2025)	68.81 ± 2.22	Freedman et al. [2025]
CCHP HST/JWST TRGB (2025)	70.39 ± 1.94	Freedman et al. [2025]
SH0ES JWST JAGB (2024)	72.1 ± 2.2	Riess et al. [2024]
CCHP JWST JAGB (2025)	67.80 ± 2.72	Freedman et al. [2025]
Mira HST (Huang 2024)	72.37 ± 2.97	Huang et al. [2024]
Type II SN (de Jaeger 2022)	75.4 ± 4.1	de Jaeger et al. [2022]
CSP HST B band (2023)	71.76 ± 1.33	Uddin et al. [2023]
CSP HST H band (2023)	73.22 ± 1.45	Uddin et al. [2023]
Jensen TRGB+SBF (2025)	73.8 ± 2.4	Jensen et al. [2025]
Boubel TF+Cep+TRGB (2024)	73.30 ± 4.08	Boubel et al. [2024]
Said DESI FP+SBF (2024)	76.05 ± 4.90	Said et al. [2025]
Chávez HII L-σ (2024)	73.1 ± 3.9	Chávez et al. [2025]
One-step		
TDCOSMO strong grav. lensing (2025)	$71.6^{+3.9}_{-3.3}$	Birrer et al. [2025]
GW170817 bright siren (2023)	$75.46^{+5.34}_{-5.39}$	Palmese et al. [2024]
GWTC-3 dark sirens (3 evts, 2023)	$68.84^{+15.5}_{-7.7}$	Alfradique et al. [2024]
Megamaser CP (2020)	73.9 ± 3.0	Pesce and et al. [2020]
X-ray+tSZ clusters (2021)	$67.3^{+21.3}_{-13.3}$	Wan et al. [2021]
Cosmic Chronometers (GP, 2023)	70.7 ± 6.7	Favale et al. [2023]
Cosmic Chronometers (ΛCDM, 2023)	66.7 ± 5.3	Moresco [2023]
SN II EPM (distance-ladder-free, 2024)	74.9 ± 2.7	Vogl et al. [2025]
γ-ray attenuation (2023)	$65.6^{+5.6}_{-5.0}$	Domínguez et al. [2024]
Equality-scale (BOSS+CBL, 2022)	$64.8^{+2.2}_{-2.5}$	Philcox et al. [2022]
Model-dependent / Indirect (ΛCDM)		
Planck CMB (2018)	67.4 ± 0.5	Planck Collaboration [2018]
Planck TT+TE+EE+lowE+Lens (2018)	67.66 ± 0.42	Planck Collaboration [2018]
ACT DR6 CMB (2025)	67.62 ± 0.50	Louis et al. [2025]
ACT DR6 + DESI DR2 BAO (2025)	68.43 ± 0.27	Louis et al. [2025]
SPT-3G Pol+Lens+τ (2025)	66.81 ± 0.81	Ge et al. [2025]
eBOSS DR12 Full-Shape BAO (2022)	$69.6^{+1.1}_{-1.3}$	Philcox and Ivanov [2022]
SDSS DR16 BAO+Planck+DES (2021)	68.18 ± 0.79	Alam et al. [2021]
DESI DR2+BBN (2025)	68.51 ± 0.58	DESI Collaboration [2025d]
DESI DR2+BBN+θ_* (2025)	68.45 ± 0.47	DESI Collaboration [2025d]
DESI DR2+Planck CMB (2025)	68.17 ± 0.28	DESI Collaboration [2025d]
DESI DR2+Planck (w_0w_a, 2025)	$63.6^{+1.6}_{-2.1}$	DESI Collaboration [2025d]

Table 3.1: *Recent H_0 determinations in the order they are described in this work. Quoted uncertainties are 1σ.*

Tension in Calibrators/Anchors

The Hubble tension can be understood as a tension in the calibrators (or anchors). As shown in section 3.2.1 the Hubble constant from the distance ladder is degenerate with the calibration of the absolute magnitude (see Eq. (3.4)) and H_0 from the inverse distance ladder is degenerate with the value of the sound horizon (see Eq. (3.11)). The SH0ES collaboration cal-

ibrates an absolute magnitude of $M_B^{\mathrm{R22}} = -19.253 \pm 0.027\,\mathrm{mag}$. Whereas, Gómez-Valent [2022] combine CMB, BAO, and uncalibrated SNe Ia under ΛCDM to find $r_d^{\mathrm{P18}} = 147.17 \pm 0.20\,\mathrm{Mpc}$ and a corresponding absolute magnitude of $M_B = -19.403 \pm 0.010\,\mathrm{mag}$, this value of M_B is again in $\sim 5\sigma$ tension with M_B^{R22}. This tension, is visually presented in Figure 3.4, taken from Gómez-Valent et al. [2024, Fig. 1]. To resolve the tension, it is clear that either the sound horizon inferred from early-universe physics must be reduced, the locally calibrated absolute magnitude must be lowered (i.e it has some constant positive offset), or both values must shift toward each other to reach agreement with the data. These possibilities will be explored in the next section.

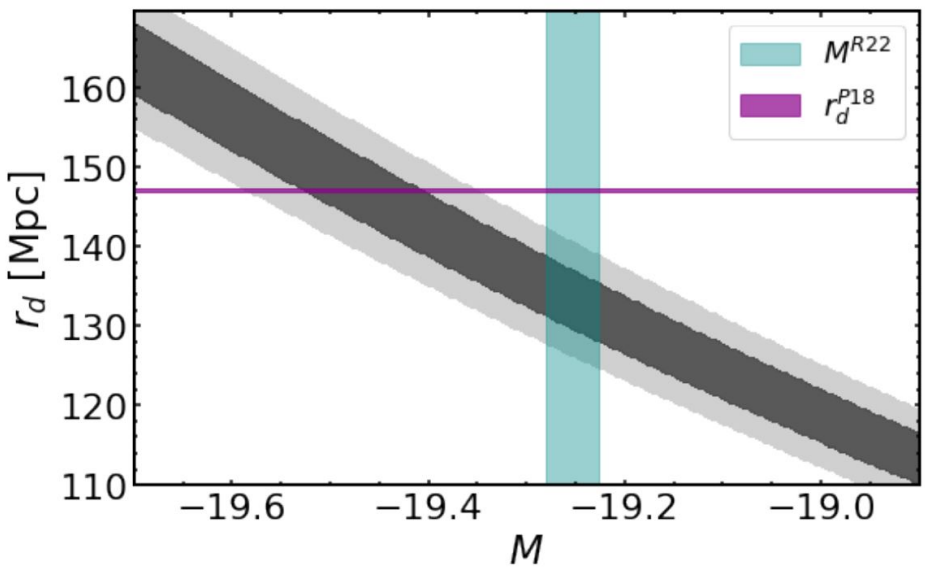

Figure 3.4: *Hubble tension in terms of the calibrators, the absolute magnitude M and the value of the sound horizon r_d. The grey band shows the degeneracy band from uncalibrated BAO and SN. Figure taken from Gómez-Valent et al. [2024, Fig. 1].*

3.4 Resolutions to the Tension

The current discrepancy between early- and some late-time measurements of H_0 has inspired a long list of potential resolutions. They fall into two categories: (i) experimental or methodological approaches that revisit calibration procedures, data reduction, astrophysical assumptions and possible

unaccounted systematics and (ii) theoretical explanations or changes in fundamental physics. This section aims to give a broad overview.

3.4.1 Experimental/Methodological Approaches

Before integrating new physics, it is natural to ask whether unrecognized systematics could still account for (part of) the $\sim 10\%$ gap between early- and late-time measurements of H_0.

3.4.1.1 Systematics in the Distance Ladder

- **Geometric Anchors:** The geometric measurements of first rung are pretty solid and currently limited by (i) GAIA parallaxes for Milkyway calibrators (ii) geometric distances to anchor galaxies like the LMC and NGC 4258. GAIA DR3 measures parallaxes extremely precise and leaves a residual parallax bias of $\lesssim 4, \mu$as [Lindegren et al., 2021]. For bright Cepheids specifically, the DR3-HST comparison indicates an additive offset of $-14 \pm 6\,\mu$as, which propagates to only a $\sim 0.4\%$ scale error in distance [Breuval et al., 2025]. Currently, there is an ongoing debate regarding a magnitude-space recalibration of GAIA parallaxes proposed by Madore et al. [2025]. Their method modifies how GAIA parallax zero-points are treated, effectively flattening the observed Cepheid metallicity dependence in the period-luminosity relation. This adjustment would increase the inferred value of H_0 by approximately 1%. However, Breuval et al. [2025] challenge this approach. They argue that such a magnitude-space correction is inconsistent with both Cepheid distances derived from open clusters and the resulting negative parallaxes in GAIA data. In 2026 GAIA DR4 will probably settle this issue with improved parallax measurements. The distance to the LMC, as an important anchor galaxy to calibrate secondary indicators, is very robustly measured with a relative precision below 1% accuracy, using a system of 20 detached eclipsing binaries (DEBs) [Pietrzyński et al., 2019]. For NGC 4258, Reid et al. [2019] measure a very precise geometric distance, within 1.5%, using masers. Taken in combination GAIA parallaxes, LMC distance from DEBs, and NGC 4258 distance from masers in the SH0ES ladder contribute $1.35\ \mathrm{km\,s^{-1}\,Mpc^{-1}}$ to the final uncertainty in H_0 [Riess et al., 2022].
- **Secondary indicators:**
  1. **Cepheid ladder and photometric zeropoints:** Crowding, zeropoint, and bandpass errors in HST Cepheid photometry were

long-suspected biases. A JWST cross-check of approximately 1000 Cepheids in NGC 4258 and five SN Ia hosts finds an HST-JWST mean offset of only 0.03 mag, too small to resolve the Hubble tension [Riess et al., 2024]. Using only JWST data, SH0ES obtains $H_0 = 73.4 \pm 2.1$ (Cepheids). JWST also reduces the period-luminosity dispersion by a factor of 2.5 and rules out HST crowding bias at the 8.2 sigma level [Riess et al., 2024]. Metallicity corrections from GAIA, with a value of about $-0.25\,\mathrm{mag\,dex}^{-1}$ [18] are now consistently applied. These corrections affect H_0 by only about 0.5 km s^{-1} Mpc^{-1} [Breuval et al., 2024].

2. **Population-II calibrators and host-galaxy selection:** The Chicago-Carnegie program (CCHP) uses Population-II tracers that are less sensitive to dust and metallicity. With 24 SN Ia hosts (HST and JWST), CCHP finds $H_0 = 70.39 \pm 1.94$ from the combined HST and JWST TRGB. Using only JWST TRGB gives $H_0 = 68.8 \pm 2.2$, and using only JWST JAGB yields $H_0 = 67.8 \pm 2.72$ [Freedman et al., 2025]. In comparison, Riess et al. [2024] find $H_0 = 72.2 \pm 2.2$ (JAGB) and $H_0 = 72.1 \pm 2.2$ (TRGB). The roughly $3\,\mathrm{km\,s}^{-1}$ Mpc-1 gap between CCHP and SH0ES may point to residual stellar-population or SN host selection effects.[19] Completing JWST imaging of the remaining HST SN Ia hosts, and adding new TRGB and JAGB calibrators, will be critical. Using JWST TRGB-calibrated surface brightness fluctuations (SBF), SH0ES independently obtains $H_0 = 73.8 \pm 2.4$ without relying on SN Ia [Jensen et al., 2025].

3. **Indicator hierarchy:** Despite sharing a geometric zero-point, a ranking persists among indicators: Cepheids > TRGB $\gtrsim$ JAGB, in both CCHP and SH0ES analyses. This is plausible since the tracers probe different stellar populations and face different systematics. Cepheids are young, metal-rich, and affected by crowding, while TRGB and JAGB stars are older, metal-poor, and mostly dust-free, but they require precise color and metallicity corrections (and age corrections for JAGB). Whether the observed offsets reflect residual crowding or dust in Cepheids, subtle metallicity effects in TRGB/JAGB, or SN host selection remains under debate. Two newly recognized TRGB systematics, i.e. edge de-

[18] An increase of 1 dex corresponds to a tenfold increase in the iron-to-hydrogen ratio.

[19] SH0ES argues that selecting a smaller host galaxy sample in JWST observations (as done by CCHP) biases the CCHP H_0 value.

tection bias and halo dust extinction, can shift H_0 by about 1 percent [Anderson et al., 2024].

4. **SN Ia standardization:** The standardization of SN Ia magnitudes also impacts H_0 when derived from the distance ladder. SN Ia peak luminosities correlate with host galaxy mass, star formation rate (SFR), and local environment. Light curve standardization methods such as SALT3, applied to the Pantheon+ sample with matched calibrator and Hubble flow selections, reduce host biases to about 0.05 mag. However, omitting empirical corrections like the mass step or local SFR can shift H_0 by 0.5 percent [Brout et al., 2022]. When combined with cross-survey zeropoint calibration and light curve model retraining, SN Ia systematics contribute roughly 0.5 km s^{-1} Mpc^{-1} to the total SH0ES uncertainty budget [Riess et al., 2022]. A sharp shift in absolute magnitude could also occur at very low redshifts (z less than 0.01), possibly due to differences in SN standardization between the calibrator and Hubble flow samples. For example, a mismatch in the color correction or Tripp calibration applied to the two samples could induce a systematic offset in M_B. If the SH0ES calibrated M_B were about 0.2 mag brighter than the true Hubble flow value, it could explain the difference between the SH0ES and Planck H_0 determinations [Gómez-Valent et al., 2024].

Although plenty rigorous cross checks of anchors, Cepheid/TRGB photometry, and SN Ia standardization have moved individual systematics to the sub-percent level, the distance ladder may still be effected by unidentified local effects. Such a local bias, like a photometric zeropoint drift, crowding/reddening effect, or large-scale environmental anomaly, could be imprinting an offset across all rungs of the ladder simultaneously [Perivolaropoulos, 2024].

3.4.1.2 Systematics from the CMB/BAO

H_0 inferred from the CMB is sensitive to instrumental systematics, calibration uncertainties, and most importantly cosmological model assumptions. Planck's self consistency check using cross frequency calibration limits hidden offsets to $\lesssim 0.3\%$ [Planck Collaboration, 2018]. Independent CMB experiments like ACT and SPT-3G provide a cross check on Planck's measurements. Although, they have differences in instrumentation, angular res-

olution, calibration pipelines, and sky coverage, they all recover consistent cosmological parameters within 1σ. Notably, both ACT DR6 [Hill et al., 2025] and SPT-3G [Balkenhol et al., 2023] measure a slightly higher value of H_0. Yet, the overall agreement suggests that instrumental systematics are well controlled across CMB measurements.

One plausible way to soften the ladder mismatch is that model-dependent assumptions in reconstructing the anisotropic 3-dimensional BAO peak could bias the recovered BAO measurements, if present and removed could help soften the tension between BAO/CMB anchors and SN calibrators. Therefore, also testing on 2-dimensional BAO data is important. [Gómez-Valent et al., 2024] Recent BAO measurements show a mild tension with Planck (smaller tension with ACT and SPT-3G), typically favoring a higher H_0 by $\sim$ 1-1.5 $\mathrm{km\,s^{-1}\,Mpc^{-1}}$. The completed BOSS/eBOSS DR12 full-shape analysis yields $H_0 = 69.6^{+1.1}_{-1.3}$ $\mathrm{km\,s^{-1}\,Mpc^{-1}}$ [Philcox and Ivanov, 2022], while the latest DESI DR2 BAO data combined with a BBN deuterium prior returns $H_0 = 68.51 \pm 0.58$ $\mathrm{km\,s^{-1}\,Mpc^{-1}}$ [DESI Collaboration, 2025d]. The $\sim 2\sigma$ offset between DESI DR2 and Planck's data suggests either residual modelling systematics in late-time clustering or the need for theoretical extensions of ΛCDM, which will be briefly mentioned in Sec. 3.4.2.

3.4.1.3 Systematics in the One-Step Methods

Each of the one-step method carry their own independent systematics. Currently, all the one-step methods still have relatively large uncertainties, in the approximately $5-10\%$ regime, compared to the distance ladder and measurements based on CMB/BAO. A range of new detectors and better statistics - from the Vera Rubin Observatory LSST (strong lensing and electromagnetic GW counterparts) and Euclid (particularly for cosmic chronometers and strong lensing systems), the upgraded ground based GW network (Advanced Ligo, Einstein Telescope, Cosmic Explorer) and space observations from LISA (for standard sirens), the next-generation Very Large Array and the Square Kilometer Array (megamasers), and the Cherenkov Telescope Array (γ-ray attenuation) - will hopefully push each method below the 5% level in accuracy to provide multiple independent constrains on the Hubble tension.

After a decade of intensive re-calibration, the combined effect of all known experimental and methodological seems unlikely to erase the full tension in H_0. The conclusion of Di Valentino et al. [2025] is that the Hubble tension almost certainly cannot be explained by experimental errors alone and will likely require new physics or a coherent late-time effect.

There seems to be a mild $\sim 2\sigma$ inconsistency between DESI DR2 BAO data and CMB data from Planck under ΛCDM assumptions. This discrepancy does not map directly onto a single parameter like H_0, but rather suggests a broader mismatch in the parameter space, particularly related to the sound horizon and expansion history. Interestingly, the tension can be alleviated in extended cosmological models, such as those allowing for time-varying dark energy (e.g. $w_0 w_a$CDM with phantom crossing), which bring both datasets into agreement again. This supports the possibility that new physics, such as dynamical dark energy, early dark energy, or modifications to gravity, may be required to consistently explain both BAO and CMB observations.[Ye and Lin, 2025]

3.4.2 Theoretical Solutions

In the recent years a large range of theoretical models has emerged to (also) explain the Hubble tension. This section is not complete and is only supposed to give a broad overview. For more details on the theoretical solutions see Di Valentino et al. [2021] or Di Valentino et al. [2025].

3.4.2.1 Early Time Modifications

All proposals in this category aim to decrease the sound horizon at recombination r_* (see Eq. (3.6)) by increasing the expansion rate in the pre-combination time, so that the observation of the CMB angular scale θ_* stays the same, but H_0 from indirect measurements gets raised (see Eq. (3.11)) by the required $\sim 7\%$. However, Jedamzik et al. [2021] showed that models who lift H_0 only by shrinking the sound horizon typical clash with BAO or galaxy-lensing measurements, so they cannot by themselves provide a complete resolution to the tension. Still, the search for a smaller sound horizon as inspired a variety of early-time proposals, which will be broadly described in the following section.

Early Dark Energy (EDE): EDE models add an extra energy component, typically an axion-like scalar, which behaves like dark energy (w $\simeq -1$), while the field is frozen by the Hubble friction. As the universe expand and H drops to the mass of the field ($H \sim m_\phi$), the field rolls toward its minimum, enters oscillations ($w \simeq +1$), and its energy density quickly dilutes. With this mechanism the field contributes a few per cent to the total energy density before recombination to speed up the expansion enough to decrease the sound horizon, but doesn't leave a significant impact on late times. The

observational bounds from different observables on EDE models are tightening.[20] Combined CMB, BAO and SN data constrain $f_{\mathrm{EDE}} \lesssim 0.06$, which in turn limits the boost in the Hubble constant to $\Delta H_0 \lesssim 3\,\mathrm{km\,s^{-1}\,Mpc^{-1}}$. [Di Valentino et al., 2025] For an observational review see McDonough et al. [2024] and for a theoretical review of EDE see Poulin et al. [2023].

New Early Dark Energy (NEDE): Unlike axion-like EDE, relying on a slowly rolling scalar filed, NEDE assumes a fast (first order) phase transition between BBN and recombination. A heavy field initially sits in a false vacuum, producing an early dark energy plateau. Once a trigger (either ultralight scalar in "cold" NEDE, or the cooling of the dark sector in "hot" NEDE) activates, the potential barrier collapses, bubbles of the true vacuum nucleate and the false vacuum energy disappears, injecting energy into the plasma, leading to a fast expansion and thereby decreasing the sound horizon. [Di Valentino et al., 2025] In practice the mechanism can lift the CMB inferred Hubble constant to $H_0 \simeq 70\text{-}72\ \mathrm{km\,s^{-1}\,Mpc^{-1}}$ [Garny et al., 2025, Niedermann and Sloth, 2021].

Extra Relativistic Species: The early expansion rate can also be increased by adding a light ultra-relativistic component, therefore increasing the radiation density. This extra radiation energy density is captured by the effective number of neutrinos ΔN_{eff}. This quantity positively correlates with the Hubble constant, via $H_0 \simeq 5.9\,\Delta N_{\mathrm{eff}}$ [Di Valentino et al., 2025]. From this it is clear that to achieve the desired high H_0, one would require $N_{\mathrm{eff}} \gtrsim 4$, which is experimentally ruled out. Planck data combined with SDSS BAO and Pantheon SN Ia give $N_{\mathrm{eff}} = 2.99 \pm 0.17$, $H_0 = 67.4 \pm 1.1\ \mathrm{km\,s^{-1}\,Mpc^{-1}}$ [Planck Collaboration, 2018]. The latest DESI DR2 BAO, combined with Planck PR4 + ACT, prefer a slightly higher value $N_{\mathrm{eff}} = 3.23 \pm 0.18$ and $H_0 = 69.2 \pm 1.0\ \mathrm{km\,s^{-1}\,Mpc^{-1}}$ under ΛCDM [DESI Collaboration, 2025a]. While CMB data from ACT DR6 alone gives $N_{\mathrm{eff}} = 2.86 \pm 0.13$, and combined with BBN $N_{\mathrm{eff}} = 2.89 \pm 0.11$ [Hill et al., 2025].

Changes in Recombination Physics: Instead of adding new energy components, the sound horizon can also be shortened by changing the microphysics of recombination. To releave the Hubble tension recombination would have to happen earlier. Mirpoorian et al. [2025] used a phenomenological model to show that such a shift in principle can alleviate some of the Hubble tension. Some physical ideas to make recombination happen earlier

[20] But, as it happens in theoretical physics, theories can be tweaked to evade given experimental bounds over and over again.

include primordial magnetic fields, which lead to baryons clumping together and recombination happen faster [Jedamzik and Pogosian, 2020], or a hypothetical interaction with a dark component could cool the baryon-photon fluid quicker.

Varying Fundamental Constants: Small changes in the fine-structure constant α_{EM} or the effective electron mass m_{e} change the hydrogen binding energy, Thomson scattering, and therefore the recombination timeline. Speeding up recombination shortens the sound horizon and can therefore in principle also raise H_0 from the indirect measurements. A recent analysis by Toda and Seto [2025] has combined Planck CMB, Pantheon+ SN and DESI DR2 BAO data to tighten the joint limits on early-time changes of both α_{EM} and m_e. They find that DESI's new BAO points slightly favor a heavier effective electron mass while leaving α_{EM} fully consistent with being constant. Yet, the percent level variations needed for the Hubble tension remain excluded by this approach, but it can help bring the values of early- and late-times closer together.

3.4.2.2 Late Time Modifications

A broad range of proposals aiming to resolve the Hubble tension involves modifying the expansion history at low redshifts, leaving the observed CMB acoustic scale intact but boosting the model dependent H_0 from the indirect measurements to the high local scale by SH0ES. However, the late time solutions face some severe challenges. Firstly, SH0ES does not directly measure H_0, rather they calibrate the absolute magnitude of SN via their distance ladder and then convert this into a value of H_0 using the cosmographic expansion in a Hubble flow section $0.023 < z < 0.15$, i.e. this is not a measurement of $H(z \to 0)$ [Efstathiou, 2021]. Yet, this is what some solutions put as prior on the SH0ES H_0, without checking if their model is actually fitting the SN data. Any model must fit both the locally calibrated M_B and the complete SN + BAO + CMB distance data, but this is where many theories fail since the absolute magnitude required to fit the SN + BAO + CMB data is incompatible with the absolute magnitude calibrated by the SH0ES team (required shift of $\sim 0.2\,\mathrm{mag}$). Ideas that just fix the tension in the value of H_0, but leave the tension in M_B unadressed cannot be considered solutions to the Hubble tension. It is likely that late-time solutions, similarly to early-time solutions, cannot individually resolve the full tension. Potentially, a combination of effects is required. In the following a brief overview is given of the main late-time approaches, that can atleast partially alleviate some of the tension.

Late Dark Energy (LDE): As the name makes clear, LDE models change the expansion at low redshifts (typically $z \lesssim 1$). This is usually done by letting $w(z)$ vary from the cosmological constant value of $w = -1$, including scenarios with transitions from quintessence into the phantom regime. [Di Valentino et al., 2025] As described above such modifications can raise the value of H_0 based on a cosmological model, but they face 2 major issues: (i) fitting both the absolute magntiude of calibrated SN and BAO/CMB data simultaneously and (ii) not introducing new tensions with large-scale structure observations. Using most recent SN, BAO and CC data, Zhou et al. [2025] show that even the most flexible late-time $w(z)$ deformations can lift H_0 only to $\sim 69\,\mathrm{km\,s^{-1}\,Mpc^{-1}}$ before clashing with the SN Ia data.[21] As such LDE models are unlikely to fully resolve the tension on their own.

Sign-Switching Dark Energy These ideas propose a dark energy density that has been negative at early times ($z \gtrsim 2$), transitioning to a positive value recently, naturally raising H_0 while preserving consistency with CMB and BAO. An analysis by Akarsu et al. [2023] shows that the Λ_sCDM model, featuring such a sign flip near $z^\dagger \sim 1.8$, can simultaneously alleviate tensions in H_0, M_B, S_8, Ly-α BAO, ω_b, and the cosmic age, while providing a better fit to Planck, Pantheon, and BAO data than standard ΛCDM.

Interacting Dark Energy (IDE): IDE solutions allow an energy exchange between dark energy and dark matter. The introduced coupling term leads to a modified background evolution which in principle can raise H_0, without changing early-time physics. The form of the interaction is usually phenomenological, and the directions of energy flow changes a lot the dynamics and viability of the models. While some IDE scenarios can bring H_0 to a higher value, they often struggle to simultaneously fit SN and full BAO constrains. Also, to stay within physically acceptable energy densities and avoiding instabilites requires careful tuning of the interaction form. [Di Valentino et al., 2025]

Modified Gravity (MG): MG frameworks address the Hubble tension by using the extra dynamical degrees of freedom that appear once the Einstein-Hilbert action is extended or its foundational principles are relaxed. In theories like $f(R)$ gravity or their scalar-tensuor duals a non-minimal coupling between the scalar sector and curvature induces a redshift dependent "effective" Hubble constant $H_0^{\mathrm{eff}}(z)$ that converges to the CMB value at high

[21] Of course under the premise that there are no unaccounted systematics in the data sets used.

z and matches the higher local distance ladder value. Horndeski subclasses that survive the GW170817 speed constraint, e.g. the cubic Galileon, achieve a similar late-time rescaling. For the teleparallel branch, simple power-law $f(T)$ models boost the expansion rate and can ease the H_0 tension. Massive gravity and bimetric gravity can also shift H_0. Conclusively, even though a lot of the models have the possibility of allowing for a higher H_0, this does not mean they resolve the cosmological tension, since many of them have troubles to be consistent with solar system tests, CMB lensing and BAO data. Furthermore, even though they offer a rich theoretical model space[22], they often require fine-tuning and introduce instabilities. [Di Valentino et al., 2025] Yet, they remain interesting scenarios to explore to help partially resolve some of the cosmological tensions with new physics.

Local Void: An interesting approach to change all rungs of the distance ladder in a coherent matter would be the presence of a local void. In the presence of a local void the reduced gravitational pull would lead a higher local expansion rate. So, at a given true luminosity distance objects would show an increased redshift compared to a FLRW universe. If one interprets these higher redshifts with the standard FLRW distance-redshift relation, distances would be underestimated. That would steepen the Hubble diagram resulting in an artifically higher H_0. Infrared galaxy counts and K-band luminosity-density measurements showed a possible $\sim 20\%$ underdensity extending to $\sim 300\,\mathrm{Mpc}$ around the Local Group, sufficient raise the inferred H_0 by several $\mathrm{km\,s^{-1}\,Mpc^{-1}}$ [Keenan et al., 2013]. However, Haslbauer et al. [2020] show that a such an underdensity is extremely unlikely under ΛCDM, which leads them to explore alternatives like Milgromian dynamics with sterile neutrinos, which can accomodate the void, local SN and lensing measurements aswell as CMB anisotropies. Recent BAO fits to isotropic D_V measurements reduce the DESI BAO - Planck CMB tension to 1σ using void models as a possible explanation [Banik and Kalaitzidis, 2025]. However, several studies have shown that data from Pantheon SN do not support the local void hypothesis as a viable sole resolution to the Hubble tension [Cai et al., 2021, Kenworthy et al., 2019, Luković et al., 2020]. Also a more recent analysis by Stiskalek et al. [2025] based on a direct distance indicator Tully-Fisher sample found that void models are disfavored by the data to resolve the tension completely.

Local Physics Solutions: Instead of changing the global cosmological model, some authors try to tackle the Hubble tension by local modifications of gravitational physics or local effects in the expansion. A possibility is

[22] A blessing and an abyss at the same time.

a smooth evolution of the SN absolute magntiude $M_B(z)$, together with a slight late-time modified expansion rate, proposed by Alestas et al. [2021].[23] In this framework, H must increase at low redshifts to match the SH0ES value and then dip below ΛCDM at higher z to preserve the BAO measurements and the angular distance to the angular diameter distance to the CMB. This would also require a redshift dependence in $M_B(z)$ to remain consistent with the full distance ladder, avoiding tensions at intermediate redshifts. [Gómez-Valent et al., 2024]

Rotating Universe: An intriguing idea for the Hubble tension, that has recently received renewed attention, is a rotating universe, as originally proposed by Gödel [1947]. In such a Gödel solution[24] a global rotation twists spacetime everywhere, so that light travelling through it picks up an extra Doppler-like redshift component beyond the usual expansion. So that objects at a given true distance appear to recede faster than in a non-rotating FLRW universe. Analysis by Szigeti et al. [2025] obtains an angular speed today of $\omega_0 \lesssim 0.002\,\mathrm{Gyr}^{-1}$ (roughly one turn in 10^{12} yr)[25] that would resolve the Hubble tension, while being consistent with local measurements. In further investigations they want to test their models using rotating N-body simulations to also constrain other cosmological parameters [Szigeti et al., 2025]. A similar analysis by Verma et al. [2025] also favors a rotating cosmology, influencing the late-time expansion. Future modelling and observations may provide improved constraints on the rotation parameter and the anisotropy axis.

Large-Scale Inhomogeneity: If we sit inside (or just outside) a very extended density pertubation, the light we use to calibrate local distances would experience a different background than the one probed by the CMB. A toy model for this is the McVittie metric [McVittie, 1933], which follows a Schwarzschild metric near a point mass to FLRW at large radii. Photon geodesics through such a space naturally shift the luminosity-distance relation in a way that can raise the locally inferred H_0. For the effect to matter, the inhomogeneity must be enormous, comparable to a supercluster in mass or a gigaparsec void, so that the gravitational field is nearly uniform across our surveys.[26] Since only tidal gradients are observable in GR, a sufficiently

[23] They achieve this by altering the effective gravitational constant.

[24] It's a spatially homogeneous but anisotropic solution falling into the Bianchi Type II category.

[25] Such models have a decreasing angular speed with time.

[26] The associated free-fall time would exceed the age of the universe, leaving no detectable infall or peculiar velocities.

smooth inhomogeneity can escape local dynamical tests, while still biasing the distance ladder.

4 Measuring H_0 from first principles

In Section 3.3 it was shown that the Hubble tension can be traced back into a tension of the calibrator of the local distance ladder, i.e. the absolute magnitude M, and the anchor of the inverse distance ladder, i.e. the comoving sound horizon scale r_d. Furthermore, the direct approach towards H_0 can be considered (quite) model-independent, though it relies on calibration (see Sec. 3.2.1), while the route using the sound horizon does not require calibration, but is generally model-dependent (see Sec. 3.2.2). This motivates the search for a method to determine H_0 that:

- is independent from the calibration steps via the local distance ladder, and the SH0ES calibrated M_B,
- does not rely on the CMB inferred value of the sound horizon,
- and does not assume a specific cosmological model.

The original idea proposed by Renzi and Silvestri [2023] utilizes the distance duality relation (DDR) (see Sec. 2.5), which connects independent distance measurements, to obtain a calibration-free and model-independent estimate of H_0. Three different cosmological probes are used:

- the transverse and line-of-sight BAO scales $D_M(z)/r_d$ and $D_H(z)/r_d = c/(H(z)\,r_d)$ (unanchored),
- independent measurements of $H(z)$ from cosmic chronometers,
- uncalibrated, standardized peak apparent magnitudes of SNe Ia $m_B(z)$.

These probes span nearly the same redshift range ($0 < z \lesssim 2$), and thus measure the same volume of the Universe using independent methods. First, the transverse and radial BAO scales, $D_M(z)/r_d$ and $H(z)\,r_d$, can be combined to isolate the product $H(z)\,D_M(z)$, which is independent of the sound horizon r_d,

$$\frac{D_M(z)}{r_d} = \frac{c}{H(z)\,r_d} \quad \Rightarrow c = D_M(z)\,H(z). \tag{4.1}$$

This combination uses the Alcock-Paczyński (AP) principle, which assumes statistical isotropy of the observed structures. In practice, the transverse and radial BAO scales exhibit small residual differences, due to measurement uncertainties and systematics, which lead to mild modulations in the reconstructed absolute magnitudes across the redshift range. Combining the two scales reduces the constraining power of the BAO data, but it brings the advantage that no anchoring with the sound horizon is required. Secondly, because the BAO and CC data are only given at discrete, non-overlapping redshifts, one first needs to interpolate the CC measurements to the BAO redshifts. To do so a non-parametric Gaussian process (GP) reconstruction of $H(z)$ based on the CC dataset is used. The GP returns, at each BAO redshift z_{BAO}, a posterior PDF for $H(z_{\mathrm{BAO}})$, from which 10^4 Monte-Carlo realizations are drawn at each BAO redshift. The BAO observables D_M/r_d and D_H/r_d are also treated probabilistically, for each z_{BAO} a Gaussian PDF, centered on the published mean with its quoted 1σ uncertainty, is assumed and 10^4 realizations are drawn from that. Then the dependence on $H(z)$ in the BAO data can be cancelled using the Cosmic Chronometers.[1] So that one gets a direct distance measure $[D_M(z)]_{\mathrm{BAO+CC}} = [D_A(z)\,(1+z)]_{\mathrm{BAO+CC}}$ from the combination of BAO and CC data. Or to be more specific at each BAO redshift one gets a Monte-Carlo ensemble of 10^4 distance samples.

As a third step, the apparent magnitudes of SN are integrated into the analysis. First, they need to be shifted to the right frame, since they are measured from Earth they need to be corrected for peculiar motions. The apparent magnitude measured from Earth $\hat{m}_B$ is given by

$$\hat{m}_B(z_{\mathrm{hel}}, z_{HD}) = 5\log_{10}\left(\frac{1+z_{\mathrm{hel}}}{1+z_{\mathrm{HD}}}\,D_L(z_{\mathrm{HD}}\right) + M + 25\,. \tag{4.2}$$

To work with the apparent magnitude in the Hubble diagram frame, i.e. the apparent magnitude corrected for the effect of peculiar motions, the transformation

$$m_B(z_{\mathrm{HD}}) = \hat{m}_B(z_{\mathrm{hel}}, z_{HD}) - 5\log_{10}\left(\frac{1+z_{\mathrm{hel}}}{1+z_{\mathrm{HD}}}\right) \tag{4.3}$$

is used. As a second step, the apparent magnitudes $m_B(z)$ of the SN data are also reconstructed at the BAO redshifts using GP, where at each z_{BAO} 10^4 realizations of $m_B(z)$ are drawn. The three datasets then can be combined for a measure of absolute magnitude at each of the BAO redshifts,

[1] Since CC directly probe the averaged expansion rate, combining them with BAO data, which assume an underlying FLRW metric, implicitly assumes that both datasets trace the same background cosmology. This could be a potential issue in the presence of cosmic backreaction.

$$M_B^{(i)}(z_{\rm BAO}) = -5\,\log_{10}\Big[(1+z_{\rm BAO})^2\left[D_A^{(i)}(z_{\rm BAO})\right]^{\rm BAO+CC}\Big] + \\ + \left[m_B^{(i)}(z_{\rm BAO})\right]^{\rm SN} - 25\,, \tag{4.4}$$

where the DDR has been used to exchange luminosity distance in Equation (2.24) for the distance estimate from BAO and CC data. The result $\left\{M_B^{(i)}\right\}_{i=1}^{10^4}$ is a 10^4-sized Monte-Carlo ensemble of absolute magnitudes at each BAO redshift. This ensemble fully captures the propagated uncertainties from CC, BAO, and SNe Ia data. Note that the ensembles at different redshifts remain statistically correlated with each other, as they are all derived from the same underlying GP reconstructions.

From M_B to H_0

The connecting piece between the absolute magnitude and the Hubble constant is the distance-redshift intercept parameter a_B. This quantity is inferred from a sample of low-z SN in the Hubble flow, following Riess et al. [2016] and Riess et al. [2022] this is taken to be $0.023 < z < 0.15$. This redshift range allows for a smooth FLRW cosmographic expansion up to third order redshift (see Eq. (2.42)), without worrying about curvature effects or higher order terms. Then the observed Hubble diagram is a straight line whose vertical intercept is

$$a_B = \log_{10}\Big[cz\,f(z;q_0,j_0)\Big] - 0.2\,m_B, \tag{4.5}$$

$$f(z;q_0,j_0) \equiv 1 + \tfrac{1}{2}(1-q_0)z - \tfrac{1}{6}(1-q_0-3q_0^2+j_0)z^2. \tag{4.6}$$

The intercept a_B is then used to convert estimates of M_B into estimates of H_0, since it defines their relation in logarithmic terms,

$$M_B = 5\,(\log_{10} H_0 - a_B - 5). \tag{4.7}$$

This relation also holds at higher redshifts than the ones where the local quantity a_B is inferred. Note that the parameter a_B does not bear any physical meaning, it is simply a convenient quantity linking the SN Ia absolute magnitude to H_0 through Equation (4.7). The cosmologically relevant information resides in q_0 and j_0. The dependence on a_B cannot be eliminated if one wants to infer H_0, since only the absolute magnitude is directly measured from Equation (4.4). There are (at least) two slightly conceptually different ways to approach the connection between H_0 and M_B.

(A) Fixed intercept method. One can adopt a single, externally determined value of the intercept parameter a_B measured from a low-redshift Hubble flow SN subsample. Provided (i) the calibrator SNe (used to determine M_B) and (ii) the Hubble flow SNe (used to measure a_B) share no common sources of uncertainty, one can combine a fixed a_B with a measured M_B through Equation (4.7), as done in Riess et al. [2016]. This approach treats M_B and a_B as statistically independent.

(B) Joint-likelihood method. To account for non-trivial covariance between the apparent magnitudes of low and high redshift SN, that arise through shared standardization practices and systematics, a joint likelihood framework is used to fit the quantities simultaneously [Riess et al., 2022]. The joint multivariate Gaussian likelihood is constructed from Equations (4.5) and (4.7),

$$\log \mathcal{L}_{\text{tot}} \;=\; \log \mathcal{L}_{a_B}(q_0, j_0) \;+\; \log \mathcal{L}_{M_B}(H_0, q_0, j_0). \tag{4.8}$$

Finally, the parameters $\{H_0, q_0, j_0\}$ are sampled with an MCMC using Cobaya.

In summary, the joint-likelihod approach propagates the full covariance between M_B and a_B, and thereby ensures that any statistical or systematic link across the whole redshift range is correctly captured in the final estimate of H_0 and its uncertainty. This typically leads to slightly larger but more realistic error bars.

5 Data sets

5.1 BAO

In the analysis six BAO data sets are used, obtained from SDSS DR14, SDSS DR16, DESI DR1, DESI DR2, and two hybrid combinations since the additional BAO points are very constraining and can be combined, if done carefully. These datasets provide radial and angular BAO distance measurements at various redshifts, expressed as D_H/r_d and D_M/r_d, where $D_H = c/H(z)$, $D_M = (1+z)D_A(z)$, and r_d is the comoving sound horizon at the drag epoch. The datasets cover a redshift range from $0.38 \lesssim z \lesssim 2.5$. The hybrid DESI DR1+SDSS dataset follows the prescription from DESI Collaboration [2025b, App. A], combining BAO-only measurements from SDSS at low redshift with DESI LRG and ELG results at intermediate redshifts, and Ly-α data from both SDSS and DESI. This approach maximizes effective volume while preserving radial and transverse distance measurements at each redshift. For the DESI DR2+SDSS hybrid dataset, a single SDSS BAO-only point at $z = 0.38$ has been added, because DESI DR2 does not provide separate D_H and D_M measurements at that redshift. In the following Tables the used BAO measurements are listed.

Tracer	z	D_M/r_d	D_H/r_d
BOSS galaxy-galaxy	0.38	10.27 ± 0.15	24.89 ± 0.58
eBOSS galaxy-galaxy	0.51	13.38 ± 0.18	22.43 ± 0.48
BOSS CMASS, eBOSS LRG	0.70	17.65 ± 0.30	19.78 ± 0.46
eBOSS ELG	0.85	19.50 ± 1.00	19.60 ± 2.10
eBOSS QSO	1.48	30.21 ± 0.79	13.23 ± 0.47
eBOSS Ly-α–Ly-α	2.34	37.41 ± 1.86	8.86 ± 0.29
eBOSS Ly-α–QSO	2.35	36.30 ± 1.80	8.20 ± 0.36

Table 5.1: *BAO and RSD measurements from SDSS DR14 from various papers focussing on different tracers: Alam et al. [2017], Bautista et al. [2021], Neveux et al. [2021], Blomqvist et al. [2019], de Sainte Agathe et al. [2019].*

Tracer	z	D_M/r_d	D_H/r_d
Same as DR14 up to $z = 1.48$			
Ly-α–Ly-α	2.33	37.60 ± 1.90	8.93 ± 0.28
Ly-α–quasar	2.330	37.30 ± 1.70	9.08 ± 0.34

Table 5.2: *BAO and RSD measurements from SDSS DR16 Alam et al. [2021].*

Tracer	z	D_M/r_d	D_H/r_d
DESI LRG1	0.510	13.62 ± 0.25	20.98 ± 0.61
DESI LRG2	0.706	16.85 ± 0.32	20.08 ± 0.60
DESI LRG3+ELG1	0.930	21.71 ± 0.28	17.88 ± 0.35
DESI ELG2	1.317	27.79 ± 0.69	13.82 ± 0.42
DESI Ly-α–QSO	2.330	39.71 ± 0.94	8.52 ± 0.17

Table 5.3: *DESI DR1 BAO-only measurements from DESI Collaboration [2025c].*

Tracer	z	D_M/r_d	D_H/r_d
SDSS BAO-only	0.38	10.23 ± 0.17	25.00 ± 0.76
SDSS BAO-only	0.51	13.36 ± 0.21	22.33 ± 0.58
DESI LRG	0.71	16.85 ± 0.32	20.08 ± 0.60
DESI ELG	0.93	21.71 ± 0.28	17.88 ± 0.35
DESI ELG	1.32	27.79 ± 0.69	13.82 ± 0.42
SDSS QSO	1.48	30.69 ± 0.80	13.26 ± 0.55
Ly-α combined	2.33	38.80 ± 0.75	8.72 ± 0.14

Table 5.4: *Combined SDSS + DESI DR1 dataset following DESI prescription in DESI Collaboration [2025c].*

Tracer	z	D_M/r_d	D_H/r_d
DESI LRG1	0.510	13.588 ± 0.167	21.863 ± 0.425
DESI LRG2	0.706	17.351 ± 0.177	19.455 ± 0.330
DESI LRG3+ELG1	0.934	21.576 ± 0.152	17.641 ± 0.193
DESI ELG2	1.321	27.601 ± 0.318	14.176 ± 0.221
DESI QS0	1.484	30.512 ± 0.760	12.817 ± 0.516
DESI Ly-α–QSO	2.330	38.988 ± 0.531	8.632 ± 0.101

Table 5.5: *DESI DR2 BAO-only measurements from DESI Collaboration [2025d].*

Tracer	z	D_M/r_d	D_H/r_d
SDSS BAO-only	0.38	10.23 ± 0.17	25.00 ± 0.76
DESI LRG1	0.510	13.588 ± 0.167	21.863 ± 0.425
DESI LRG2	0.706	17.351 ± 0.177	19.455 ± 0.330
DESI LRG3+ELG1	0.934	21.576 ± 0.152	17.641 ± 0.193
DESI ELG2	1.321	27.601 ± 0.318	14.176 ± 0.221
DESI QS0	1.484	30.512 ± 0.760	12.817 ± 0.516
DESI Ly-α–QSO	2.330	38.988 ± 0.531	8.632 ± 0.101

Table 5.6: *DESI DR2 + SDSS at low redshift ($z = 0.38$) hybrid dataset from DESI Collaboration [2025d] and Alam et al. [2021].*

5.2 Cosmic Chronometer

Cosmic Chronometer, introduced in Section 3.2.3.5, directly probe $H(z)$ without relying on an explicit cosmological model. In this work 33 CC measurements of $H(z)$ are used, aswell as their 1σ uncertainties reported by the original authors, in a redshift range from $0 \lesssim z \lesssim 2$ (see Tab. 5.7). To include correlations, because of shared systematics and data-processing choices, the full covariance matrix has to be constructed. Following the methodology of Moresco et al. [2020b] and the public implementation available at `https://gitlab.com/mmoresco/CCcovariance`:

$$\mathrm{Cov}_{ij}^{\mathrm{tot}} = \mathrm{Cov}_{ij}^{\mathrm{stat}} + \mathrm{Cov}_{ij}^{\mathrm{syst}},$$

where the systematic part is further decomposed into

$$\mathrm{Cov}_{ij}^{\mathrm{syst}} = \mathrm{Cov}_{ij}^{\mathrm{met}} + \mathrm{Cov}_{ij}^{\mathrm{young}} + \mathrm{Cov}_{ij}^{\mathrm{model}}.$$

Here, $\mathrm{Cov}_{ij}^{\mathrm{met}}$ accounts for uncertainties in stellar metallicity estimation, and $\mathrm{Cov}_{ij}^{\mathrm{young}}$ models the contamination from residual young stellar populations [Moresco et al., 2020b]. Both of these are treated as purely diagonal, as they are uncorrelated between redshift bins. The modeling term $\mathrm{Cov}_{ij}^{\mathrm{model}}$ captures the systematic uncertainty due to the choice of stellar population synthesis (SPS) models, initial mass function (IMF), stellar libraries, and star formation history (SFH). In particular, the IMF term reflects differences between common IMF choices rather than only one IMF, and its average impact on $H(z)$ is small compared to the SPS contribution [Moresco, 2023]. It is assumed to be correlated across all redshifts and is given by [Moresco et al., 2022],

$$\mathrm{Cov}_{ij}^{\mathrm{model}} = \mathrm{Cov}_{ij}^{\mathrm{SPS}} + \mathrm{Cov}_{ij}^{\mathrm{IMF}} + \mathrm{Cov}_{ij}^{\mathrm{st.lib.}} + \mathrm{Cov}_{ij}^{\mathrm{SFH}},$$

where each of the matrices is non-diagonal.

z	$H(z)$ [km s^{-1} Mpc^{-1}]	σ_H [km s^{-1} Mpc^{-1}]	Reference
0.07	69.0	19.6	Zhang et al. [2014]
0.09	69.0	12.0	Jimenez et al. [2003]
0.12	68.6	26.2	Zhang et al. [2014]
0.17	83.0	8.0	Simon et al. [2005]
0.1791	74.91	3.81	Moresco et al. [2012]
0.1993	74.96	4.90	Moresco et al. [2012]
0.20	72.9	29.6	Zhang et al. [2014]
0.27	77.0	14.0	Simon et al. [2005]
0.28	88.8	36.6	Zhang et al. [2014]
0.3519	82.78	13.95	Moresco et al. [2012]
0.3802	83.0	13.54	Moresco et al. [2016]
0.40	95.0	17.0	Simon et al. [2005]
0.4004	76.97	10.18	Moresco et al. [2016]
0.4247	87.08	11.24	Moresco et al. [2016]
0.4497	92.78	12.9	Moresco et al. [2016]
0.4783	80.91	9.04	Moresco et al. [2016]
0.47	89.0	49.6	Ratsimbazafy et al. [2017]
0.48	97.0	62.0	Stern et al. [2010]
0.5929	103.8	12.50	Moresco et al. [2012]
0.6797	91.6	7.96	Moresco et al. [2012]
0.75	105.0	10.76	Jimenez et al. [2023]
0.7812	104.5	12.20	Moresco et al. [2012]
0.8754	125.1	16.70	Moresco et al. [2012]
0.88	90.0	40.0	Stern et al. [2010]
0.90	117.0	23.0	Simon et al. [2005]
1.037	153.7	19.67	Moresco et al. [2012]
1.26	135.0	65.0	Tomasetti et al. [2023]
1.30	168.0	17.0	Simon et al. [2005]
1.363	160.0	33.58	Moresco [2015]
1.43	177.0	18.00	Simon et al. [2005]
1.53	140.0	14.0	Simon et al. [2005]
1.75	202.0	40.0	Simon et al. [2005]
1.965	186.5	50.43	Moresco [2015]

Table 5.7: *Cosmic chronometer $H(z)$ measurements and their 1σ uncertainties from various sources used in this work.*

5.3 SNe Ia

Two independent Type Ia supernovae datasets are used in this work, that differ in methodology and redshift cover.

Pantheon+: The Pantheon+ catalogue [Scolnic et al., 2022] consists of 1701 light curves for 1550 spectroscopically confirmed SNe a from 18 different surveys. They cover a redshift range of $0.001 \leq z \leq 2.26$. All photometry is cross-calibrated and refit with SALT2 (via SNANA), using rest-frame $300 - 700\,\mathrm{nm}$ coverage and -15 to $+45$ day epochs around the SN peak. The SN standardization procedure assumed the Tripp (see Eq. (3.2)) with simulation based bias corrections and a host-mass term [Scolnic et al., 2022]. Compared to Pantheon, Pantheon+ has a larger sample size, especially at $z < 0.01$, and an improved treatment of uncertainties in redshift, peculiar velocity, intrinsic scatter model of SNe, and photometric calibration. The full covariance matrix is used, which contains calibration, light-curve model, selection/bias, peculiar velocity, and host-mass systematics.

DES-SN 5Y: The DES-SN 5Y dataset [DES Collaboration, 2024] comes from observing 10 fields, covering approximately $3\,\mathrm{deg}^2$, with approximately weekly cadence during 2013-2018. Compared to Pantheon+ the DES dataset is single-instrument. The surveys contain different amount of SNe in different redshift ranges (see Fig. 5.1 and Fig. 5.2). The main difference to Pantheon+ is that DES uses photometric classification of SNe with SuperNNova and SCONE, assigning a Type Ia probability. They estimate the contamination with core-collapse SN to be $\sim 6.5\%$ and likely contaminated SN are weigthed down by increased distance errors [DES Collaboration, 2024]. After uniform quality cuts and SALT3 light-curve fitting, the DES sample contains 1635 SNe from $0.10 < z < 1.13$, as well as an external low-z anchor of 194 Sne (from CfA3, CfA4, CSP(DR3), Foundation SN survey) in the range of $0.025 < z < 0.10$, which is not measured by DES directly, for a total of 1829 SNe. Distances are derived with a Tripp standardization including a host-property step and simulation-based bias corrections within the BEAMS with Bias Corrections framework. [DES Collaboration, 2024] The full statistical and systematic covariance matrix covers calibration, intrinsic-scatter modelling and redshift corrections.

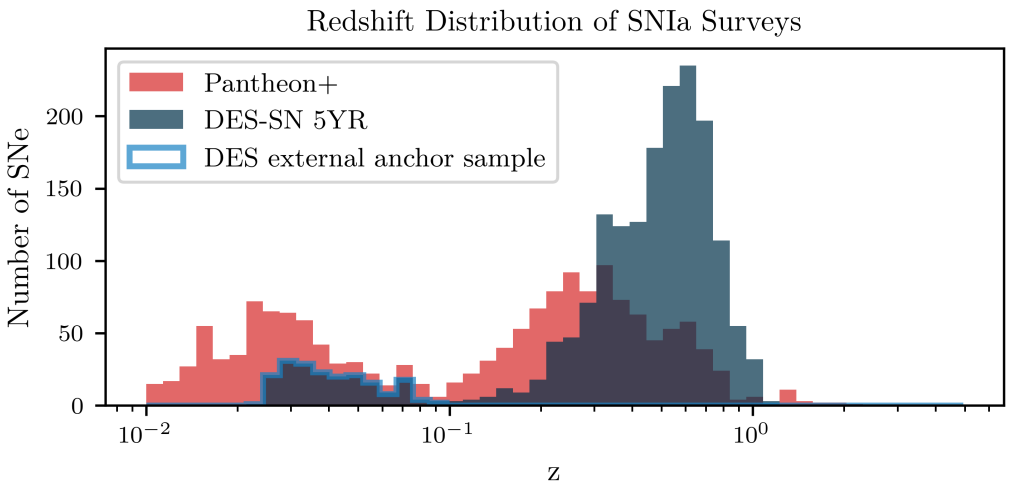

Figure 5.1: *Comparison between the Pantheon+ and DES-SN 5Y redshift distributions.*

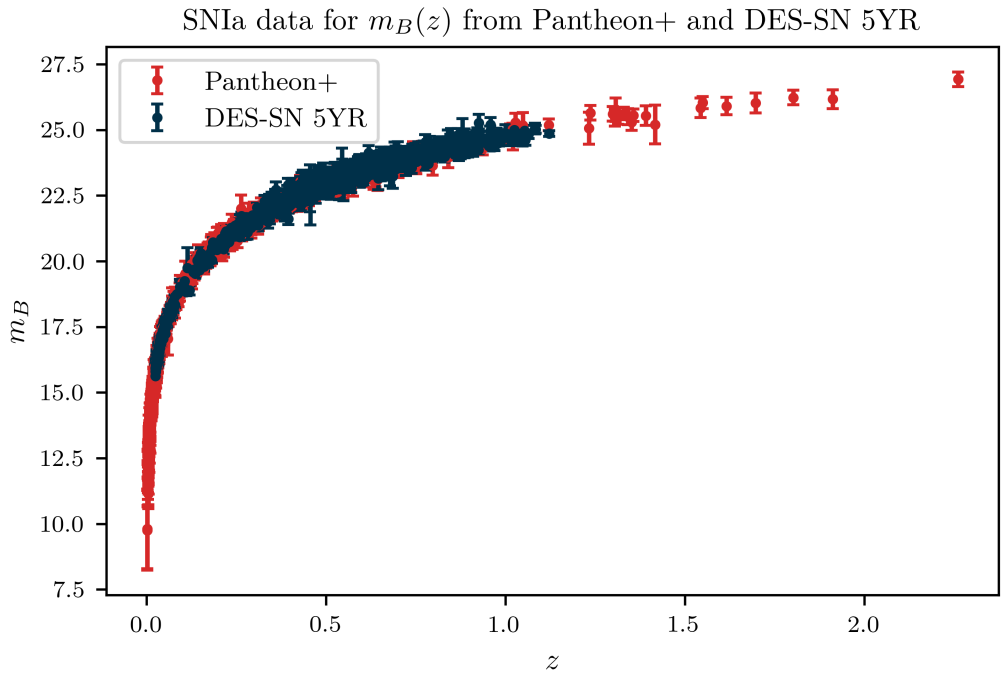

Figure 5.2: *SNIa data for the apparent corrected magnitude from Pantheon+ and DES-SN 5YR. To avoid overcrowding in the plot, SNe from the DES-SN 5YR dataset with an error larger than 1 were excluded, resulting in the removal of 75 data points for the plot.*

6 Gaussian Processes

6.1 Fundamentals

A Gaussian Process (GP) is a Bayesian framework for reconstructing functions in a non-parametric way. Instead of specifying a fixed functional form with a finite number of parameters, a GP defines a probability distribution over functions, such that any finite set of function values follows a joint Gaussian distribution [Rasmussen and Williams, 2005].

Formally, a GP can be written as

$$f(\mathbf{x}) \sim \mathcal{GP}\left(m(\mathbf{x}),\, k(\mathbf{x}, \mathbf{x}')\right), \tag{6.1}$$

where $\mathbf{x} \in \mathbb{R}^D$ is the input or training vector of dimension D, $m(\mathbf{x}) = \mathbb{E}[f(\mathbf{x})]$ is the mean function, and $k(\mathbf{x}, \mathbf{x}') = \mathrm{cov}\left(f(\mathbf{x}), f(\mathbf{x}')\right)$ is the covariance function or kernel, which includes information about smoothness, amplitude, and correlation length of the function values [Rasmussen and Williams, 2005]. Often the mean function is set to zero, unless there is specific prior information to motivate a different choice, since the kernel largely determines the behavior of the model.

In this work, the GP framework is used to interpolate and smooth cosmological observables measured at discrete and not matching redshifts. Specifically,

1. the apparent magnitude $m_B(z)$ of SN Ia,
2. and $H(z)$ from CC data,

need to be reconstructed at the BAO redshifts, in order to combine them consistently through the distance duality relation in Equation (4.4). Gaussian Processes provide a principled way to reconstruct these functions, together with their uncertainties, directly from the data.

6.1.1 Prior and Likelihood

Let the observed dataset be

$$\mathcal{D} = \{(\mathbf{x}_i, y_i)\}_{i=1}^{N}, \tag{6.2}$$

where y_i are noisy measurements of the underlying function $f(\mathbf{x}_i)$ that should be reconstructed. Each observation is modelled as

$$y_i = f(\mathbf{x}_i) + \boldsymbol{\varepsilon}, \tag{6.3}$$

where $\boldsymbol{\varepsilon} \sim \mathcal{N}(\mathbf{0}, \Sigma_{\text{obs}})$ is the observational noise, with $\Sigma_{\text{obs}} \in \mathbb{R}^{N\times N}$ the observational covariance matrix of the data. The special case of independent Gaussian noise is $\Sigma_{\text{obs}} = \sigma_n^2 I_N$.

The GP prior states that the vector of underlying function values at the training inputs,

$$\mathbf{f} = [f(\mathbf{x}_1), \ldots, f(\mathbf{x}_N)]^\top, \tag{6.4}$$

is distributed as a multivariate Gaussian,

$$\mathbf{f} \sim \mathcal{N}\left(\mathbf{0},\, K(X, X)\right). \tag{6.5}$$

The kernel specifies how correlated the function values are between two input points $\mathbf{x}_i$ and $\mathbf{x}_j$. [Rasmussen and Williams, 2005]

6.1.2 Posterior and Predictions

For a set of test inputs, $X_* = \{\mathbf{x}_*^{(j)}\}_{j=1}^M$, where M is the number of locations at which we want to make predictions, let the corresponding (unobserved) underlying function values be $\mathbf{f}_* = [f(\mathbf{x}_*^{(1)}), \ldots, f(\mathbf{x}_*^{(M)})]^\top$. In this work, the test inputs X_* correspond to the BAO redshifts, and the vector $\mathbf{f}_*$ contains the reconstructed $m_B(z)$ or $H(z)$ values at those redshifts.

Under the GP prior, the training outputs $\mathbf{y}$ (measured at the training inputs X) and the function values $\mathbf{f}_*$ at the test inputs are jointly Gaussian distributed,

$$\begin{bmatrix} \mathbf{y} \\ \mathbf{f}_* \end{bmatrix} \sim \mathcal{N}\left(\mathbf{0}, \begin{bmatrix} K(X,X) + \Sigma_{\text{obs}} & K(X, X_*) \\ K(X_*, X) & K(X_*, X_*) \end{bmatrix}\right). \tag{6.6}$$

Conditioning this joint distribution on the known training data $(X, \mathbf{y})$ and on the specified test inputs X_* gives the GP posterior at the test locations

$$\mathbf{f}_* \,|\, X, \mathbf{y}, X_* \sim \mathcal{N}\left(\bar{\mathbf{f}}_*,\, \text{cov}(\mathbf{f}_*)\right), \tag{6.7}$$

with predictive mean

$$\bar{\mathbf{f}}_* = \mathbf{m}_* + K(X_*, X)\left[K(X,X) + \Sigma_{\text{obs}}\right]^{-1}(\mathbf{y} - \mathbf{m}), \tag{6.8}$$

and predictive covariance

$$\mathrm{cov}(\mathbf{f}_*) = K(X_*, X_*) - K(X_*, X)\left[K(X, X) + \boldsymbol{\Sigma}_{\mathrm{obs}}\right]^{-1} K(X, X_*). \tag{6.9}$$

The predictive mean $\bar{\mathbf{f}}_*$ gives the reconstructed function values at the test inputs, while the predictive covariance $\mathrm{cov}(\mathbf{f}_*)$ gives the uncertainties and correlations between these predictions.[1] [Rasmussen and Williams, 2005] The quality of these predictions depends on the choice of kernel function and its hyperparameters $\boldsymbol{\tau}$, which determine the structure of the prior covariance $K(X, X)$. Therefore, in the next section the kernels used in this work are introduced, before discussing how the kernel hyperparameters get optimized.

6.1.3 Kernels

The most simple kernel is the squared exponential (SE) kernel, also called the radial basis function (RBF) kernel, defined as

$$k_{\mathrm{SE}}(\mathbf{x}, \mathbf{x}') = \sigma_M^2 \exp\left(-\frac{\|\mathbf{x} - \mathbf{x}'\|^2}{2\ell^2}\right), \tag{6.10}$$

where σ_M^2 is the signal variance and ℓ is the characteristic length scale controlling how quickly correlations decay with distance in input space. The SE kernel encodes the assumption that the underlying function is smooth and infinitely differentiable.

RBF kernels can be extended to offer more flexibility in modelling non-smooth functions, to do this Matérn kernels are used in this work. The general Matérn kernel with smoothness parameter $\nu > 0$ is

$$k_{\text{Matérn}}(\mathbf{x}, \mathbf{x}') = \sigma_M^2 \frac{2^{1-\nu}}{\Gamma(\nu)} \left(\frac{\sqrt{2\nu}\, r}{\ell}\right)^{\nu} K_\nu\left(\frac{\sqrt{2\nu}\, r}{\ell}\right), \tag{6.11}$$

where $r = \|\mathbf{x} - \mathbf{x}'\|$, Γ is the gamma function, and K_ν is the modified Bessel function of the second kind. For half-integer ν the expression simplifies to a product of an exponential and a polynomial. For example, with $\nu = 3/2$:

$$k_{\nu=3/2}(\mathbf{x}, \mathbf{x}') = \sigma_M^2 \left(1 + \frac{\sqrt{3}r}{\ell}\right) \exp\left(-\frac{\sqrt{3}r}{\ell}\right). \tag{6.12}$$

[1] That is the big advantage of GPs, more than giving a best fit they provide the predictive covariance to the predictions.

While the SE kernel is appropriate for very smooth functions, Matérn kernels allow for finite differentiability and can better match the statistical properties of many physical processes. Both, SE and Matérn kernels belong to the class of stationary kernels, which only depend on the distance $\|\mathbf{x} - \mathbf{x}'\|$. The choice of kernel, together with its hyperparameters $\boldsymbol{\tau}$, fully specifies the GP prior covariance $K(X, X)$. [Rasmussen and Williams, 2005] Optimizing these hyperparameters so that $K(X, X)$ best matches the intrinsic correlation structure of the data, given the observational covariance Σ_{obs}, is one of the most challenging steps in GP regression and will be the focus of the next section.

6.2 Kernel Optimization: Objective Functions

6.2.1 Log Marginal Likelihood (LML) Method

The most common approach to determine the hyperparameters $\boldsymbol{\theta}$ of a GP kernel is by maximizing the LML of the observed data under the GP model. The LML is given by

$$\begin{aligned}\log p(\mathbf{y} \mid X, \boldsymbol{\theta}) = &-\frac{1}{2}(\mathbf{y} - \mathbf{m})^\top \Big[K(X, X) + \Sigma_{\text{obs}}\Big]^{-1}(\mathbf{y} - \mathbf{m}) - \\ &- \frac{1}{2}\log\det\Big[K(X, X) + \Sigma_{\text{obs}}\Big] - \frac{N}{2}\log(2\pi)\ ,\end{aligned} \tag{6.13}$$

where N is the number of training points, which is the entire dataset for the LML.

The LML quantifies how plausible the entire observed dataset is under the GP prior with hyperparameters $\boldsymbol{\theta}$. Therefore, it does not evaluate predictions, instead it asks how well the whole observed data fits the GP model. Maximizing Equation (6.13) balances how good the fit is (first term) with model complexity (second term), the latter penalizing overly flexible kernels via the determinant of the total covariance matrix. In practice, the general workflow is:

1. Choose a kernel $k(\mathbf{x}, \mathbf{x}'; \boldsymbol{\theta})$.
2. Compute the LML for the whole dataset for given $\boldsymbol{\theta}$.
3. Determine $\boldsymbol{\theta}$ either by:

- Maximization of the LML (point estimate), or
- Marginalization over $\boldsymbol{\theta}$ using its posterior $p(\boldsymbol{\theta} \mid \mathbf{y}, X) \propto p(\mathbf{y} \mid X, \boldsymbol{\theta})\, p(\boldsymbol{\theta})$, usually via MCMC sampling.

4. If maximization is used, fix $\boldsymbol{\theta}$ to the optimal value and use the kernel in the GP. If marginalization is used, average predictions over the MCMC samples of $\boldsymbol{\theta}$.

The advantage of the LML is that it is fully Bayesian and has relatively low computational cost to implement. Furthermore, it naturally incorporates a trade-off between data fit and model complexity.

However, the method must be applied with care. Since the LML is computed using the entire dataset, the GP is effectively trained and evaluated on the same points. This makes the optimization closer to an interpolation than to a true test of predictive performance. As a result, the hyperparameters may be tuned to fit the specific noise realization in the training set, giving an overly optimistic impression of model performance. If the hyperparameters are fixed to their maximum-LML values, the resulting predictive uncertainties can be underestimated, because alternative hyperparameter combinations that also fit the data well are ignored. The correct procedure is to marginalize over $\boldsymbol{\theta}$ using its posterior distribution, allowing these uncertainties to propagate into the reconstruction. Hwang et al. [2023] emphasize that the choice of prior mean $\mathbf{m}(X)$ can strongly affect the LML surface and the resulting hyperparameters. Poorly chosen mean functions can lead to biased reconstructions and even unphysical features such as oscillations or negative derivatives in quantities that should be monotonic [Hwang et al., 2023]. Favale et al. [2023] report that in LML GP reconstructions of $H(z)$ from cosmic chronometers, the reduced χ^2 per degree of freedom $\tilde{\chi}^2$ can be significantly below 1 for all kernels tested. While this may partly indicate overestimated observational uncertainties, it also illustrates that optimizing the LML does not necessarily guarantee realistic predictive uncertainties.

In summary, the LML method is the conventional choice for GP hyperparameter optimization, but it must be applied with caution, it evaluates the plausibility of the observed data under the GP prior, not the GP's ability to predict unseen data.

6.2.2 Gaussian Process Monte Carlo (GPMC)

The GPMC method by Renzi and Silvestri [2023] optimizes the kernel by directly targeting predictive performance and thereby avoiding the problem

of evaluating the GP on the same points it was trained on. Crucially, in this method the GP regression is already run inside the optimization loop, for each trial set of hyperparameters $\boldsymbol{\theta}$, a GP is trained on the training data, predictions are made for the testing data, and the resulting agreement is scored via a χ^2 likelihood:

$$-2\ln\mathcal{L}(\boldsymbol{\theta}) = \left[\mathbf{Y}^{\text{pred}}(\boldsymbol{\theta}) - \mathbf{Y}^{\text{test}}\right]^{\top}\Sigma^{-1}\left[\mathbf{Y}^{\text{pred}}(\boldsymbol{\theta}) - \mathbf{Y}^{\text{test}}\right], \quad (6.14)$$

where Σ is the known covariance matrix of the test data, $\mathbf{Y}^{\text{pred}}$ are the GP predictions at the test points, and $\mathbf{Y}^{\text{test}}$ are the corresponding observed values.

In practice, the workflow is:

1. Select a training and testing dataset for a given observable.
2. Train a GP with kernel $k(\boldsymbol{\tau})$ on the training set.
3. From the GP posterior, predict the observable at the testing redshifts.
4. Compare these predictions to the testing dataset by evaluating the χ^2 in Eq. (6.14).
5. Adjust $\boldsymbol{\tau}$ to minimize χ^2, so it is a maximum likelihood estimate (MLE). There are two options:
   - Select the single hyperparameter set $\boldsymbol{\tau}$ that minimizes χ^2, ignoring the uncertainty in $\boldsymbol{\tau}$, as originally done by Renzi and Silvestri [2023].
   - **Ensemble averaging:** To capture the uncertainties in the hyperparamters one keeps the top N hyperparameter sets ranked by their χ^2. For each set, one computes the GP prediction for the target function $f(z)$ (e.g. $H(z)$). Then, the predictions are stacked and resampled to form the final PDF for $f(z)$. In this way, one averages over predictions rather than over the hyperparameters themselves, so that the nonlinear mapping from $\boldsymbol{\tau}$ to $f(z)$ is correctly preserved.

In the following, different strategies for constructing the training and testing datasets within the GPMC framework are explored. We first consider the case where the training and testing sets come from different observational samples (external dataset), and then look variants where they are drawn

from the same dataset, using simple train-test splits, K-fold cross-validation, and leave-one-out validation.

6.2.2.1 Testing with External Dataset

Originally, Renzi and Silvestri [2023] used an external dataset from SNe Ia as the testing set for the GP optimization of CC data. Specifically, six measurements of $E(z)$ were employed, which required an extrapolation of $H(z)$ to $z \to 0$ in order to convert between $H(z)$ and $E(z)$. For the GP regression of $m_B(z)$ from the SNe data[2], a binned SNe dataset was used. [3]

The main advantage of using a truly out-of-sample dataset is that it provides a direct test of the GP's predictive performance on unseen data. Another advantage of using an external testing set is that it allows the full dataset to be used for GP training, which is especially important for CC data given the limited number of available measurements (see Table 5.7, 33 points). The main drawback is that, when the goal is to analyse the impact of different dataset combinations on H_0 and to test the consistency between SN and BAO datasets (see Section 5), the inclusion of additional measurements in the optimization can introduce extra assumptions and systematic effects, potentially biasing the very datasets one wants to compare. Moreover, there is no guarantee that the out-of-sample testing data are in any way closer to the true physical relation than the training data. This concern is particularly relevant in our case, where we have multiple SN and BAO datasets but only a single CC dataset for $H(z)$, adding external data to the optimization may compromise the comparison.

6.2.2.2 Self-Contained Testing on the Optimization Dataset

Simple Train-Test Split In the simplest setup, the dataset is randomly divided into two subsets: a training set, used to fit the GP and optimize its hyperparameters, and a test set used to assess predictive performance. To avoid biased evaluation, both sets should cover the full redshift range. The optimal train-test ratio depends on dataset size, large samples can be split more evenly, while small ones require a minimal test fraction to keep the reconstruction stable. For very sparse datasets, cross-validation is generally preferable, as it uses all points for both training and evaluation without permanently discarding data for testing. This consideration is particularly

[2] Renzi and Silvestri [2023] analyzed the Pantheon SN dataset.

[3] However, this is not strictly an external dataset, since the same individual SNe still contribute to the binned points.

relevant for datasets with few points, such as the Cosmic Chronometer sample ($N = 33$), where removing even a small subset substantially reduces the available information. For the CC data a simple train-test split highly depends on the way the split is done and therefore should not be used. Applying a simple split to the SN data still produces stable reconstructions that are almost independent on the way the split is done, but the resulting M_B values, computed via Equation (4.4), exhibit substantially higher correlations between redshifts compared to cross-validation. This is likely because the evaluation is based on a single, fixed partition of the dataset, the training set remains dense across the redshift range, so test points are often located very close in redshift to training points. In such cases, the GP can interpolate with minimal uncertainty, which inflates the apparent correlation structure and yields overly optimistic performance estimates. Cross-validation averages results over multiple partitions, including configurations where the model must predict in less densely covered regions, thus providing a more robust and realistic measure of generalization.

K-Fold Cross-Validation (CV) In K-fold CV, the dataset is first split into K equally sized subsets, or "folds". For each run, one fold is kept aside as the test set while the remaining $K-1$ folds are used as the training set. This process is repeated K times, each time holding out a different fold for testing, so that every point in the dataset is used once for testing and $K-1$ times for training. The log-likelihood from each fold is summed and then divided by the number of folds used, giving the average log-likelihood, that is used as the optimization target. Since the average smooths over fold-to-fold variations, it will generally not match the optimum of any single fold, and it is likewise not guaranteed to reach the global optimum. Instead, the optimizer seeks hyperparameters with good average performance across all splits. Compared to a single train-test split, this approach is more stable and avoids the problem of the dependency on the specific way the split is done. It also produces reconstructions that are less correlated than those from a simple train-test split. In the GPMC framework, an important benefit is that in Eq. (6.14) the covariance matrix $\mathbf{\Sigma}$ always refers to the test points of the current fold, as every data point is eventually part of a test fold, the complete covariance matrix of the dataset is effectively used during the process. This is an advantage over the simple train-test split or the external dataset validation, where only the covariance of the specific test set enters the likelihood.

A slight drawback is the increased computational cost, since K separate GP fits are required, and the need to choose K carefully. A small K can lead to

high variance in the estimates (since each test set is large and the training set is small), while a very large K may result in high computational load and overly optimistic estimates for some datasets. In many cases, values between $K = 5$ and $K = 10$ give a reasonable balance.

It is good practice to keep a final holdout set that is never seen during training or testing. This set is then used to select the kernel, choosing the one that yields the χ^2 per degree of freedom closest to unity on the holdout. This is advisable because, in K-fold CV every data point is used for training in multiple folds, so evaluating the final model only on the folds risks overestimating its predictive power, the holdout set provides an unbiased check.

6.3 Implementation

6.3.1 Choice of Method

After testing various GP optimization strategies, the method adopted for the final reconstructions is the GPMC approach with K-fold CV. This choice is motivated by the fact that GPMC directly targets predictive accuracy on unseen data, rather than solely maximizing the LML, which can overfit the noise in the training sample and underestimate uncertainties. The use of K-fold CV further improves robustness by averaging predictive performance over multiple train-test splits, ensuring that the selected hyperparameters perform consistently well across the dataset and not just for a specific split. A key advantage is that all data points are used for training while each also serves once as a test point, this is particularly important for CC data, and ensures that the full observational covariance matrix of the dataset is taken into account. About $10 - 20\%$ of the data are used as a final holdout set for kernel selection. Once the kernel is chosen, the full dataset is retrained and partioned into K folds. In the choice of K there is a tradeoff, larger K increase the training fraction but vies smaller test sets, whereas a small K is computationally cheaper but makes the result more sensitive to the particular random fold assignment. Compared to train-test split the distribution of hyperparameters is much more narrow for K-fold CV, particularly for the SN data. In practice, $K = 6$ for CC and $K = 7$ for SN reconstructions are chosen, as this provides a reasonable balance between computational cost, stability, and test set size.

6.3.2 Kernel selection

6.3.2.1 CC dataset

To determine the best kernel for the CC dataset, the Matérn kernels with smoothness parameters $\nu \in \{0.5, 1.5, 2.5, 3.5, 4.5\}$ are tested. For each ν, the kernel amplitude σ_M and characteristic length scale ℓ are optimized using the Optuna optimization framework, maximizing the K-fold cross-validated log-likelihood on the training subset. Each kernel is then evaluated on 100 random holdout sets (see an example holdout reconstruction in Fig. 6.1), each containing $N_{\text{holdout}} = 6$ CC data points. For each holdout set, the GP is retrained on the complementary training data using the top-N ensemble from the cross-validation phase, where the top-N ensemble is chosen to be all trials within a tight band $\Delta\mathcal{L}$ of the best CV log-likelihood, and predictions are made for the held-out points. Because of the limited size of the CC data and uneven redshift coverage the GP hyperparameter landscape is relatively flat, variations in ℓ can be traded for changes in σ_M with little change in the CV score. Predictive performance is quantified by the total χ^2_{holdout} with respect to the CC observational uncertainties, and an "effective" value $\chi^2_{\text{eff}} \equiv \chi^2_{\text{holdout}}/N_{\text{holdout}}$ is computed to account for the number of degrees of freedom. The final metric for each kernel is obtained by averaging these quantities over all 100 holdout realizations. Table 6.1 reports the results. The kernel whose mean χ^2_{eff} is closest to unity, is selected for subsequent GP reconstructions of $H(z)$. According to this the Matérn kernel with $\nu = 3.5$ is preferred.

Kernel	Mean χ^2_{holdout}	Mean χ^2_{eff}
Matérn($\nu = 0.5$)	4.086	0.681
Matérn($\nu = 1.5$)	4.536	0.756
Matérn($\nu = 2.5$)	4.577	0.763
Matérn($\nu = 3.5$)	5.892	**0.982**
Matérn($\nu = 4.5$)	6.270	1.045

Table 6.1: *Results of kernel selection criteria for the CC data. GP performance is evaluated on 100 random holdout sets ($N_{\text{holdout}} = 6$ points each) for different Matérn smoothness parameters ν. The column "Mean χ^2_{holdout}" reports the average total χ^2 over all holdout sets, while "Mean χ^2_{eff}" gives the average χ^2 per degree of freedom ($\chi^2_{\text{holdout}}/N_{\text{holdout}}$). The best kernel with the mean χ^2_{eff} value closest to unity is highlighted in bold.*

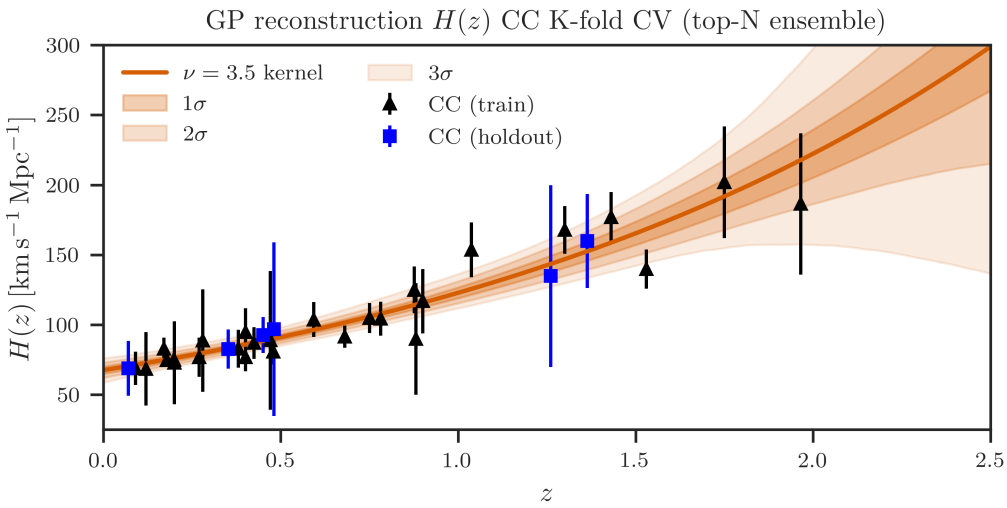

Figure 6.1: *Example GP reconstruction of $H(z)$ from the Cosmic Chronometer dataset using the GPMC method with K-fold cross-validation ($K = 6$), shown for one specific holdout split and a Matérn kernel with $\nu = 3.5$. The solid line is the ensemble averaged mean from the top-N trials, with shaded bands denoting 1σ, 2σ, and 3σ intervals.*

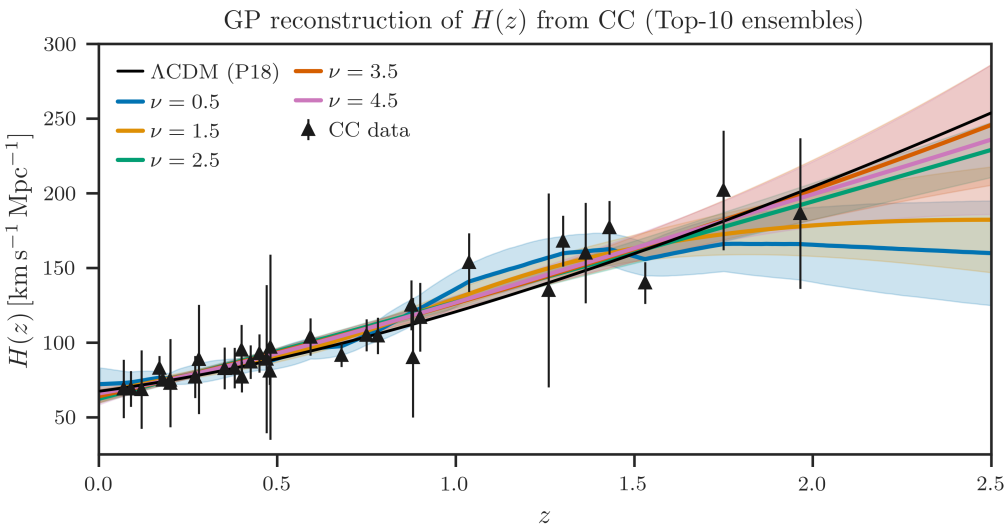

Figure 6.2: *GP reconstructions of $H(z)$ from the CC dataset using Matérn kernels with different smoothness parameters ν. Each curve shows the mean prediction from the top-N hyperparameter (300 trials in total) ensembles selected via cross-validation ($K = 6$), with shaded regions indicating the 1σ dispersion across the ensembles. The ΛCDM model from Planck 2018 is shown for reference.*

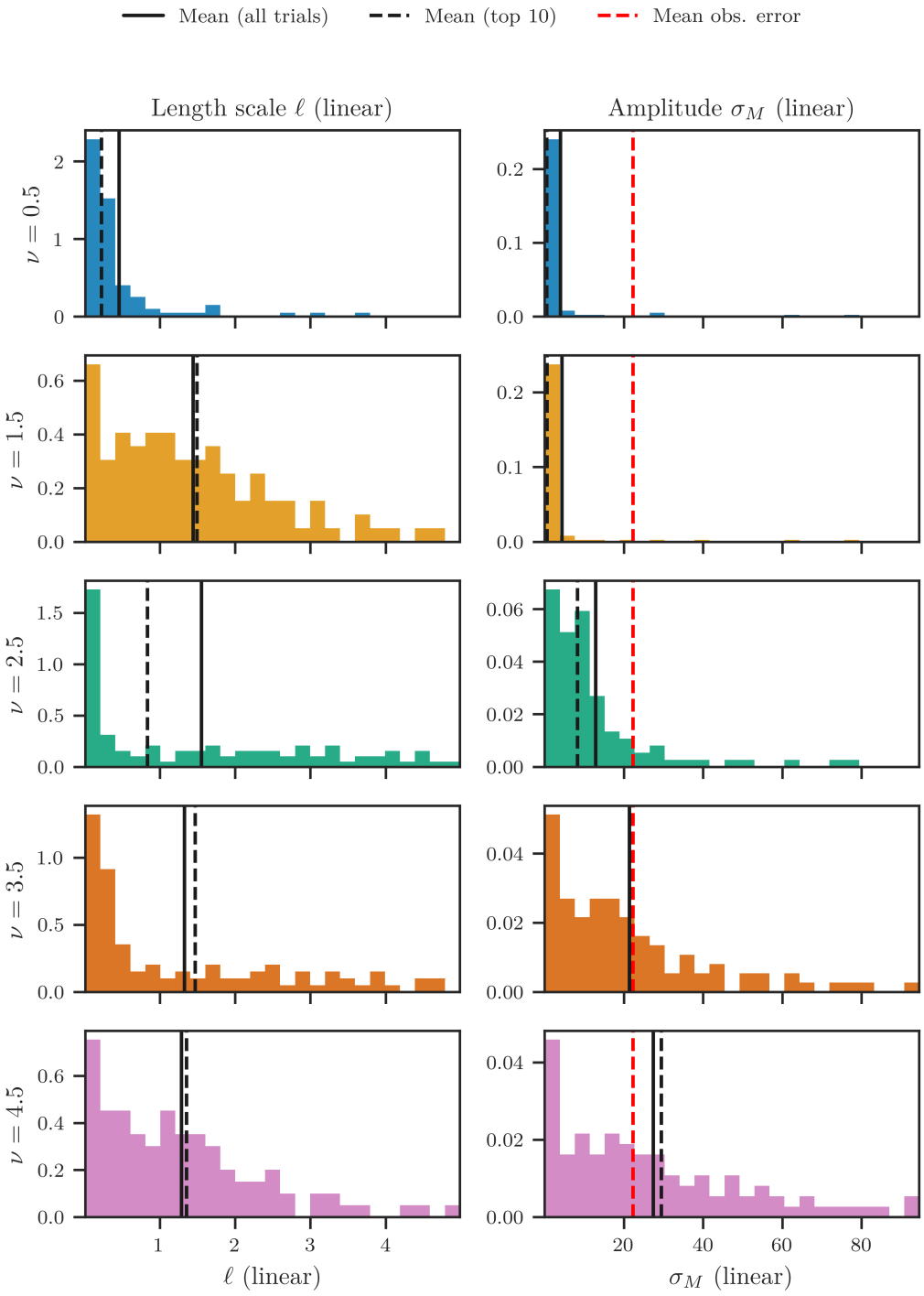

Figure 6.3: *Histograms of the optimized hyperparameters for CC reconstruction, obtained from 100 CV trials ($K = 6$) for each Matérn parameter ν. Solid vertical lines mark the mean over all trials, dashed lines indicate the mean over the top ten trials, and the red dashed line is the mean observational error in $H(z)$.*

The reconstructions for the five Matérn kernels are shown in Figure 6.2. They agree well in the range $0 < z < 1.5$, while in regions without data ($z \lesssim 0.05$ or $z \gtrsim 2$) the extrapolations naturally diverge with widening uncertainties. For $\nu \leq 1.5$, the reconstructions show unstable behaviour: a downward drift at high z and, in the case of $\nu = 0.5$, an artificial bump around $1 < z < 1.5$ that closely tracks individual data points. This can be traced to their hyperparameter posteriors (See Fig. 6.3), which favour short length scales ℓ and small amplitudes σ_M, making the GP overly sensitive to local fluctuations and limiting its extrapolation power.

By contrast, for $\nu \geq 2.5$ the posteriors shift toward larger ℓ and σ_M, yielding smoother reconstructions and more stable high-z behaviour. Among these, the $\nu = 3.5$ kernel is particularly well balanced, its preferred amplitude clusters around $\sigma_M \sim 20\ \mathrm{km\,s^{-1}\,Mpc^{-1}}$, close to the mean observational uncertainty of the CC dataset, which explains its good compromise between local adaptability and long-range stability. Taken together with the holdout metrics in Table 6.1, these considerations motivate the choice of the $\nu = 3.5$ Matérn kernel for the final CC reconstruction.

6.3.2.2 SN datasets

For the SN datasets the kernel gets selected in an analogous procedure to the CC. The results for Pantheon+ using the holdout criterion can be seen in Table 6.2, with the best fitting kernel being the Matérn kernel with $\nu = 3.5$. The advantage of the SN datasets is that they contain much more points, making the reconstructions much more stable and essentially kernel independent in the regions with data coverage (see Fig. 6.4a and 6.4b). As a result, fewer optimization trials with Optuna are required for the SN case. The only notable exception is the very rough kernel with $\nu = 0.5$, which shows an artificial rise at low redshift and a slight downward trend at high redshift in both SN datasets, illustrating its poor extrapolation behaviour. The reason is the same like for the CC, its sample paths are continuous but not differentiable, that's why it is not very smooth and has a short effective correlation. The other kernels $\nu \geq 1.5$ are smoother, with longer ranged correlations, which leads to a more stable behavior at the boundaries. All kernels $\nu \geq 1.5$ are visually nearly indistinguishable in the region with data coverage (see Fig. 6.4a and 6.4b) and show only minor variations in the holdout tests χ^2 (see Tab. 6.2 and 6.3). Across tested kernels the hyperparameter distributions vary only slightly, yielding nearly identical reconstructions. Given these results and for consistency and comparability between the two SN datasets, the Matérn kernel with $\nu = 3.5$ for both Pantheon+ and DES is chosen for

the final reconstructions.

Kernel ν	Mean χ^2_{holdout}	χ^2_{eff}
Matérn($\nu = 0.5$)	197.540	1.162
Matérn($\nu = 1.5$)	179.012	1.053
Matérn($\nu = 2.5$)	177.838	1.040
Matérn($\nu = 3.5$)	171.684	**1.004**
Matérn($\nu = 4.5$)	171.190	1.007

Table 6.2: *For 10 random holdout seeds, 10% of the sample is withheld, the rest is used for K-fold CV (K=7), and the χ^2_{holdout} is computed on the held-out set. Each holdout contains 170 SNe. The table reports the mean of χ^2_{holdout} over the 10 holdouts and the corresponding mean reduced value.*

Kernel ν	Mean χ^2_{holdout}	χ^2_{eff}
Matérn($\nu = 0.5$)	226.005	1.235
Matérn($\nu = 1.5$)	193.065	1.055
Matérn($\nu = 2.5$)	186.660	1.020
Matérn($\nu = 3.5$)	182.085	0.995
Matérn($\nu = 4.5$)	**182.451**	**0.997**

Table 6.3: *Mean χ^2 values on 10 random holdout sets of the DES-SNY5 sample ($N = 1829$). Each holdout contains 183 SNe. While all kernels perform comparably and are well calibrated, $\nu = 4.5$ is marginally preferred, with $\nu = 3.5$ essentially indistinguishable.*

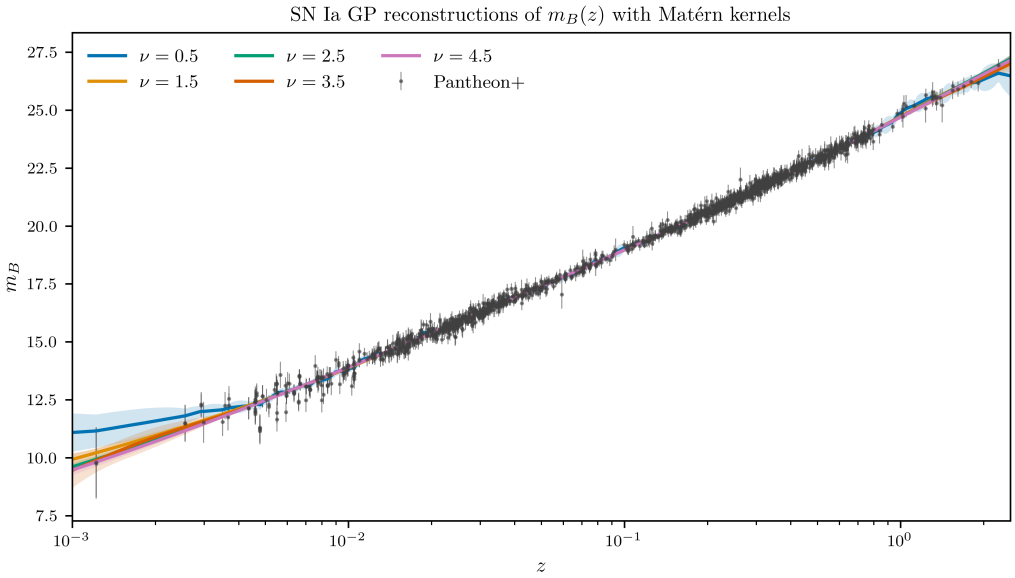

(a) *Pantheon+ GP reconstructions of $m_B(z)$ with varying Matérn smoothness ν.*

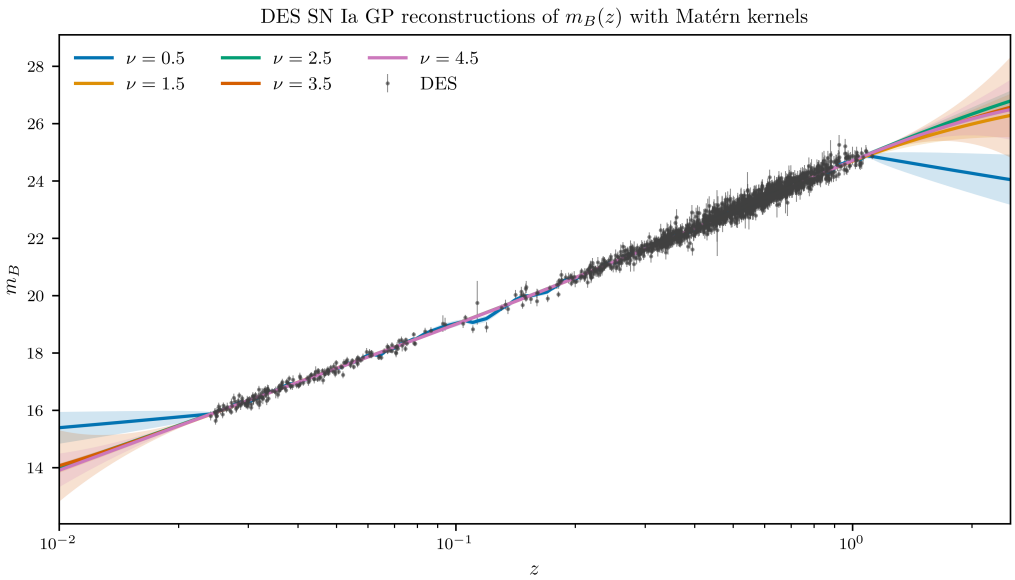

(b) *DES-SN 5Y GP reconstructions of $m_B(z)$ with varying Matérn smoothness ν, points with an error larger than one are omitted in the plot to avoid overcrowding (75 points).*

Figure 6.4: *SN Ia GP reconstructions of $m_B(z)$ with Matérn kernels for Pantheon+ and DES-SN 5Y across several smoothness parameters ($\nu \in \{0.5, 1.5, 2.5, 3.5, 4.5\}$). In both panels, curves show the GP mean with 1σ bands from the top-N trials selected via K=7 cross-validation. For DES, training data extend to $z_{\max} \simeq 1.12$, curves at higher z are extrapolations and carry larger uncertainties.*

6.4 Changes in Methodology

Several key methodological changes have been made in this work compared to Renzi and Silvestri [2023]:

- *Internal validation only:* No external dataset is used for test points, training and validation is performed within the same dataset to focus on testing the consistency between the datasets used and to minimize bias and systematics from including external data.
- *K-fold CV with full training covariance:* K-fold cross-validation enables the use of the full observational covariance of the training data. In Renzi and Silvestri [2023] only the test-point covariance is used. This choice yields slightly larger error bars here, but more realistic and robust ones.
- *Hyperparameter ensembling:* Instead of committing to a single maximum-likelihood hyperparameter set, predictions are averaged over the top trials within a fixed $\Delta\mathcal{L}$ band, capturing hyperparameter uncertainty and reducing the sensitivity to flat regions of the hyperparameter space.
- *Kernel selection via repeated holdouts:* A new kernel selection step adds a χ^2 computed on random holdout sets, looping over many holdout realizations reduces sensitivity to any single split, and kernels are ranked by the mean (reduced) holdout χ^2.
- *Joint-likelihood method:* Rather than fixing a_B, a joint likelihood analysis is performed to account for correlations between low- and high-z SNe (shared standardization and systematics) and to infer q_0 and j_0 alongside H_0.
- *Emphasis on the data-driven quantity:* The analysis here highlights the absolute magnitude M_B as the primary data driven outcome, with H_0 secondarily derived via $\log_{10} H_0 = a_B + 0.2\, M_B + 5$.
- *Optimization details:* The optimization algorithms have been changed to more effectively sample the hyperparameter space.
- *New data:* Two new CC measurements at sparsely sampled redshifts are incorporated together with updated CC systematics and the full covariance matrix; two newer SN catalogues (Pantheon+ and DES-SN 5YR) with substantially more SNe are used; and five additional BAO datasets are included (SDSS DR16, DESI DR1, DESI DR1+SDSS, DESI DR2, DESI DR2+SDSS($z = 0.38$)).

7 Results and Discussion

All results in this chapter follow from the configuration detailed in Section 6.3. For clarity, the discussion in this chapter is structured to trace the analysis workflow.

7.1 Results of this Work

Figure 7.1 shows the final GP reconstruction of $H(z)$ from cosmic chronometers. The reconstruction is well within 1σ of ΛCDM. The mean prediction lies slightly above the ΛCDM curve in the range $0.5 \lesssim z < 2.5$, which coincides with the region where CC data is sparse. The GP extrapolation of $z \to 0$ yields $H_0 = 67.6 \pm 7.7\ \mathrm{km\,s^{-1}\,Mpc^{-1}}$, in good agreement with other non-parametric CC reconstructions of $H(z)$ (e.g., Renzi and Silvestri [2023], Favale et al. [2023]). The residuals in the bottom panel of Fig. 7.1 exhibit no systematic offset and are broadly consistent with zero, confirming agreement between the GP reconstruction and the CC dataset.

In Figure 7.2 the reconstructed angular diameter distance, from the combination of BAO and CC data, at the BAO redshifts is shown. The BAO datasets are broadly consistent with slight deviations around $z \approx 0.5$ and $z \approx 0.7$ between SDSS DR16 and DESI DR1. These differences have been discussed here DESI Collaboration [2025c] and removed with the release of DESI DR2. The known 2σ discrepancy, e.g. see Ye and Lin [2025], between DESI BAO and CMB data under ΛCDM is not visible here, because of the larger uncertainty in the CC measurements compared to the CMB. The mild upward trend of the CC $H(z)$ in Figure 7.1 compared to the ΛCDM expansion rate, directly translates into the BAO reconstructions to be slightly below the curve in Figure 7.2. The effect is small and not statistically significant with current errors.

Figure 7.3 displays the final GP reconstructions of $m_B(z)$ for Pantheon+ and DES-SN 5YR datasets. In both cases the residual panels show a symmetric scatter about zero with no redshift trends visible, indicating a good agreement between the GP fit and the SN data. Compared to the CC reconstruction, the SN GP uncertainty bands are much tighter, due to their much greater data size. Between $1.5 < z < 2.5$ the DES uncertainty

bounds are wider than the ones of Pantheon+, since DES has no data above $z > 1.2$. Nevertheless, due to the large number of SN in DES the extrapolation remains relatively tight. In Figure 7.4 the two reconstructions are compared against each other. The residuals in Figure 7.4a show a catalogue offset, for $z \lesssim 1.2$ the DES points lie systematically below Pantheon+ by ~ 0.04 mag. This is also clearly visible in Figure 7.4b, where the residual $\Delta m_B(z) \equiv m_B^{\mathrm{P+}}(z) - m_B^{\mathrm{DES}}(z)$ is negative over the redshift range in which DES has data, so that SN from Pantheon+ are slightly brighter (numerically smaller magnitudes). A localized feature at $0 < z \lesssim 0.1$ coincides with the DES anchor subset, in this redshift range DES relies on a few external samples. For foundation low-z SNe common to both Pantheon+ and DES, Efstathiou [2025] finds a systematic offset of 0.04-0.05 mag, which matches the bump in Fig. 7.4b for $0 < z < 0.1$. Interestingly, he notes that such a photometric offset could mimic the effect of dynamical dark energy. Note, that the anchor induced bump does not directly affect the reconstructions at the BAO points (see residuals in Figure 7.4a), since the lowest BAO point is at $z \sim 0.4$. Near $z \simeq 0.1$ the DES anchor subset transitions to the main DES survey sample. For SNe in common to both the Pantheon+ and the main DES sample Efstathiou [2025] finds a smaller mean offset of ~ 0.01 mag, which can be explained by the different light-curve fitters (SALT2 vs. SALT3) and varied bias corrections. In Figure 7.4b one can see that the residual between Pantheon+ and DES in the region $0.1 \lesssim z \lesssim 1.2$ is slightly higher (few $\times 10^{-2}$ mag). The key reasons are: (i) the catalogues do not contain the same set of SNe and the GPs are trained on the full catalogues, (ii) there are processing (fitter and bias corrections) and methodological (photometric versus spectral confirmation of SNe Ia) differences between the two catalogues, (iii) here GP means are compared not point estimates, (iv) the GP smoothly bridges the anchor to the main sample transition, (v) most of the incommon SN cluster between $0.2 < z < 0.4$, in that range the residual is closer to zero, the SN at higher z are not shared. It is important to note that, especially at higher redshift, the DES-SN 5YR catalogue does not rely on spectroscopic confirmation of SN. This opens the possibility of contamination from core collapse SN, which could bias the sample. The offset in magnitudes can also be seen in the residuals at the BAO points in Figure 7.4a. At $z \gtrsim 1.5$ the residual in Figure 7.4b turns toward zero and can flip sign, however this is most likely an artifact of the GP extrapolation in that region and not statistically significant.

The catalog differences in the reconstructed m_B propagate almost one-to-one into the inferred absolute magnitudes at the BAO redshifts, see Equation (4.4) where the $D_A(z)$ term from BAO+CC is identical for the two SN

datasets. Figure 7.5 shows that, for $0.38 \lesssim z \lesssim 1.5$, DES has systematically larger absolute magnitudes than Pantheon+ by $\simeq 0.03 - 0.05\,\mathrm{mag}$, mirroring the offset in m_B discussed previously. Additionally, a slight modulation is visible in the reconstructed M_B's in Figure 7.5. This reflects how BAO measurements are converted into D_A, small differences between the transverse and radial BAO scales, which we compress into an isotropic estimate $D_A(z)\,H(z)$, can shift D_A slightly with z. This then propagates into M_B via the DDR used in Equation (4.4). Consistency tests of the DDR in this analysis are compatible with unity at the 1σ level. Importantly, no clear drift with redshift is seen, which could indicate a mismatch in how the probes trace the expansion history or a breakdown of the GP kernel at high redshift. The KDE panels in Figure 7.6 make this clear, the individual redshift colored posteriors cluster around the combined black MCMC posterior with no systematic tilt. The inferred absolute magnitudes at the highest BAO redshift carry large uncertainties (see Fig. 7.5 and 7.6) and contribute very little weight to the final result, removing them does not change the combined mean or uncertainty in any significant way. The final results for the combined absolute magnitude are presented in Figure 7.7. Across all dataset combinations the results are consistent at the 1σ level and clearly cluster closer to the Planck-ΛCDM required absolute magnitude. Quantitatively, the posteriors lie within 0.1-1.6σ of Planck across BAO choices (DES5YR: 0.47-1.62σ; P+: 0.08-0.81σ). The only mild outlier is the hybrid DESI DR1+SDSS combination, which shows a small shift relative to the others, likely reflecting details of how the two BAO sets are merged. In contrast, they are 1.3-3.1σ away from the SH0ES calibration using the Cepheid distance ladder (DES5YR: 1.34-2.39σ; P+: 2.09-3.10σ). Additionally, also a systematic SN catalogues offset is present, for every BAO set M_B^{DES} is less negative than $M_B^{\mathrm{P+}}$ by $\simeq 0.04$ mag, matching the Δm_B offset seen earlier (see Tab. 7.1). The absence of a statistically significant difference between the absolute magnitudes inferred from the two SN datasets is due to the limited constraining power of the CC data. With a tighter anchor, such as CMB-calibrated BAO, differences between the SN samples could become statistically significant. An additional interesting consideration interpreting possible differences between datasets is the sky coverage of the surveys. DES observes on the southern hemisphere, while DESI and SDSS look at the northern sky, the Pantheon+ catalogue is a bit mixed across hemispheres. In the presence of anisotropies, such differences in sky coverage could in principle contribute to systematic shifts between different datasets.

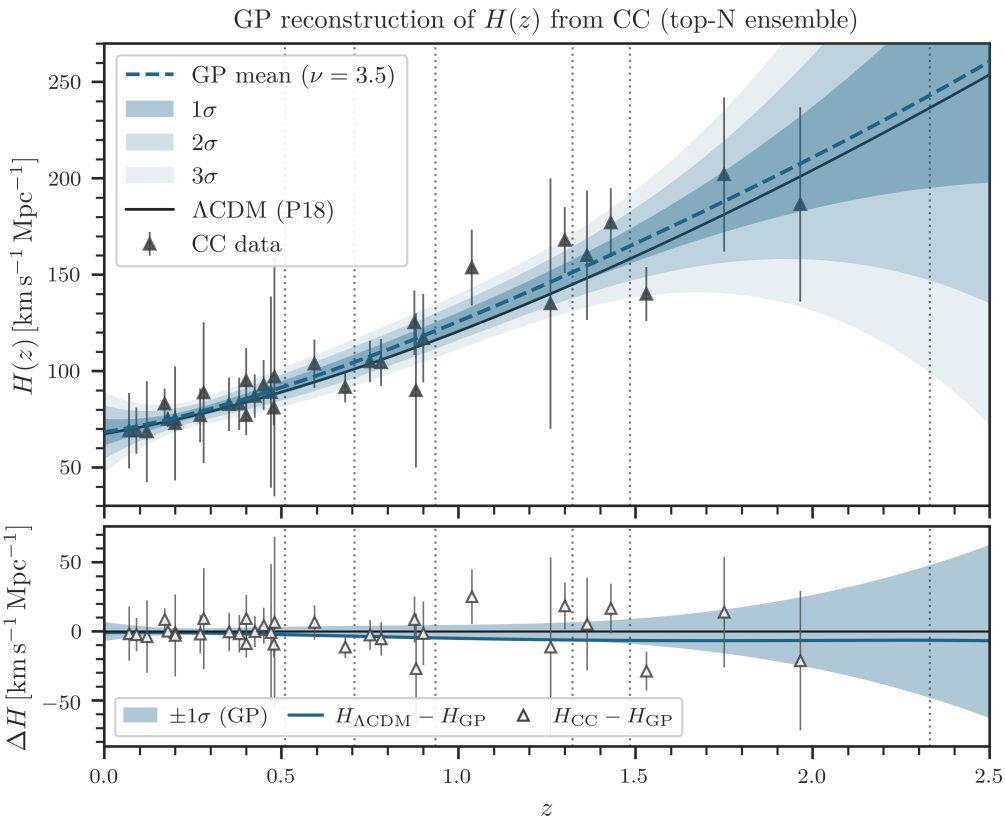

Figure 7.1: *Final GP reconstruction of $H(z)$ from CC data using a Matérn kernel with $\nu = 3.5$. Hyperparameters are selected via K-fold CV ($K = 6$), the mean curve and shaded 1-3σ bands come from the top-N ensemble (trials within $\Delta\mathcal{L} = 0.05$ of the best, 300 trials in total). Vertical dotted lines mark DESI DR2 BAO redshifts and the solid black curve shows the Planck ΛCDM prediction. The lower panel shows $H_{\mathrm{data}} - H_{\mathrm{GP}}$ residuals, with the GP 1σ band and the ΛCDM minus GP mean difference.*

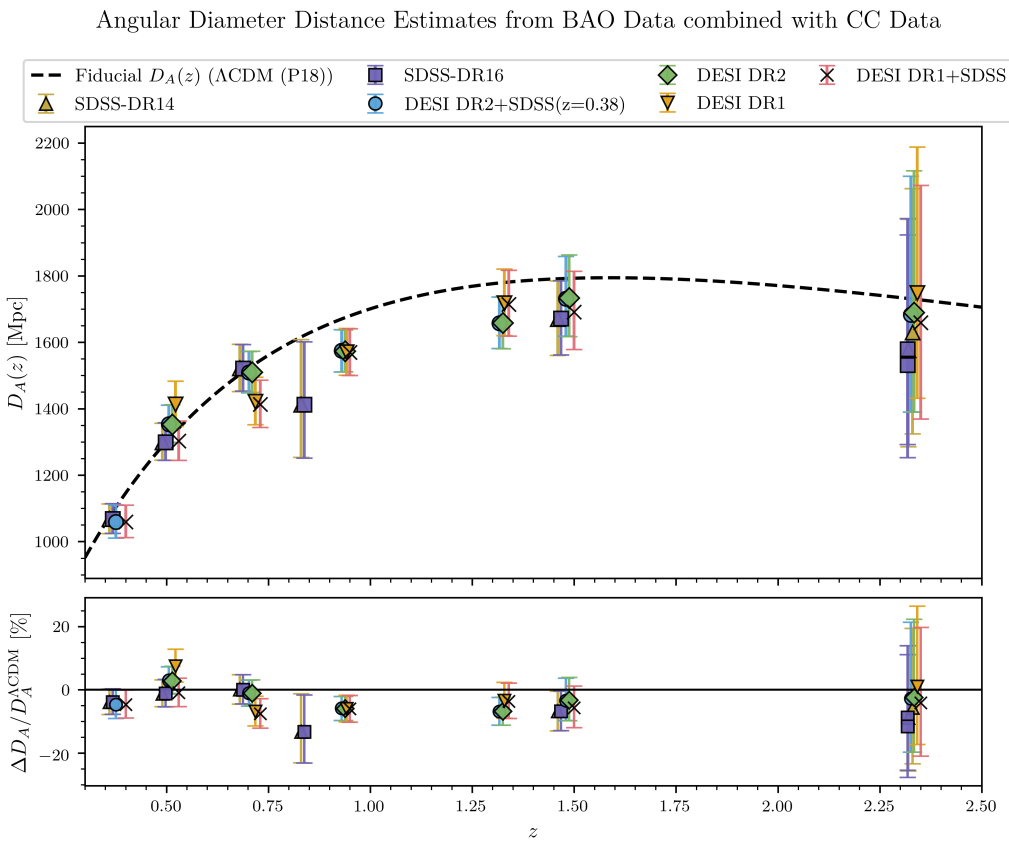

Figure 7.2: *On the top the reconstructed angular diameter distance from six BAO datasets combined with the GP reconstruction of $H(z)$ from CC at the BAO redshifts. For each BAO redshift $X \equiv c\,D_M/[D_H(1+z)]$ is sampled and divided by GP draws of $H(z)$ to obtain D_A. The markers are the posterior medians, and the uncertainty bars are the 16-84% credible intervals. For better visibility points at same redshift have a tiny horizontal jitter. The dashed curve corresponds to D_A obtained from ΛCDM with values from Planck Collaboration [2018]. In the bottom the fractional residual with respect to ΛCDM is shown.*

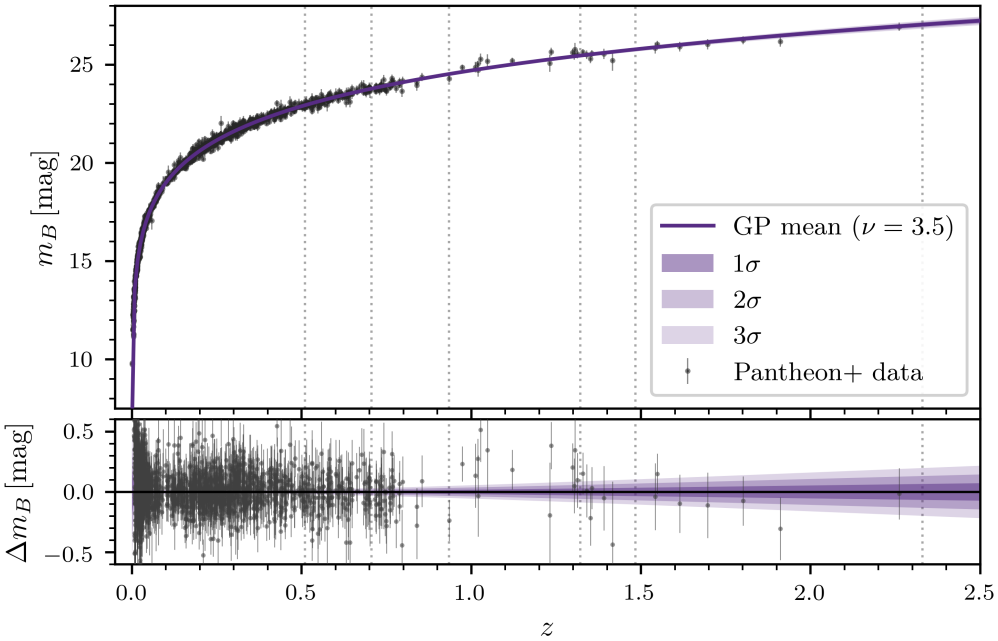

(a) *GP reconstruction for Pantheon+ $m_B(z)$ with Matérn kernel ($\nu = 3.5$).*

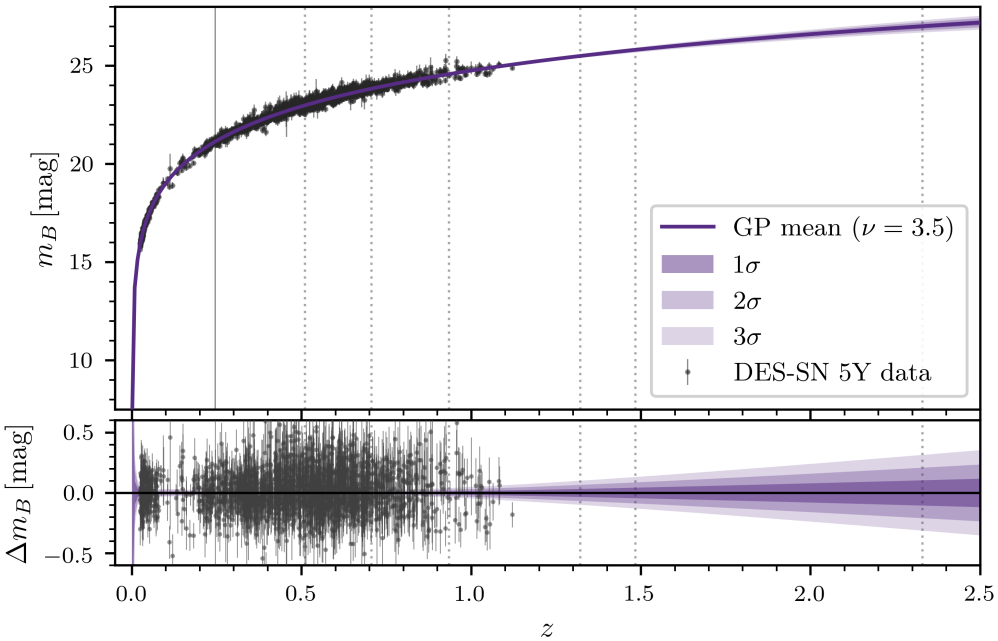

(b) *GP reconstructions for DES-SN 5Y $m_B(z)$ with Matérn kernel ($\nu = 3.5$), with 75 SNe ($\sigma_{m_B} > 1$ mag) omitted in the plot for better visibility.*

Figure 7.3: *GP reconstructions of $m_B(z)$ from top-N ensemble (trials within $\Delta\mathcal{L} = 0.01$ of the best, 50 trials total). Shaded bands show 1-3σ, the lower panels plot $\Delta m_B \equiv m_B - m_B^{\mathrm{GP}}$, and vertical dotted lines mark DESI DR2 redshifts.*

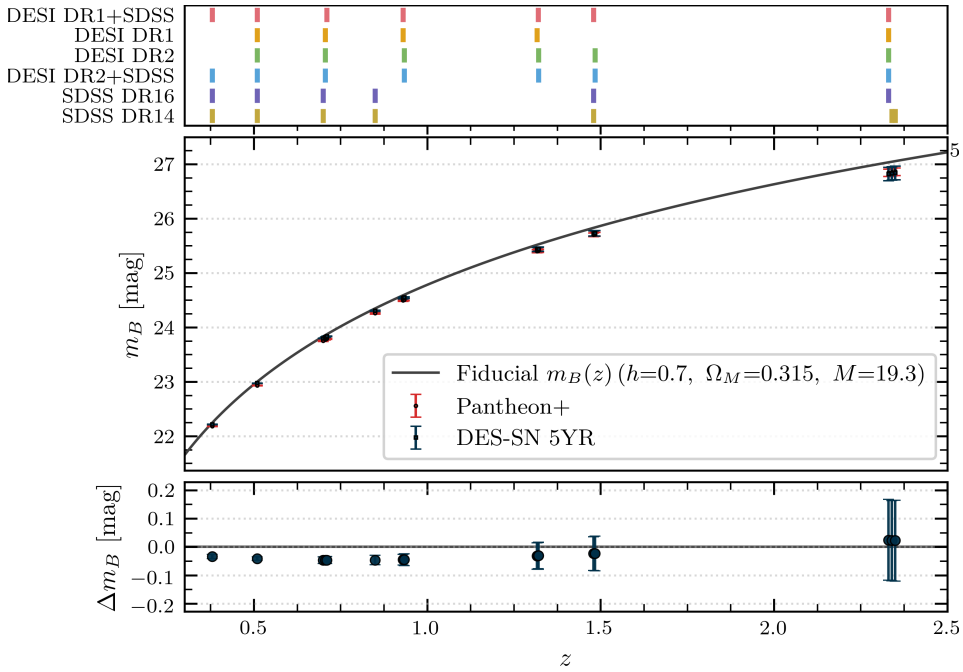

(a) *In the top pannel colored ticks indicate which BAO dataset have data at the at redshift. GP predictions for the apparent magnitudes at the BAO redshifts for all combinations of SN dataset and BAO redshifts with a fiducial m_B curve. The residual panel shows the difference $m_B^{\mathrm{P+}} - m_B^{\mathrm{DES}}$ in predictions for the two SN datasets.*

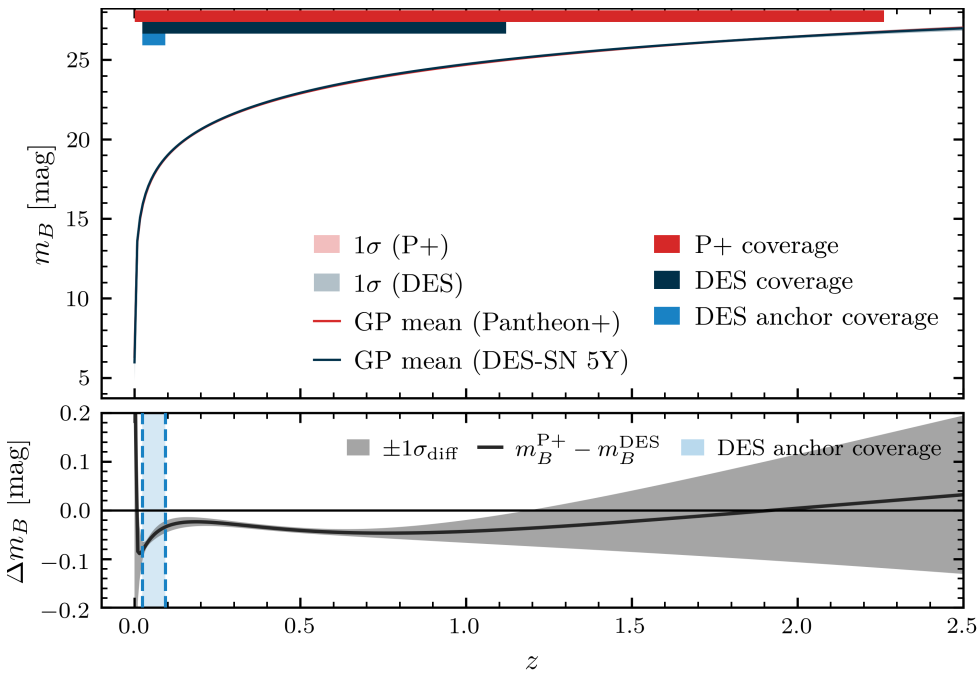

(b) *GP means and 1σ uncertaintes for SN datasets. Colored bars indicate catalogue redshift coverage. In the residual plot the grey band shows $\sigma_{\mathrm{diff}}(z) = (\sigma^2_{\mathrm{P+}}(z) + \sigma^2_{\mathrm{DES}}(z))^{1/2}$.*

Figure 7.4: *Comparison of SN GP reconstructions.*

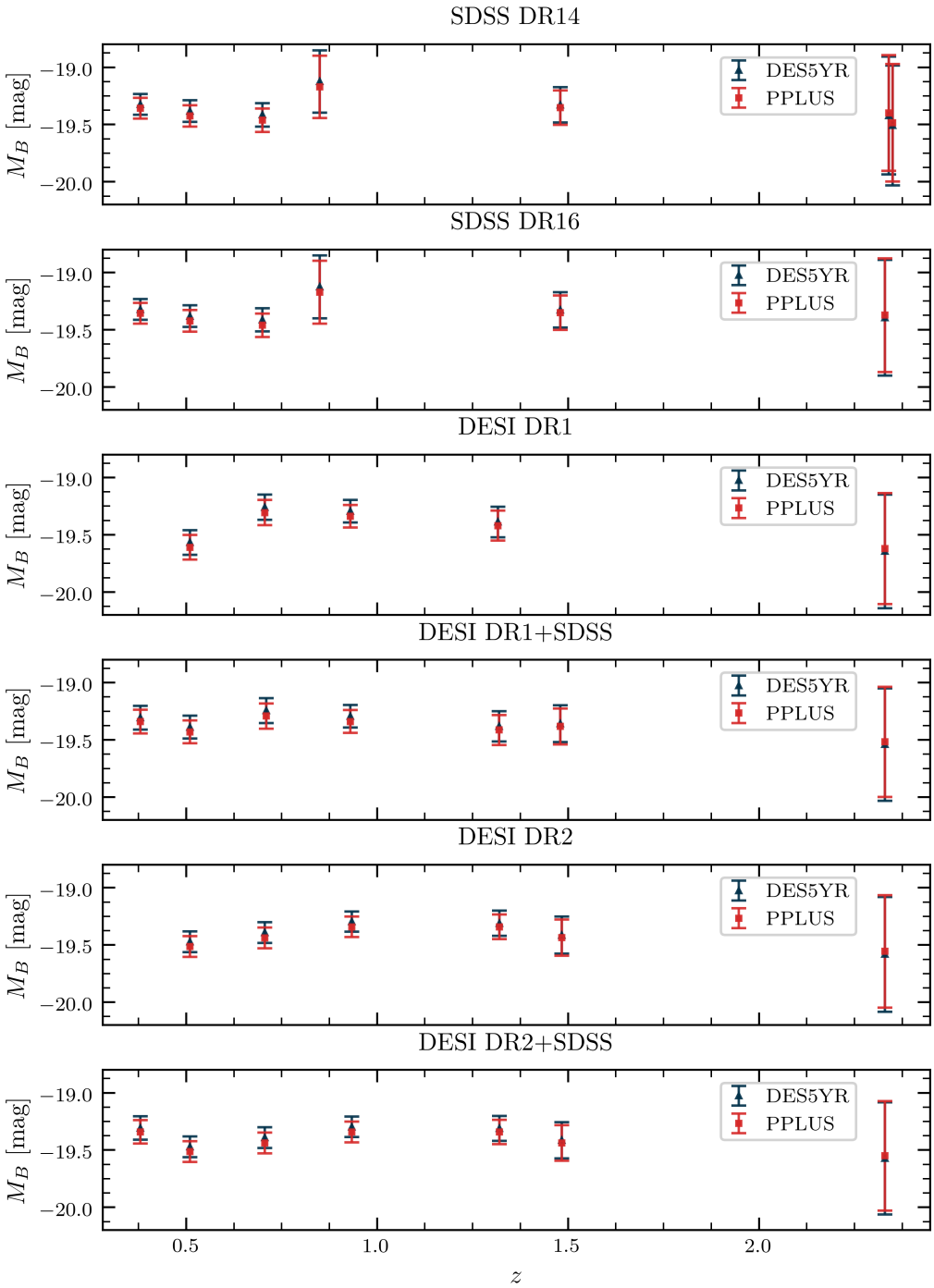

Figure 7.5: *Means with 1σ uncertainties of the reconstructed M_B at each BAO redshift. Results are obtained from the joint BAO+CC angular diameter distance and SNe Ia reconstructions of m_B (DES-SN 5YR and Pantheon+) utilizing the distance duality relation.*

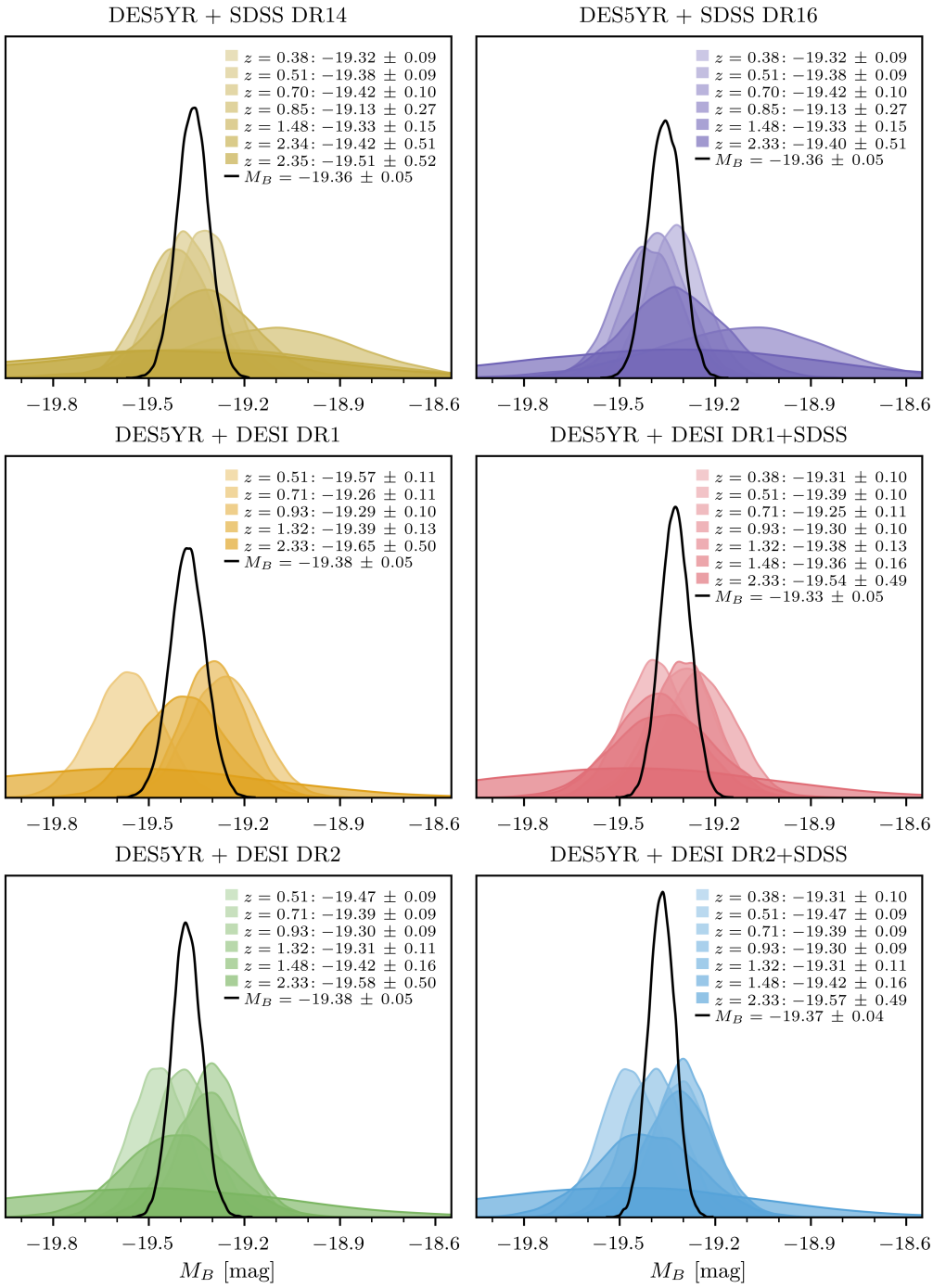

(a) *Using DES-SN 5YR as the SNe sample.*

Figure 7.6: *KDE plots for reconstructed M_B's at the BAO redshifts, grouped by BAO dataset. In each panel, semi-transparent colored curves are the per-redshift posteriors; the solid black curve is the MCMC posterior of the combined M_B.*

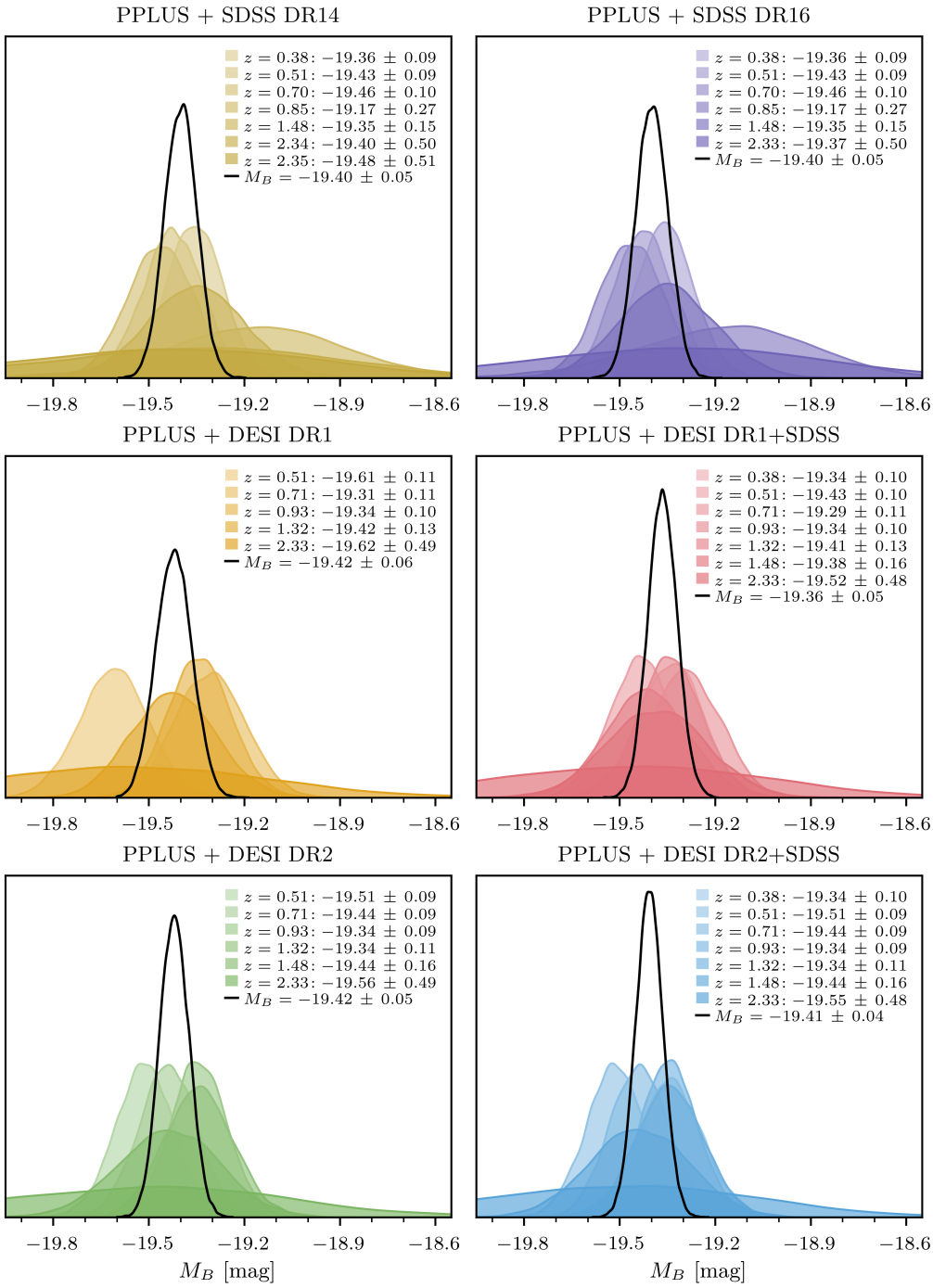

(b) *Using Pantheon+ as the SNe sample.*

Figure 7.6: *KDE plots for reconstructed M_B's at the BAO redshifts, grouped by BAO dataset. In each panel, semi-transparent colored curves are the per-redshift posteriors; the solid black curve is the MCMC posterior of the combined M_B.*

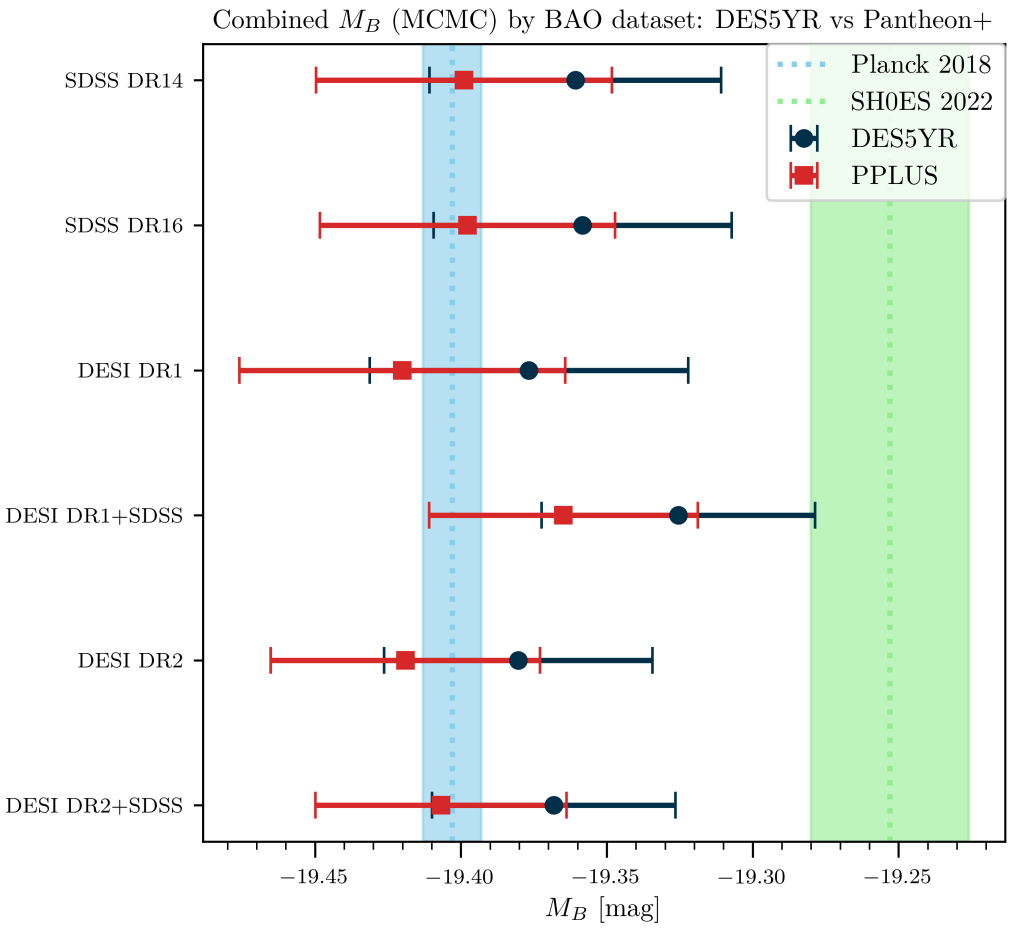

Figure 7.7: *Posterior means and 1σ uncertainties of the absolute magnitude M_B obtained from the combination of CC, BAO and SN data via the distance-duality relation. The vertical axis lists the BAO datasets all combined with the same CC data, with the two SNIa reconstructions shown side by side. The light green band marks the calibrated $M_B^{\mathrm{R22}} = -19.253 \pm 0.027\,\mathrm{mag}$ inferred by Riess et al. [2022] using the Cepheid distance ladder, while the light blue band marks the $M_B = -19.403 \pm 0.010\,\mathrm{mag}$ required by the Planck Collaboration [2018] measurements under ΛCDM.*

BAO / SN	M_B [mag]	vs Planck (σ)	vs SH0ES (σ)	ΔM_B [mag]
SDSS DR14				
DES-SN 5YR	-19.36 ± 0.05	0.83	1.90	
Pantheon+	-19.40 ± 0.05	0.08	2.54	-0.04
SDSS DR16				
DES-SN 5YR	-19.36 ± 0.05	0.86	1.82	
Pantheon+	-19.40 ± 0.05	0.10	2.52	-0.04
DESI DR1				
DES-SN 5YR	-19.38 ± 0.05	0.47	2.03	
Pantheon+	-19.42 ± 0.06	0.30	2.69	-0.04
DESI DR1 + SDSS				
DES-SN 5YR	-19.33 ± 0.05	1.62	1.34	
Pantheon+	-19.36 ± 0.05	0.81	2.09	-0.04
DESI DR2				
DES-SN 5YR	-19.38 ± 0.05	0.48	2.39	
Pantheon+	-19.42 ± 0.05	0.34	3.10	-0.04
DESI DR2 + SDSS				
DES-SN 5YR	-19.37 ± 0.04	0.81	2.32	
Pantheon+	-19.41 ± 0.04	0.09	3.03	-0.04

Table 7.1: *Absolute magnitude M_B from the joint SN+BAO+CC analysis. The quoted values are posterior means with 1σ errors, together with their tension in units of σ with Planck under ΛCDM ($M_B = -19.40 \pm 0.01\,\mathrm{mag}$) and SH0ES Cepheid calibration ($M_B^{\mathrm{R22}} = -19.25 \pm 0.03\,\mathrm{mag}$). The rightmost column shows the offset between Pantheon+ and DES-SN 5YR for each BAO dataset.*

After estimating M_B at the BAO redshifts, the expansion parameters from the joint likelihood of Equation (4.8) can be estimated to account for the non-trivial correlation between low and high redshift SNe. The results in Figure 7.8 and Table 7.2 show that H_0 from Pantheon+ is systematically higher than from DES-SN 5YR by about 1.3-1.4 $\mathrm{km\,s^{-1}\,Mpc^{-1}}$ across all BAO choices. Yet, the two SN catalogues give statistically consistent results within 1σ (0.49-0.67σ). Across all dataset combinations, the relative 1σ error on H_0 is between $\sim 2.0 - 2.7\%$. Each determination is statistically consistent with the Planck ΛCDM value of H_0 (DES5YR: 0.21 to 0.59σ; P+: 0.19 to 1.26σ from Planck) and shows a 2.3 to 3.6σ tension with the SH0ES H_0 (DES5YR: 2.66 to 3.62σ; P+: 1.90 to 3.10σ). The deceleration and jerk parameters are nearly identical between catalogues ($q_0 \approx -0.57$ to -0.58 and $j_0 \approx 1$), with q_0 agreeing well with the result from Riess

et al. [2022] on Pantheon+, and with j_0 only poorly constrained in the low redshift range $0.023 < z < 0.15$. Since q_0 and j_0 agree between the two SN datasets, any difference in H_0 must enter through the apparent magnitudes via the intercept, $a_B(z) = \log_{10}\Big[c\,z\,f(z; q_0, j_0)\Big] - 0.2\,m_B(z)$. Recall that a_B is determined from the low-z SNe ($0.023 < z < 0.15$), independent of BAO. In this range the SN datasets show a photometric offset with $m_B^{\mathrm{P+}} < m_B^{\mathrm{DES}}$ (see Figs 7.4b), which translates into to a larger intercept for Pantheon+. The inferred intercepts are

$$\begin{aligned} a_B^{\mathrm{DES}} &= 0.6981 \pm 0.0014, \\ a_B^{\mathrm{P+}} &= 0.7146 \pm 0.0010, \end{aligned} \tag{7.1}$$

a tension exceeding 9σ. The Pantheon reference $a_B = 0.7127 \pm 0.0012$ [Riess et al., 2016] lies within 1.2σ of $a_B^{\mathrm{P+}}$. Note that, Pantheon+ contains more low-z SNe and uses slightly different processing, leading to a different mean and smaller error.

The a_B allows to link the measured absolute magnitudes at the BAO redshifts to an H_0 estimate via Equation (4.7), rewriting this yields

$$\log_{10} H_0 \;=\; a_B + 0.2\,M_B + 5. \tag{7.2}$$

If one defines all differences as Pantheon+ minus DES, $\Delta X \equiv X^{\mathrm{P+}} - X^{\mathrm{DES}}$. Then the numerical differences are

$$\Delta a_B = 0.7146 - 0.6981 = +0.0165, \qquad \Delta M_B \approx -0.040 \text{ mag}.$$

Plugging this into Equation (7.2) yields

$$\Delta \log_{10} H_0 \;=\; \underbrace{\Delta a_B}_{+0.0165} \;+\; \underbrace{0.2\,\Delta M_B}_{-0.008} \;\approx\; +0.0085,$$

so that the difference in the Hubble constant is,

$$\frac{H_0^{\mathrm{P+}}}{H_0^{\mathrm{DES}}} \approx 10^{\,0.0085} \approx 1.02,$$

that is the $\sim 2\%$ increase, about $+1.3\,\mathrm{km\,s^{-1}\,Mpc^{-1}}$ at $h = 0.67$, one can see in Table 7.2. To summarize: $m_B^{\mathrm{P+}} < m_B^{\mathrm{DES}} \Rightarrow a_B^{\mathrm{P+}} > a_B^{\mathrm{DES}}$ and although $M_B^{\mathrm{P+}}$ is more negative (partially lowering H_0), the larger intercept dominates, leaving Pantheon+ with the higher H_0.

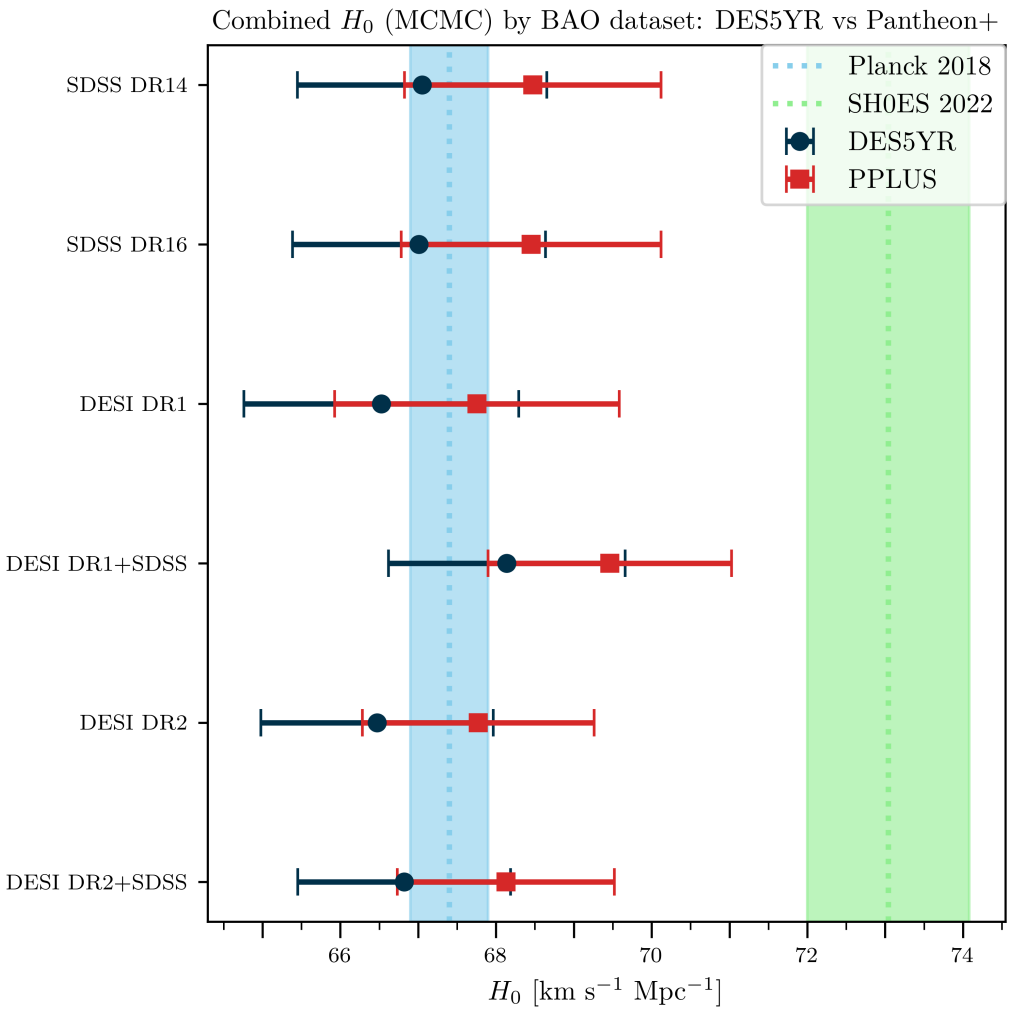

Figure 7.8: *Posterior means and 1σ uncertainties of H_0 obtained from the joint-likelihood analysis, which combines the low redshift Hubble flow SNe with high-redshift SN, BAO, and CC data into a single MCMC. The vertical axis lists the BAO datasets all combined with the same CC data, with the two SNIa reconstructions shown side by side. The light green band marks the value by Riess et al. [2022], $H_0^{R22} = 73.04 \pm 1.04\,\mathrm{km\,s^{-1}\,Mpc^{-1}}$, while the light blue band marks the value by Planck Collaboration [2018] under ΛCDM, $H_0^{P18} = 67.4 \pm 0.5\,\mathrm{km\,s^{-1}\,Mpc^{-1}}$.*

BAO / SN	H_0 [km s^{-1} Mpc^{-1}]	q_0	j_0
SDSS DR14			
Pantheon+	68.47 ± 1.65	-0.58 ± 0.08	1.00 ± 0.54
DES-SN 5YR	67.05 ± 1.60	-0.57 ± 0.13	1.00 ± 0.55
SDSS DR16			
Pantheon+	68.45 ± 1.67	-0.57 ± 0.08	1.00 ± 0.55
DES-SN 5YR	67.01 ± 1.62	-0.57 ± 0.12	1.03 ± 0.55
DESI DR1			
Pantheon+	67.76 ± 1.83	-0.58 ± 0.08	1.00 ± 0.54
DES-SN 5YR	66.53 ± 1.77	-0.57 ± 0.13	0.99 ± 0.54
DESI DR1+SDSS			
Pantheon+	69.46 ± 1.57	-0.57 ± 0.08	1.00 ± 0.55
DES-SN 5YR	68.14 ± 1.52	-0.58 ± 0.13	1.01 ± 0.54
DESI DR2			
Pantheon+	67.77 ± 1.49	-0.58 ± 0.08	1.01 ± 0.55
DES-SN 5YR	66.47 ± 1.49	-0.58 ± 0.13	1.01 ± 0.55
DESI DR2 + SDSS			
Pantheon+	68.13 ± 1.39	-0.57 ± 0.08	1.00 ± 0.55
DES-SN 5YR	66.82 ± 1.37	-0.57 ± 0.13	1.00 ± 0.54

Table 7.2: *Posterior means and 1σ uncertainties for H_0, q_0, j_0 from the joint likelihood analysis using MCMC. DES systematically smaller values of H_0, but within 1σ of Pantheon+. The q_0's and j_0's are almost identical for all datasets, while j_0 is not getting very constrained in the redshift range of interest.*

7.2 Comparison to Similar Methodologies

The result for SDSS DR14 + CC combined with Pantheon+ ($M_B = -19.40 \pm 0.05\,\mathrm{mag}$ and $H_0 = 68.47 \pm 1.65\,\mathrm{km\,s^{-1}\,Mpc^{-1}}$) is in excellent agreement with the similar analysis of Renzi and Silvestri [2023], who report $M_B = -19.36 \pm 0.05\,\mathrm{mag}$ and $H_0 = 68.5 \pm 1.5\,\mathrm{km\,s^{-1}\,Mpc^{-1}}$, using the Pantheon catalogue instead of Pantheon+ and a slightly different methodology (see Sec. 6.4).

Using the same idea with the DDR and data from DESI DR1 and Pantheon+, Guo et al. [2025] obtain $H_0 = 68.4^{+1.0}_{-0.8}\,\mathrm{km\,s^{-1}\,Mpc^{-1}}$, consistent with the 67.76 ± 1.83 for the same data in this work. Their noticeably smaller error

bars likely reflect methodological choices that significantly compress uncertainties: (i) treating the BAO redshifts as independent when combining them (neglecting correlations between them); (ii) anchoring the SN and CC GP's to a ΛCDM (or w_0w_a) mean, which shrinks variance but also biases the reconstructions toward the prior mean; (iii) possibly under propagating CC systematics by not using a full CC covariance. Additionally, an external prior on a_B from Pantheon is used, even though they use the Pantheon+ data, and their per-redshift H_0 error appear uneven (e.g. smaller at $z = 2.33$ than at $z = 1.317$), a counter intuitive pattern. Despite these caveats, their H_0 remains statistically consistent with the results here at the 1σ level.

A model-independent study by Favale et al. [2023] finds $M_B = -19.31^{+0.09}_{-0.11}$ mag and $H_0 = 71.5 \pm 3.1\,\mathrm{km\,s^{-1}\,Mpc^{-1}}$ using Pantheon+ (excluding SNe employed by SH0ES), BAO data from various surveys, and CC data. In terms of the absolute magnitude, their host-excluded value is a bit brighter than the range estimated here, but statistically consistent given the uncertainties. Their corresponding H_0 is consequently also higher by 1-1.5σ. The main reason for this difference is the GP setup, hyperparameters are fixed by maximizing the log-marginal likelihood, and their reported normalized $\tilde{\chi}^2$ values are well below unity, indicating over-smoothed fits and/or inflated predictive variances. Consistent with this, their Figure 2 shows significant wiggles in the uncertainties of $m_B(z)$ and $H(z)$ dipping at the high redshift and turning upward as $z \to 0$, this leads to a significant deviation from ΛCDM and can explain the brighter M_B and larger H_0.

7.3 Connection to the Hubble Tension

The method in this work relies on uncalibrated SNe Ia (independent of locally calibrated M_B), the combined isotropic BAO observable $H(z)D_M(z)/c$ (independent of sound horizon), and CC data for $H(z)$, all tied together by the DDR. As a result, the inference of the absolute magnitude M_B is robust against systematic offsets in stellar-population based distance calibrations. This explains why residual systematic biases in Cepheids, TRGB, or JAGB (e.g. crowding, metallicity, etc.) do not propagate into the M_B here. Instead, the analysis remains sensitive only to systematics internal to the SN standardization itself (e.g. the mass step, local SFR, light curve fitting, bias corrections), as seen in the $\Delta M_B \sim 0.04$ mag offset between Pantheon+ and DES-5YR. The calibration free inferred M_B (see Tab. 7.1) supports the determination from the inverse distance ladder, which is not surprising since M_B is measured in the range where BAO data exists ($0.3 \lesssim z \lesssim 2.3$) and the

CC reconstruction of $H(z)$ is within 1σ of ΛCDM, whereas the local distance ladder methods calibrates M_B in a much nearer region ($0.002 \lesssim z \lesssim 0.01$). Interestingly, the measured M_B is also consistent with the CCHP population-II calibrations by Freedman et al. [2025] of SNe Ia (TRGB and JAGB). It remains in 2-3σ tension with the brighter calibration adopted by SH0ES, i.e. the M_B values are fainter by $\sim$ 0.10-0.17 mag depending on dataset. [Freedman et al., 2025] highlights three points that are relevant to this absolute magnitude discussion: (i) the current calibrator pool is still small, and modest reprocessing or sample changes at the few hundredths of a mag level can shift the mean M_B, (ii) there is evidence for a trend of inferred M_B with host distance in the SH0ES Cepheid sample, possibly linked to resolution and crowding at $d \gtrsim$ 20-40 Mpc, and (iii) JWST imaging of the more distant hosts is expected to reduce both crowding and selection effects Freedman et al. [2025]. At the same time, several other distance ladder methods independent of TRGB or Cepheids (e.g. Miras, Type II SNe, surface-brightness fluctuations, Tully-Fisher, HII galaxies) still cluster around $h \simeq$ 0.72-0.74 (see Tab. 7.2), although with larger uncertainties. Reconciling the SH0ES and Planck scales corresponds to a shift in the absolute magnitude scale of $\Delta M \approx 0.15$ mag. A similar offset is absolute magnitude is required here to bring the measured M_B into agreement with SH0ES, since distance ladder calibration systematics are included, the remaining source of systematic uncertainty lies within the SN standardization. But, the persistence of high late-time H_0 values across multiple indicators and methods (see Tab. 3.1), that do not depend on the Type Ia absolute magnitude, indicates it is more likely that there is either a physical or systematic offset for the whole local distance ladder at very low redshift. Such a shift could be explained by photons losing energy in our local environment, hypothetically this could happen due to a crossing into a gravitational field of an extended massive object. Given the good agreement with the global ΛCDM model, instead of changing the late time expansion history it might be interesting to look at nearby modifications of the FLRW metric, an interesting model candidate could be the McVittie metric (see Sec. 3.4.2). Recent work by Sah et al. [2025] finds that the Pantheon+ catalogue itself shows statistically significant dipolar anisotropies, H_0 varies by more than $1.5\,\mathrm{km\,s^{-1}\,Mpc^{-1}}$ in the range $0.023 < z < 0.15$, which is larger than the precision measured by SH0ES, and the deceleration parameter q_0 exhibits a redshift dependent dipolar modulation at $> 5\sigma$ significance. These results suggest that part of the discrepancy in late universe measurements may be linked to anisotropic bulk flows in the local Universe, rather than to isotropic modifications of the cosmological model.

Early-time modifications raise the CMB inferred H_0 primarily by reducing the sound horizon (see Sec. 3.4.2). A crucial point is that the analysis in this work does not depend on the sound horizon, so theoretical modifications to the sound horizon do not affect the inferred M_B and H_0. Within current uncertainties, the data favour an absolute magnitude closer to the inverse distance ladder, i.e. the absolute magnitude one would obtain with the sound horizon of ΛCDM. Hence, early-time changes that act only through r_d seem insufficient on their own, bringing the measurements together would also require a shift in the absolute magnitude scale and/or a different coherent local effect. This does not rule out early-time physics modifications, but it limits their explanatory power in this context.

8 Conclusion

This thesis develops and applies the idea by Renzi and Silvestri [2023] for a calibration free and sound horizon independent route to the Hubble constant by combining uncalibrated SNe Ia data from Pantheon+ and DES-SN 5Y, unanchored BAO data from SDSS and DESI, and 33 cosmic chronometers measurements, under the distance duality relation (DDR). The method is essentially independent of a cosmological model, since Gaussian processes allow for a non-parametric reconstruction of $m_B(z)$ from SNe and $H(z)$ from cosmic chronometers. The analysis only depends on a FLRW geometry for the luminosity distance expansion at low redshift and the DDR assumes standard photon propagation in a metric theory of gravity. Astrophysical modeling in the CC data (stellar population synthesis models, initial mass function, stellar libraries, and star formation history), is accounted for through the full CC covariance matrix,

The GP reconstruction of $H(z)$ from CC agrees with ΛCDM within 1σ over $0 \lesssim z \lesssim 2.5$. BAO and CC give angular diameter distances that are consistent across SDSS and DESI releases, small inconsistencies at low redshifts between SDSS and DESI DR1 are resolved with DESI DR2. The SN datasets are statistically consistent, but show a catalogue offset of about 0.04 mag, including a low-z feature near the DES anchor subset and a residual offset at higher z, directly propagating into a nearly constant $\Delta M_B \simeq -0.04$ mag (DES M_B is fainter, i.e. less negative) and into a $\sim 2\%$ higher H_0 for Pantheon+ than for DES. The inferred absolute magnitudes cluster around $M_B \simeq -19.36$ to -19.42 mag (excluding the hybrid DESI DR1+SDSS case as a mild outlier), close to the value implied by Planck under ΛCDM and in 2-3σ tension with the brighter SH0ES calibration. The joint likelihood over (H_0, q_0, j_0) yields $H_0 \simeq 66.5 - 68.5\,\mathrm{km\,s^{-1}\,Mpc^{-1}}$ with $2.0 - 2.7\%$ uncertainties, consistent with the inverse distance ladder and in tension with SH0ES at the 2.3-3.6σ level. DDR tests show no significant redshift drift, q_0 is consistent across datasets and with other literature, while the jerk parameter j_0 is only weakly constrained in the low-z range.

It is more accurate to view the discrepancy between early and late time measurements as an absolute magnitude tension, not only an H_0 tension. The calibration free M_B estimated at the BAO redshifts here supports the inverse distance ladder. To bridge the SH0ES and Planck scales one would

have to find an explanation why the SH0ES calibrated magnitude is dimmer by about $\Delta M \sim 0.15\,\mathrm{mag}$, mapping to a $\sim 7\%$ higher H_0. Since several non-SN local methods also prefer a higher H_0, any resolution likely needs a coherent effect across the local ladder, possibly a mix of systematics and variations in the very late-time physics. Early-time changes that only reduce the sound horizon r_d usually leave M_B untouched, so they are not sufficient on their own to reconcile the full set of observables, particularly because the data driven M_B agrees with the inverse distance ladder from the CMB. Any full explanation must also account for the absolute magnitude scale and the full SN magnitude-redshift relation.

With only the DDR linking the probes, the pipeline provides data consistency check. At the BAO redshifts there is no monotonic drift in M_B, independent BAO sets mapped through CC give compatible $D_A(z)$, and the small offset in the SN catalog propagates into a shift in a_B and M_B. The small modulation of $M_B(z)$ can be explained by compressing the two BAO scales into the isotropic $H(z)D_M(z)/c$ and then converting to D_A with CC, which induces mild redshift dependent shifts within the errors, not a DDR violation. Any failure of these checks would point to residual systematics or a breakdown of the minimal assumptions.

Upcoming data will help to specify these conclusions. An increased sample size for the CC measurements (e.g. from Euclid) will reduce uncertainties in the reconstruction of the expansion rate. BAO carry much of the constraining power in this setup, so the final DESI data will help to tighten the errorbars. At low redshift, the Zwicky Transient Facility will provide a much larger and more uniform Hubble flow SN sample ($z \lesssim 0.1$), improving the intercept a_B, reducing sensitivity to catalogue processing differences, and strengthening cross-checks of SN standardization on the nearby rung. JWST observations of more distant calibrator hosts will probe crowding, metallicity, and selection at the few-hundredths of a mag level. Gravitational waves with an electromagnetic counterpart could be easily integrated into the pipeline, as they directly give a measure of $D_L(z)$. Gravitational waves with an electromagnetic counterpart (bright sirens) fit naturally into this pipeline, as they provide a direct $D_L(z)$ at a known redshift and do not rely on photon calibration. For events without a counterpart (dark sirens), statistical redshifts can be used, in parallel, BAO+CC with DDR give a prediction for $D_L(z)$, which can be compared to the GW distances. For the hypothetical inclusion of future redshift drift measurements for $H(z)$ one should be careful not to use it as a one-to-one replacement for the CC based $H(z)$ in this pipeline. CC infer a volume averaged expansion rate, whereas redshift drift measures $H(z)$ along the line-of-sight, so that in the presence

of cosmic backreaction, the two measurements won't coincide. As a future extension, the DDR can be relaxed by introducing a small deviation $\eta(z)$ via $D_L(z) = D_A(z)(1+z)^2\,\eta(z)$ and fitting $\eta(z)$ jointly, as done in prior DDR tests by Renzi et al. [2022].

In essence, this work provides a simple, data-driven, and model-independent reference for checking consistency across late-universe probes, and serves as one small piece in the broader effort to address the Hubble tension.

> "It is the mountains that take me by surprise, they lift me because they remain tied to their mysterious origins and are unaware of the final shore."
> — Etel Adnan in *Sea and Fog*

Bibliography

Addison, G. E., Watts, D. J. H., Bennett, C. L., and Halpern, M. (2018). Elucidating ΛCDM: Impact of Early-Universe Physics on the CMB-Inferred Hubble Constant. *Astrophysical Journal*, 853:119. doi:10.3847/1538-4357/aaa1ed. arXiv:1707.06547.

Aiola, S. e. (2020). The Atacama Cosmology Telescope: DR4 maps and first ΛCDM cosmological parameters. *Journal of Cosmology and Astroparticle Physics*, 12:047. doi:10.1088/1475-7516/2020/12/047. arXiv:2007.07288.

Akarsu, O., Kumar, S., Özulker, E., Vázquez, J. A., and Yadav, A. (2023). Relaxing cosmological tensions with a sign switching cosmological constant: Improved results with Planck, BAO, and Pantheon data. *Physical Review D*, 108(2):023513. doi:10.1103/PhysRevD.108.023513. arXiv:2211.05742.

Alam, S., Ata, M., Bailey, S., Beutler, F., Bizyaev, D., Blazek, J. A., Bolton, A. S., Brownstein, J. R., Burden, A., Chuang, C.-H., Comparat, J., Cuesta, A. J., Dawson, K. S., Eisenstein, D. J., Escoffier, S., Gil-Marin, H., Grieb, J. N., Hand, N., Ho, S., Kinemuchi, K., Kirkby, D., Kitaura, F., Malanushenko, E., Malanushenko, V., Maraston, C., McBride, C. K., Nichol, R. C., Olmstead, M. D., Oravetz, D., Padmanabhan, N., Palanque-Delabrouille, N., Pan, K., Pellejero-Ibanez, M., Percival, W. J., Petitjean, P., Prada, F., Price-Whelan, A. M., Reid, B. A., Rodriguez-Torres, S. A., Roe, N. A., Ross, A. J., Ross, N. P., Rossi, G., Rubino-Martin, J. A., Sanchez, A. G., Saito, S., Salazar-Albornoz, S., Samushia, L., Satpathy, S., Scoccola, C. G., Schlegel, D. J., Schneider, D. P., Seo, H.-J., Simmons, A., Slosar, A., Strauss, M. A., Swanson, M. E. C., Thomas, D., Tinker, J. L., Tojeiro, R., Magana, M. V., Vazquez, J. A., Verde, L., Wake, D. A., Wang, Y., Weinberg, D. H., White, M., Wood-Vasey, W. M., Yeche, C., Zehavi, I., Zhai, Z., and Zhao, G.-B. (2017). The clustering of galaxies in the completed SDSS-III Baryon Oscillation Spectroscopic Survey: cosmological analysis of the DR12 galaxy sample. *Mon. Not. Roy. Astron. Soc.*, 470(3):2617–2652. doi:10.1093/mnras/stx721. arXiv:1607.03155.

Alam, S., Aubert, M., Avila, S., Balland, C., Bautista, J. E., Bershady, M. A., Bizyaev, D., Blanton, M. R., Bolton, A. S., Bovy, J., Brinkmann, J.,

Brownstein, J. R., Burtin, E., Chabanier, S., Chapman, M. J., Choi, P. D., Chuang, C.-H., Comparat, J., Cuceu, A., Dawson, K. S., de la Macorra, A., de la Torre, S., de Mattia, A., de Sainte Agathe, V., du Mas des Bourboux, H., Escoffier, S., Etourneau, T., Farr, J., Font-Ribera, A., Frinchaboy, P. M., Fromenteau, S., Gil-Marín, H., Gonzalez-Morales, A. X., Gonzalez-Perez, V., Grabowski, K., Guy, J., Hawken, A. J., Hou, J., Kong, H., Klaene, M., Kneib, J.-P., Goff, J.-M. L., Lin, S., Long, D., Lyke, B. W., Cousinou, M.-C., Martini, P., Masters, K., Mohammad, F. G., Moon, J., Mueller, E.-M., noz Gutiérrez, A. M., Myers, A. D., Nadathur, S., Neveux, R., Newman, J. A., Noterdaeme, P., Oravetz, A., Oravetz, D., Palanque-Delabrouille, N., Pan, K., III, J. P., Paviot, R., Percival, W. J., Pérez-Ràfols, I., Petitjean, P., Pieri, M. M., Prakash, A., Raichoor, A., Ravoux, C., Rezaie, M., Rich, J., Ross, A. J., Rossi, G., Ruggeri, R., Ruhlmann-Kleider, V., Sánchez, A. G., Sánchez, F. J., Sánchez-Gallego, J. R., Sayres, C., Schneider, D. P., Seo, H.-J., Shafieloo, A., Slosar, A., Smith, A., Stermer, J., Tamone, A., Tinker, J. L., Tojeiro, R., na, M. V.-M., Variu, A., Wang, Y., Weaver, B. A., Weijmans, A.-M., Yèche, C., Zarrouk, P., Zhao, C., Zhao, G.-B., and Zheng, Z. (2021). The Completed SDSS-IV Extended Baryon Oscillation Spectroscopic Survey: Cosmological Implications from Two Decades of Spectroscopic Surveys at the Apache Point Observatory. *Physical Review D*, 103(8):083533. doi:10.1103/PhysRevD.103.083533. arXiv:2007.08991.

Alestas, G., Kazantzidis, L., and Perivolaropoulos, L. (2021). A phantom transition at $z_t < 0.01$ as a resolution of the Hubble tension. *Phys. Rev. D*, 103(8):083517. doi:10.1103/PhysRevD.103.083517. arXiv:2008.05817.

Alfradique, V., Bom, C. R., Palmese, A., Teixeira, G., Santana-Silva, L., Drlica-Wagner, A., Riley, A. H., Martínez-Vázquez, C. E., Sand, D. J., Stringfellow, G. S., Medina, G. E., Carballo-Bello, J. A., Choi, Y., Esteves, J., Limberg, G., Mutlu-Pakdil, B., Noël, N. E. D., Pace, A. B., Sakowska, J. D., and Wu, J. F. (2024). A Dark Siren Measurement of the Hubble Constant Using Gravitational Wave Events from the First Three LIGO/Virgo Observing Runs and DELVE. *Monthly Notices of the Royal Astronomical Society*, 528(2):3249–3259. doi:10.1093/mnras/stae086. arXiv:2310.13695.

Anderson, R. I., Koblischke, N. W., and Eyer, L. (2024). Small-amplitude Red Giants Elucidate the Nature of the Tip of the Red Giant Branch as a Standard Candle. *The Astrophysical Journal Letters*, 963(2):L43. doi:10.3847/2041-8213/ad284d. arXiv:2303.04790.

Balkenhol, L., Dutcher, D., Spurio Mancini, A., Doussot, A., Benabed, K.,

Galli, S., Ade, P. A. R., Anderson, A. J., Ansarinejad, B., Archipley, M., Bender, A. N., Benson, B. A., Bianchini, F., Bleem, L. E., Bouchet, F. R., Bryant, L., Camphuis, E., Carlstrom, J. E., Cecil, T. W., Chang, C. L., Chaubal, P., Chichura, P. M., Chou, T.-L., Coerver, A., Crawford, T. M., Cukierman, A., Daley, C., de Haan, T., Dibert, K. R., Dobbs, M. A., Everett, W., Feng, C., Ferguson, K. R., Foster, A., Gambrel, A. E., Gardner, R. W., Goeckner-Wald, N., Gualtieri, R., Guidi, F., Guns, S., Halverson, N. W., Hivon, E., Holder, G. P., Holzapfel, W. L., Hood, J. C., Huang, N., Knox, L., Korman, M., Kuo, C.-L., Lee, A. T., Lowitz, A. E., Lu, C., Millea, M., Montgomery, J., Nakato, Y., Natoli, T., Noble, G. I., Novosad, V., Omori, Y., Padin, S., Pan, Z., Paschos, P., Prabhu, K., Quan, W., Rahimi, M., Rahlin, A., Reichardt, C. L., Rouble, M., Ruhl, J. E., Schiappucci, E., Smecher, G., Sobrin, J. A., Stark, A. A., Stephen, J., Suzuki, A., Tandoi, C., Thompson, K. L., Thorne, B., Tucker, C., Umilta, C., Vieira, J. D., Wang, G., Whitehorn, N., Wu, W. L. K., Yefremenko, V., Young, M. R., and Zebrowski, J. A. (2023). Measurement of the CMB temperature power spectrum and constraints on cosmology from the SPT-3G 2018 TT, TE, and EE dataset. *Phys. Rev. D*, 108:023510. doi:10.1103/PhysRevD.108.023510. arXiv:2212.06009.

Banik, I. and Kalaitzidis, V. (2025). Testing the local void solution to the Hubble tension using baryon acoustic oscillation measurements over the last twenty years. *Monthly Notices of the Royal Astronomical Society*, 540(1):545–561. doi:10.1093/mnras/staf781. arXiv:2501.17934.

Bartelmann, M. (2022). The Hubble Constant. In *Lecture Notes on Cosmology*, pages 25–37. Heidelberg University. Available at: https://home.strw.leidenuniv.nl/%7Ebouwens/obscosmo/Bartelmann-4.pdf. Chapter 4, version accessed 4 Jul 2025.

Baumann, D. (2022). *Cosmology*. Cambridge University Press. doi:10.1017/9781108937092. ISBN: 9781108937092.

Bautista, J. E., Paviot, R., Vargas Magana, M., de la Torre, S., Fromenteau, S., Gil-Marin, H., Ross, A. J., Burtin, E., Dawson, K. S., Hou, J., Kneib, J.-P., de Mattia, A., Percival, W. J., Rossi, G., Tojeiro, R., Zhao, C., Zhao, G.-B., Alam, S., Brownstein, J., Chapman, M. J., Choi, P. D., Chuang, C.-H., Escoffier, S., de la Macorra, A., du Mas des Bourboux, H., Mohammad, F. G., Moon, J., Mueller, E.-M., Nadathur, S., Newman, J. A., Schneider, D., Seo, H.-J., and Wang, Y. (2021). The Completed SDSS-IV extended Baryon Oscillation Spectroscopic Survey: measurement of the BAO and growth rate of structure of the luminous red galaxy sample from

the anisotropic correlation function between redshifts 0.6 and 1. *Mon. Notes Roy. Astron. Soc.*, 500(3):736–762. doi:10.1093/mnras/staa2800. arXiv:2007.08993.

Beaton, R. L., Freedman, W. L., Madore, B. F., Bono, G., Carlson, E., Clementini, G., Fiorentino, G., Monson, A. J., Rich, J., Scowcroft, V., Seibert, M., Seidel, M., Sturch, L., and Yang, L. (2016). The Carnegie-Chicago Hubble Program. I. An Independent Approach to the Extragalactic Distance Scale Using Only Population II Distance Indicators. *The Astrophysical Journal*, 832(2):210. doi:10.3847/0004-637X/832/2/210. arXiv:1604.01788.

Bernal, J. L., Verde, L., and Riess, A. G. (2016). The trouble with H_0. *Journal of Cosmology and Astroparticle Physics*, (10):019–019. doi:10.1088/1475-7516/2016/10/019. arXiv:1607.05617.

Birrer, S., Buckley-Geer, E. J., Cappellari, M., Courbin, F., Dux, F., Fassnacht, C. D., Frieman, J. A., Galan, A., Gilman, D., Huang, X.-Y., Knabel, S., Langeroodi, D., Lin, H., Millon, M., Morishita, T., Motta, V., Mozumdar, P., Paic, E., Shajib, A. J., Sheu, W., Sluse, D., Sonnenfeld, A., Spiniello, C., Stiavelli, M., Suyu, S. H., Tan, C. Y., Treu, T., de Vyvere, L. V., Wang, H., Wells, P., Williams, D. M., and Wong, K. C. (2025). TDCOSMO 2025: Cosmological Constraints from Strong Lensing Time Delays. *arXiv preprint*. doi:10.48550/arXiv.2506.03023. arXiv:2506.03023.

Birrer, S., Millon, M., Sluse, D., Shajib, A. J., Courbin, F., Koopmans, L. V. E., Suyu, S. H., and Treu, T. (2024). Time-Delay Cosmography: Measuring the Hubble Constant and other cosmological parameters with strong gravitational lensing. *Space Science Reviews*, 220:48. doi:10.1007/s11214-024-01079-w. arXiv:2210.10833.

Blomqvist, M., du Mas des Bourboux, H., Busca, N. G., de Sainte Agathe, V., Rich, J., Balland, C., Bautista, J. E., Dawson, K., Font-Ribera, A., Guy, J., Le Goff, J.-M., Palanque-Delabrouille, N., Percival, W. J., Perez-Rafols, I., Pieri, M. M., Schneider, D. P., Slosar, A., and Yeche, C. (2019). Baryon acoustic oscillations from the cross-correlation of Lyα absorption and quasars in eBOSS DR14. *Astron. Astrophys.*, 629:A86. doi:10.1051/0004-6361/201935641. arXiv:1904.03430.

Borghi, N., Mancarella, M., Moresco, M., Tagliazucchi, M., Iacovelli, F., Cimatti, A., and Maggiore, M. (2024). Cosmology and Astrophysics

with Standard Sirens and Galaxy Catalogs in View of Future Gravitational Wave Observations. *The Astrophysical Journal*, 964(2):191. doi:10.3847/1538-4357/ad20eb. arXiv:2312.05302.

Boubel, P., Colless, M., Said, K., and Staveley-Smith, L. (2024). An Improved Tully-Fisher Estimate of the Hubble Constant. *Monthly Notices of the Royal Astronomical Society*, 533(2):1550–1559. doi:10.1093/mnras/stae1925. arXiv:2408.03660.

Bouwens, R. J. (2024). Distance-Measurement Methods (Lecture Notes 3). Leiden University, Observational Cosmology Course, unpublished.

Breuval, L., Anand, G. S., Anderson, R. I., and et al. (2025). Converging on the Cepheid Metallicity Dependence: Implications of Non-standard *Gaia* Parallax Recalibration on Distance Measures. *arXiv preprint*. doi:10.48550/arXiv.2507.15936. arXiv:2507.15936.

Breuval, L., Riess, A. G., Casertano, S., Yuan, W., Macri, L. M., Romaniello, M., Murakami, Y. S., Scolnic, D., Anand, G. S., and SoszyÅski, I. (2024). Small Magellanic Cloud Cepheids Observed with the Hubble Space Telescope Provide a New Anchor for the SH0ES Distance Ladder. *The Astrophysical Journal*, 973(1):30. doi:10.3847/1538-4357/ad630e. arXiv:2404.08038.

Brout, D., Scolnic, D., Popovic, B., Riess, A. G., Carr, A., Zuntz, J., Kessler, R., Davis, T. M., Hinton, S., Jones, D., Kenworthy, W. D., Peterson, E. R., Said, K., Taylor, G., Ali, N., Armstrong, P., Charvu, P., Dwomoh, A., Meldorf, C., Palmese, A., Qu, H., Rose, B. M., Sanchez, B., Stubbs, C. W., Vincenzi, M., Wood, C. M., Brown, P. J., Chen, R., Chambers, K., Coulter, D. A., Dai, M., Dimitriadis, G., Filippenko, A. V., Foley, R. J., Jha, S. W., Kelsey, L., Kirshner, R. P., Möller, A., Muir, J., Nadathur, S., Pan, Y.-C., Rest, A., Rojas-Bravo, C., Sako, M., Siebert, M. R., Smith, M., Stahl, B. E., and Wiseman, P. (2022). The Pantheon+ Analysis: Cosmological Constraints. *The Astrophysical Journal*, 938(2):110. doi:10.3847/1538-4357/ac8e04. arXiv:2202.04077.

Cai, R.-G., Ding, J.-F., Guo, Z.-K., Wang, S.-J., and Yu, W.-W. (2021). Do the observational data favor a local void? *Physical Review D*, 103(12):123539. doi:10.1103/PhysRevD.103.123539. arXiv:2012.13812.

Cantiello, M. and Blakeslee, J. P. (2023). Surface Brightness Fluctuations. *arXiv e-prints*. doi:10.48550/arXiv.2307.03116. arXiv:2307.03116.

Chávez, R., Terlevich, R., Terlevich, E., González-Morán, A., Fernández-Arenas, D., Bresolin, F., Plionis, M., Basilakos, S., Amorín, R., and Llerena, M. (2025). Mapping the Hubble Flow from $z \sim 0$ to $z \sim 7.5$ with HII Galaxies. *Monthly Notices of the Royal Astronomical Society*, 538(2):1264–1271. doi:10.1093/mnras/staf386. arXiv:2404.16261.

Chávez, R., Terlevich, R., Terlevich, E., Plionis, M., Bresolin, F., Basilakos, S., and Melnick, J. (2014). HII galaxies in the local Universe. I. Sample selection and Hα integrated kinematic properties. *Monthly Notices of the Royal Astronomical Society*, 442(4):3565–3581. doi:10.1093/mnras/stu987. arXiv:1405.4010.

Ciardullo, R. (2022). The Planetary Nebula Luminosity Function in the Era of Precision Cosmology. *Frontiers in Astronomy and Space Sciences*, 9:896326. doi:10.3389/fspas.2022.896326.

de Jaeger, T., Galbany, L., Riess, A. G., Stahl, B. E., Shappee, B. J., Filippenko, A. V., and Zheng, W. (2022). A 5% measurement of the Hubble constant from Type II supernovae. *Monthly Notices of the Royal Astronomical Society*, 514(3):4620–4628. doi:10.1093/mnras/stac1661. arXiv:2203.08974.

de Sainte Agathe, V., Balland, C., du Mas des Bourboux, H., Busca, N. G., Blomqvist, M., Guy, J., Rich, J., Font-Ribera, A., Pieri, M. M., Bautista, J. E., Dawson, K., Le Goff, J.-M., de la Macorra, A., Palanque-Delabrouille, N., Percival, W. J., Perez-Rafols, I., Schneider, D. P., Slosar, A., and Yeche, C. (2019). Baryon acoustic oscillations at z = 2.34 from the correlations of Lyα absorption in eBOSS DR14. *Astron. Astrophys.*, 629:A85. doi:10.1051/0004-6361/201935638. arXiv:1904.03400.

DES Collaboration (2024). The Dark Energy Survey: Cosmology Results With ∼1500 New High-redshift Type Ia Supernovae Using The Full 5-year Dataset. doi:10.3847/2041-8213/ad6f9f. arXiv:2401.02929. For the full list of authors please see the original publication.

DESI Collaboration (2025a). Constraints on Neutrino Physics from DESI DR2 BAO and DR1 Full Shape. *arXiv e-prints*. doi:10.48550/arXiv.2503.14744. arXiv:2503.14744. For the full list of authors please see the original publication.

DESI Collaboration (2025b). DESI 2024 III: Baryon Acoustic Oscillations from Galaxies and Quasars. *Journal of Cosmology and Astroparticle*

Physics, 04:012. doi:10.1088/1475-7516/2025/04/012. arXiv:2404.03000. For the full list of authors please see the original publication.

DESI Collaboration (2025c). DESI 2024 VI: Cosmological Constraints from the Measurements of Baryon Acoustic Oscillations. *Journal of Cosmology and Astroparticle Physics*, 02:021. doi:10.1088/1475-7516/2025/02/021. arXiv:2404.03002. For the full list of authors please see the original publication.

DESI Collaboration (2025d). DESI DR2 Results II: Measurements of Baryon Acoustic Oscillations and Cosmological Constraints. doi:10.48550/arXiv.2503.14738. arXiv:2503.14738. For the full list of authors please see the original publi- cation.

Di Valentino, E., Mena, O., Pan, S., Visinelli, L., Yang, W., Melchiorri, A., Mota, D. F., Riess, A. G., and Silk, J. (2021). In the realm of the Hubble tension — a review of solutions. *Classical and Quantum Gravity*, 38(15):153001. doi:10.1088/1361-6382/ac086d. arXiv:2103.01183.

Di Valentino, E., Said, J. L., Riess, A., Pollo, A., Poulin, V., Gómez-Valent, A., Weltman, A., Palmese, A., Huang, C. D., van de Bruck, C., Saraf, C. S., Kuo, C.-Y., Uhlemann, C., Grandón, D., Paz, D., Eckert, D., Teixeira, E. M., Saridakis, E. N., Ó Colgáin, E., Beutler, F., Niedermann, F., Bajardi, F., Barenboim, G., Gubitosi, G., Musella, I., Banik, I., Szapudi, I., Singal, J., Haro Cases, J., Chluba, J., Torrado, J., Mifsud, J., Jedamzik, K., Said, K., Dialektopoulos, K., Herold, L., Perivolaropoulos, L., Zu, L., Galbany, L., Breuval, L., Visinelli, L., Kadam, L. A., et al. (2025). The CosmoVerse White Paper: Addressing Observational Tensions in Cosmology with Systematics and Fundamental Physics. *Physics of the Dark Universe*, 49:101965. doi:10.1016/j.dark.2025.101965. arXiv:2504.01669.

Dodelson, S. and Schmidt, F. (2020). *Modern Cosmology*. Academic Press. doi:10.1016/C2017-0-01943-2. Second Edition; eBook ISBN 978-0-12-815949-1.

Domínguez, A., Kirkeberg, P. O., Wojtak, R., Saldana-Lopez, A., Desai, A., Primack, J. R., Finke, J., Ajello, M., Pérez-González, P. G., Paliya, V. S., and Hartmann, D. (2024). A New Derivation of the Hubble Constant from γ-Ray Attenuation Using Improved Optical Depths for the Fermi and CTA Era. *Monthly Notices of the Royal Astronomical Society*, 527(3):4632–4642. doi:10.1093/mnras/stad3425. arXiv:2306.09878.

Domínguez, A., Wojtak, R., Finke, J. D., Ajello, M., Helgason, K., Prada, F., Desai, A., Paliya, V. S., Marcotulli, L., and Hartmann, D. H. (2019). A New Measurement of the Hubble Constant and Matter Content of the Universe Using Extragalactic Background Light γ-Ray Attenuation. *The Astrophysical Journal*, 885(2):137. doi:10.3847/1538-4357/ab4a0e. arXiv:1903.12097.

Efstathiou, G. (2021). To H0 or not to H0? *Monthly Notices of the Royal Astronomical Society*, 505(3):3866–3872. doi:10.1093/mnras/stab1588. arXiv:2103.08723.

Efstathiou, G. (2025). Evolving Dark Energy or Supernovae Systematics? *Monthly Notices of the Royal Astronomical Society*, 538(2):875–882. doi:10.1093/mnras/staf301. arXiv:2408.07175.

Efstathiou, G. and Gratton, S. (2021). A Detailed Description of the CamSpec Likelihood Pipeline and a Reanalysis of the Planck High Frequency Maps. *The Open Journal of Astrophysics*, 4. doi:10.21105/astro.1910.00483. arXiv:1910.00483.

Ellis, G. F. R., Maartens, R., and MacCallum, M. A. H. (2012). *Relativistic Cosmology*. Cambridge University Press. doi:10.1017/CBO9781139014403. online ISBN: 9781139014403.

Etherington, I. M. H. (1933). Republication of: LX. On the definition of distance in general relativity. *General Relativity and Gravitation*, 39(7):1055–1067. doi:10.1007/s10714-007-0447-x.

Ezquiaga, J. M. and Holz, D. E. (2022). Spectral Sirens: Cosmology from the Full Mass Distribution of Compact Binaries. *Physical Review Letters*, 129(6):061102. doi:10.1103/PhysRevLett.129.061102. arXiv:2202.08240.

Falco, E. E., Gorenstein, M. V., and Shapiro, I. I. (1985). On model-dependent bounds on H_0 from gravitational images. *The Astrophysical Journal*, 289:L1–L4. doi:10.1086/184422.

Farr, W. M., Fishbach, M., Ye, J., and Holz, D. E. (2019). A Future Percent-level Measurement of the Hubble Expansion at Redshift 0.8 with Advanced LIGO. *The Astrophysical Journal Letters*, 883(2):L42. doi:10.3847/2041-8213/ab4284. arXiv:1908.09084.

Favale, A., Gómez-Valent, A., and Migliaccio, M. (2023). Cosmic chronometers to calibrate the ladders and measure the curvature of the Universe. A

model-independent study. *Monthly Notices of the Royal Astronomical Society*, 523(3):3406–3422. doi:10.1093/mnras/stad1621. arXiv:2301.09591.

Freedman, W. L. and Madore, B. F. (2010). The Hubble Constant. *Annual Review of Astronomy and Astrophysics*, 48:673–710. doi:10.1146/annurev-astro-082708-101829. arXiv:1004.1856.

Freedman, W. L. and Madore, B. F. (2023). Progress in Direct Measurements of the Hubble Constant. *Journal of Cosmology and Astroparticle Physics*, 2023(11):050. doi:10.1088/1475-7516/2023/11/050. arXiv:2309.05618.

Freedman, W. L., Madore, B. F., Hoyt, T. J., Jang, I. S., Beaton, R. L., Lee, M. G., Monson, A. J., Neeley, J. R., and Rich, J. (2019). The Carnegie-Chicago Hubble Program. VIII. An Independent Determination of the Hubble Constant Based on the Tip of the Red Giant Branch. *The Astrophysical Journal*, 882(1):34. doi:10.3847/1538-4357/ab2f73. arXiv:1907.05922.

Freedman, W. L., Madore, B. F., Jang, I. S., Hoyt, T. J., Lee, A. J., and Owens, K. A. (2025). Status Report on the Chicago-Carnegie Hubble Program (CCHP): Three Independent Astrophysical Determinations of the Hubble Constant Using the James Webb Space Telescope. *The Astrophysical Journal*, 985(2):203. doi:10.3847/1538-4357/acee25. arXiv:2408.06153.

Garny, M., Niedermann, F., Rubira, H., and Sloth, M. S. (2025). Hot New Early Dark Energy: Dark Radiation Matter Decoupling. *arXiv e-prints*. doi:10.48550/arXiv.2508.03795. arXiv:2508.03795.

Ge, F., Millea, M., Camphuis, E., Daley, C., Huang, N., Omori, Y., Quan, W., Anderes, E., Anderson, A. J., Ansarinejad, B., Archipley, M., Balkenhol, L., Benabed, K., Bender, A. N., Benson, B. A., Bianchini, F., Bleem, L. E., Bouchet, F. R., Bryant, L., Carlstrom, J. E., Chang, C. L., Chaubal, P., Chen, G., Chichura, P. M., Chokshi, A., Chou, T.-L., Coerver, A., Crawford, T. M., de Haan, T., Dibert, K. R., Dobbs, M. A., Doohan, M., Doussot, A., Dutcher, D., Everett, W., Feng, C., Ferguson, K. R., Fichman, K., Foster, A., Galli, S., Gambrel, A. E., Gardner, R. W., Goeckner-Wald, N., Gualtieri, R., Guidi, F., Guns, S., Halverson, N. W., Hivon, E., Holder, G. P., Holzapfel, W. L., Hood, J. C., Howe, D., Hryciuk, A., Kéruzoré, F., Khalife, A. R., Knox, L., Korman, M., Kornoelje, K., Kuo, C.-L., Lee, A. T., Levy, K., Lowitz, A. E., Lu, C., Maniyar, A., Martsen, E. S., Menanteau, F., Montgomery, J., Nakato, Y., Natoli, T., Noble, G. I., Pan, Z., Paschos, P., Phadke, K. A., Pollak, A. W., Prabhu, K., Rahimi, M., Rahlin, A., Reichardt, C. L., Riebel, D., Rouble, M., Ruhl,

J. E., Schiappucci, E., Sobrin, J. A., Stark, A. A., Stephen, J., Tandoi, C., Thorne, B., Trendafilova, C., Umiltà, C., Vieira, J. D., Vitrier, A., Wan, Y., Whitehorn, N., Wu, W. L. K., Young, M. R., and Zebrowski, J. A. (2025). Cosmology From CMB Lensing and Delensed EE Power Spectra Using 2019–2020 SPT-3G Polarization Data. *Physical Review D*, 111(8):083534. doi:10.1103/PhysRevD.111.083534. arXiv:2411.06000.

Gieren, W., Storm, J., Konorski, P., Górski, M., Pilecki, B., Thompson, I., Pietrzyński, G., Graczyk, D., Barnes, T. G., Fouqué, P., Nardetto, N., Gallenne, A., Karczmarek, P., Suchomska, K., Wielgórski, P., Taormina, M., and Zgirski, B. (2018). The effect of metallicity on Cepheid period–luminosity relations from a Baade–Wesselink analysis of Cepheids in the Milky Way and Magellanic Clouds. *Astronomy & Astrophysics*, 620:A99. doi:10.1051/0004-6361/201833263. arXiv:1809.04073.

Gödel, K. (1947). An Example of a New Type of Cosmological Solutions of Einstein's Field Equations of Gravitation. *Reviews of Modern Physics*, 21(3):447–450. doi:10.1103/RevModPhys.21.447.

Gómez-Valent, A. (2022). A Fast Test to Assess the Impact of Marginalization in Monte Carlo Analyses, and Its Application to Cosmology. *Physical Review D*, 106(6):063506. doi:10.1103/PhysRevD.106.063506. arXiv:2203.16285.

Gómez-Valent, A., Favale, A., Migliaccio, M., and Sen, A. A. (2024). Late-time phenomenology required to solve the $\mathbf{H_0}$ tension in view of the cosmic ladders and the anisotropic and angular BAO data sets. *Physical Review D*, 109(2):023525. doi:10.1103/PhysRevD.109.023525. arXiv:2309.07795.

Graves, G. J., Faber, S. M., and Schiavon, R. P. (2009). Dissecting the Red Sequence. II. Stellar Population Properties as a Function of Velocity Dispersion and Residual Star Formation. *The Astrophysical Journal*, 698(2):1590–1610. doi:10.1088/0004-637X/698/2/1590. arXiv:0903.3603.

Gray, R. e. a. (2020). Cosmological Inference Using Gravitational-Wave Standard Sirens: A Mock Data Analysis. *Physical Review D*, 101:122001. doi:10.1103/PhysRevD.101.122001. arXiv:1908.06050.

Guo, W., Wang, Q., Cao, S., Biesiada, M., Liu, T., Lian, Y., Jiang, X., Mu, C., and Cheng, D. (2025). Newest measurements of Hubble constant from DESI 2024 BAO observations. *The Astrophysical Journal Letters*, 978(2):L33. doi:10.3847/2041-8213/ada37f. arXiv:2412.13045.

Haridasu, B. S., Salucci, P., and Sharma, G. (2024). Radial Tully-Fisher relation and the local variance of the Hubble parameter. *Monthly Notices of the Royal Astronomical Society*, 532(2):2234–2247. doi:10.1093/mnras/stae1467. arXiv:2403.06859.

Haslbauer, M., Banik, I., and Kroupa, P. (2020). The KBC Void and Hubble Tension Contradict ΛCDM on a Gpc Scale-Milgromian Dynamics as a Possible Solution. *Monthly Notices of the Royal Astronomical Society*, 499(2):2845–2883. doi:10.1093/mnras/staa2348. arXiv:2009.11292.

Heavens, A., Jimenez, R., and Verde, L. (2014). Standard rulers, candles, and clocks from the low-redshift Universe. *Physical Review Letters*, 113(24):241302. doi:10.1103/PhysRevLett.113.241302. arXiv:1409.6217.

Hill, J. C., Aiola, S., Choi, S. K., and et al. (2025). The Atacama Cosmology Telescope: DR6 Power Spectra, Likelihoods and ΛCDM Parameters. *arXiv preprint*. doi:10.48550/arXiv.2503.14452. arXiv:2503.14452. Matching version accepted by JCAP.

Hogg, D. W. (2000). Distance measures in cosmology. *arXiv e-print*. doi:10.48550/arXiv.astro-ph/9905116. arXiv:astro-ph/9905116.

Huang, C. D., Riess, A. G., Yuan, W., Macri, L. M., Zakamska, N. L., Casertano, S., Whitelock, P. A., Hoffmann, S. L., Filippenko, A. V., and Scolnic, D. (2020). Hubble Space Telescope Observations of Mira Variables in the Type Ia Supernova Host NGC 1559: An Alternative Candle to Measure the Hubble Constant. *The Astrophysical Journal*, 889(1). doi:10.3847/1538-4357/ab5dbd. arXiv:1908.10883.

Huang, C. D., Yuan, W., Riess, A. G., Hack, W., Whitelock, P. A., Zakamska, N. L., Casertano, S., Macri, L. M., Marengo, M., Menzies, J. W., and Smith, R. K. (2024). The Mira Distance to M101 and a 4% Measurement of H_0. *The Astrophysical Journal*, 963(2):83. doi:10.3847/1538-4357/ad1ff8. arXiv:2401.09581.

Hubble, E. (1929). A Relation between Distance and Radial Velocity among Extra-Galactic Nebulae. *Proceedings of the National Academy of Sciences*, 15(3):168–173. doi:10.1073/pnas.15.3.168.

Humphreys, E. M. L., Reid, M. J., Moran, J. M., Greenhill, L. J., and Argon, A. L. (2013). Toward a New Geometric Distance to NGC 4258. III. Final Results and the Hubble Constant. *The Astrophysical Journal*, 775(1):13. doi:10.1088/0004-637X/775/1/13. arXiv:1307.6031.

Hwang, S.-g., L'Huillier, B., Keeley, R. E., Jee, M. J., and Shafieloo, A. (2023). How to use GP: Effects of the mean function and hyperparameter selection on Gaussian Process regression. *Journal of Cosmology and Astroparticle Physics*, 2023(02):014. doi:10.1088/1475-7516/2023/02/014. arXiv:2206.15081.

Jedamzik, K. and Pogosian, L. (2020). Relieving the Hubble tension with primordial magnetic fields. *Phys. Rev. Lett.*, 125:181302. doi:10.1103/PhysRevLett.125.181302. arXiv:2004.09487.

Jedamzik, K., Pogosian, L., and Zhao, G.-B. (2021). Why Reducing the Cosmic Sound Horizon Alone Cannot Fully Resolve the Hubble Tension. *Nature*, 4:123. doi:10.1038/s42005-021-00628-x. arXiv:2010.04158.

Jensen, J. B., Blakeslee, J. P., Cantiello, M., Cowles, M., Anand, G. S., Tully, R. B., Kourkchi, E., and Raimondo, G. (2025). The TRGB-SBF Project. III. Refining the HST Surface Brightness Fluctuation Distance Scale Calibration with JWST. *The Astrophysical Journal*, in press. doi:10.3847/1538-4357/addfd6. arXiv:2407.06850.

Jimenez, R. and Loeb, A. (2002). Constraining Cosmological Parameters Based on Relative Galaxy Ages. *The Astrophysical Journal*, 573(1):37–42. doi:10.1086/340549. arXiv:astro-ph/0106145.

Jimenez, R., Moresco, M., Verde, L., and Wandelt, B. D. (2023). Cosmic Chronometers with Photometry: A New Path to $H(z)$. *Journal of Cosmology and Astroparticle Physics*, 2023(11):047. doi:10.1088/1475-7516/2023/11/047. arXiv:2306.11425.

Jimenez, R., Verde, L., Treu, T., and Stern, D. (2003). Constraints on the equation of state of dark energy and the hubble constant from stellar ages and the CMB. *The Astrophysical Journal*, 593:622–629. doi:10.1086/376595. arXiv:astro-ph/0302560.

Keenan, R. C., Barger, A. J., and Cowie, L. L. (2013). Evidence for a ~ 300 Mpc scale underdensity in the local galaxy distribution. *Astrophysical Journal*, 775(1):62. doi:10.1088/0004-637X/775/1/62. arXiv:1304.2884.

Kenworthy, W. D., Jones, D. O., Dai, M., Kessler, R., Scolnic, D., Brout, D., Siebert, M. R., Pierel, J. D. R., Foley, R. J., Jha, S. W., and (2021). SALT3: An Improved Type Ia Supernova Model for Measuring Cosmic Distances. *The Astrophysical Journal*, 923(2):265. doi:10.3847/1538-4357/ac30d8. arXiv:2104.07795.

Kenworthy, W. D., Scolnic, D., and Riess, A. (2019). The Local Perspective on the Hubble Tension: Local Structure Does Not Impact Measurement of the Hubble Constant. *The Astrophysical Journal*, 875(2):145. doi:10.3847/1538-4357/ab0ebf. arXiv:1901.08681.

Kessler, R., Brout, D., D'Andrea, C. B., Davis, T. M., Hinton, S. R., Kim, A. G., Lasker, J., Lidman, C., Macaulay, E., Möller, A., Sako, M., Scolnic, D., Smith, M., Sullivan, M., Zhang, B., and et al. (2019). First Cosmology Results Using Type Ia Supernova from the Dark Energy Survey: Simulations to Correct Supernova Distance Biases. *Monthly Notices of the Royal Astronomical Society*, 485(1):1171–1187. doi:10.1093/mnras/stz463. arXiv:1811.02379.

Knox, L. and Millea, M. (2020). Hubble constant hunter's guide. *Physical Review D*, 101:043533. doi:10.1103/PhysRevD.101.043533. arXiv:1908.03663.

Kochanek, C. S. (2002). What Do Gravitational-Lens Time Delays Measure? *The Astrophysical Journal*, 578:25–32. doi:10.1086/342476. arXiv:0205319.

Krolewski, A., Percival, W. J., and Woodfinden, A. (2025). A new method to determine H_0 from cosmological energy-density measurements. *Physical Review Letters*, 134(10):101002. doi:10.1103/PhysRevLett.134.101002. arXiv:2403.19227.

Leavitt, H. S. and Pickering, E. C. (1912). Periods of 25 variable stars in the small magellanic cloud. *Harvard College Observatory Circular*, 173:1–3.

Lemaître, G. (1927). Un univers homogène de masse constante et de rayon croissant rendant compte de la vitesse radiale des nébuleuses extragalactiques. *Annales de la Société Scientifique de Bruxelles*, A47:49–59. English translation in Monthly Notices of the Royal Astronomical Society, 91:483–490 (1931).

LIGO and Virgo Collaboration (2017). A gravitational-wave standard siren measurement of the Hubble constant. *Nature*, 551:85–88. doi:10.1038/nature24471. arXiv:1710.05835. For the full list of authors please see the original publication.

LIGO and VIRGO Collaboration (2021). A Gravitational-wave Measurement of the Hubble Constant Following the Second Observing Run of Advanced LIGO and Virgo. *The Astrophysical Journal*, 909(2):218. doi:10.3847/1538-4357/abdcb7. arXiv:1908.06060. For the full list of authors please see the original publication.

LIGO and Virgo Collaboration (2019). GWTC-1: A Gravitational-Wave Transient Catalog of Compact Binary Mergers Observed by LIGO and Virgo during the First and Second Observing Runs. *Physical Review X*, 9(3):031040. doi:10.1103/PhysRevX.9.031040. arXiv:1811.12907. For the full list of authors please see the original publication.

Lindegren, L., Bastian, U., and Biermann, M. e. a. (2021). Gaia early data release 3: Parallax bias versus magnitude, colour and position. *Astronomy & Astrophysics*, 649:A4. doi:10.1051/0004-6361/202039653. arXiv:2012.01742.

Liu, T., Cao, S., and Wang, J. (2025). A model-independent determination of the sound horizon using recent BAO measurements and strong lensing systems. *Physical Review D*, 111(2):023524. doi:10.1103/PhysRevD.111.023524. arXiv:2406.18298.

Louis, T., Posta, A. L., Atkins, Z., Jense, H. T., Abril-Cabezas, I., Addison, G. E., Ade, P. A. R., Aiola, S., Alford, T., Alonso, D., Amiri, M., An, R., Austermann, J. E., Barbavara, E., Battaglia, N., Battistelli, E. S., Beall, J. A., Bean, R., Beheshti, A., Beringue, B., Bhandarkar, T., Biermann, E., Bolliet, B., Bond, J. R., Calabrese, E., Capalbo, V., Carrero, F., Chen, S.-F., Chesmore, G., mei Cho, H., Choi, S. K., Clark, S. E., Cothard, N. F., Coughlin, K., Coulton, W., Crichton, D., Crowley, K. T., Darwish, O., Devlin, M. J., Dicker, S., Duell, C. J., Duff, S. M., Duivenvoorden, A. J., Dunkley, J., Dünner, R., Villagra, C. E., Fankhanel, M., Farren, G. S., Ferraro, S., Foster, A., Freundt, R., Fuzia, B., Gallardo, P. A., Garrido, X., Gerbino, M., Giardiello, S., Gill, A., Givans, J., Gluscevic, V., Goldstein, S., Golec, J. E., Gong, Y., Guan, Y., Halpern, M., Harrison, I., Hasselfield, M., Healy, E., Henderson, S., Hensley, B., Hervías-Caimapo, C., Hill, J. C., Hilton, G. C., Hilton, M., Hincks, A. D., Hložek, R., Ho, S.-P. P., Hood, J., Hornecker, E., Huber, Z. B., Hubmayr, J., Huffenberger, K. M., Hughes, J. P., Ikape, M., Irwin, K., Isopi, G., Joshi, N., Keller, B., Kim, J., Knowles, K., Koopman, B. J., Kosowsky, A., Kramer, D., Kusiak, A., Lague, A., Lakey, V., Lee, E., Li, Y., Li, Z., Limon, M., Lokken, M., and et al. (2025). The Atacama Cosmology Telescope: DR6 Power Spectra, Likelihoods and ΛCDM Parameters. *arXiv preprint*. doi:10.48550/arXiv.2503.14452. arXiv:2503.14452. Matching version accepted by JCAP.

Luković, V. V., Haridasu, B. S., and Vittorio, N. (2020). Exploring the evidence for a large local void with supernovae Ia data.

Monthly Notices of the Royal Astronomical Society, 491(2):2075–2087. doi:10.1093/mnras/stz3070. arXiv:1907.11219.

Madore, B. F., Freedman, W. L., and Owens, K. (2025). Chicago-Carnegie Hubble Program: Multiwavelength Search for the Effects of Metallicity on the Cepheid Distance Scale. II. Theoretical Models and Synthetic Spectra. *Astrophysical Journal*, 981(1):32. doi:10.3847/1538-4357/ada3d5. arXiv:2506.01188.

Madore, B. F., Mager, V., and Freedman, W. L. (2009). Sharpening the Tip of the Red Giant Branch. *The Astrophysical Journal*, 690(1):389–395. doi:10.1088/0004-637X/690/1/389. arXiv:0809.2598.

McDonough, E., Hill, J. C., Ivanov, M. M., Posta, A. L., and Toomey, M. W. (2024). Observational constraints on early dark energy. *International Journal of Modern Physics D*, 33(11):2430003. doi:10.1142/S0218271824300039. arXiv:2310.19899.

McVittie, G. C. (1933). The Mass-Particle in an Expanding Universe. *Monthly Notices of the Royal Astronomical Society*, 93(5):325–339. doi:10.1093/mnras/93.5.325.

Mirpoorian, S. H., Jedamzik, K., and Pogosian, L. (2025). Modified recombination and the Hubble tension. *Physical Review D*, 111(8):083519. doi:10.1103/PhysRevD.111.083519. arXiv:2411.16678.

Moresco, M. (2015). Raising the Bar: New Constraints on the Hubble Parameter with Cosmic Chronometers at $z \sim 2$. *Monthly Notices of the Royal Astronomical Society: Letters*, 450(1):L16–L20. doi:10.1093/mnrasl/slv037. arXiv:1503.01116.

Moresco, M. (2023). Addressing the Hubble tension with Cosmic Chronometers. *arXiv e-print*. doi:10.48550/arXiv.2307.09501. arXiv:2307.09501.

Moresco, M., Amati, L., Amendola, L., Birrer, S., Blakeslee, J. P., Cantiello, M., Cimatti, A., Darling, J., Della Valle, M., Fishbach, M., Grillo, C., Hamaus, N., Holz, D., Izzo, L., Jimenez, R., Lusso, E., Meneghetti, M., Piedipalumbo, E., Pisani, A., Pourtsidou, A., Pozzetti, L., Quartin, M., Risaliti, G., Rosati, P., and Verde, L. (2022). Unveiling the Universe with emerging cosmological probes. *Living Reviews in Relativity*, 25(1):6. doi:10.1007/s41114-022-00040-z. arXiv:2201.07241.

Moresco, M., Cimatti, A., Jimenez, R., Pozzetti, L., Zamorani, G., Bolzonella, M., Dunlop, J., Lamareille, F., Mignoli, M., Pearce, H., Rosati,

P., Stern, D., Verde, L., Zucca, E., Carollo, C. M., Contini, T., Kneib, J.-P., Le Fèvre, O., Lilly, S. J., Mainieri, V., Renzini, A., Scodeggio, M., Balestra, I., Gobat, R., McLure, R., Bardelli, S., Bongiorno, A., Caputi, K., Cucciati, O., de la Torre, S., de Ravel, L., Franzetti, P., Garilli, B., Iovino, A., Kampczyk, P., Knobel, C., Kovač, K., Le Borgne, J.-F., Le Brun, V., Maier, C., Pelló, R., Peng, Y., Pérez-Montero, E., Presotto, V., Silverman, J. D., Tanaka, M., Tasca, L. A. M., Tresse, L., Vergani, D., Almaini, O., Barnes, L., Bordoloi, R., Bradshaw, E., Cappi, A., Chuter, R., Cirasuolo, M., Coppa, G., Diener, C., Foucaud, S., Hartley, W., Kamionkowski, M., Koekemoer, A. M., López-Sanjuán, C., McCracken, H. J., Nair, P., Oesch, P., Stanford, A., and Welikala, N. (2012). Improved Constraints on the Expansion Rate of the Universe up to $z \sim 1.1$ from the Spectroscopic Evolution of Cosmic Chronometers. *Journal of Cosmology and Astroparticle Physics*, 2012(08):006. doi:10.1088/1475-7516/2012/08/006. arXiv:1201.3609.

Moresco, M., Jimenez, R., Verde, L., Cimatti, A., and Pozzetti, L. (2020a). Setting the Stage for Cosmic Chronometers. II. Impact of Stellar Population Synthesis Models Systematics and Full Covariance Matrix. *The Astrophysical Journal*, 898(1):82. doi:10.3847/1538-4357/ab9eb0. arXiv:2003.07362.

Moresco, M., Jimenez, R., Verde, L., Cimatti, A., and Pozzetti, L. (2020b). Setting the Stage for Cosmic Chronometers. II. Impact of Stellar Population Synthesis Models Systematics and Full Covariance Matrix. *The Astrophysical Journal*, 898(1):82. doi:10.3847/1538-4357/ab9eb0. arXiv:2003.07362.

Moresco, M., Jimenez, R., Verde, L., Pozzetti, L., Cimatti, A., and Citro, A. (2018). Setting the Stage for Cosmic Chronometers. I. Assessing the Impact of Young Stellar Populations on Hubble Parameter Measurements. *The Astrophysical Journal*, 868(2):84. doi:10.3847/1538-4357/aae829. arXiv:1804.05864.

Moresco, M., Pozzetti, L., Cimatti, A., Jimenez, R., Maraston, C., Verde, L., Thomas, D., Citro, A., Tojeiro, R., and Wilkinson, D. (2016). A 6% Measurement of the Hubble Parameter at $z \sim 0.45$: Direct Evidence of the Epoch of Cosmic Re-acceleration. *Journal of Cosmology and Astroparticle Physics*, 2016(05):014. doi:10.1088/1475-7516/2016/05/014. arXiv:1601.01701.

Neveux, R., Burtin, E., de Mattia, A., Smith, A., Ross, A. J., Hou, J., Bautista, J. E., Brinkmann, J., Chuang, C.-H., Dawson, K. S., Gil-Marin,

H., Lyke, B. W., de la Macorra, A., du Mas des Bourboux, H., Mohammad, F. G., Mueller, E.-M., Myers, A. D., Newman, J. A., Percival, W. J., Rossi, G., Schneider, D., Vivek, M., Zarrouk, P., Zhao, C., and Zhao, G.-B. (2021). The Completed SDSS-IV extended Baryon Oscillation Spectroscopic Survey: BAO and RSD measurements from the anisotropic power spectrum of the Quasar sample between redshift 0.8 and 2.2. *Mon. Not. Roy. Astron. Soc.*, 500(2):210–229. doi:10.1093/mnras/staa2780. arXiv:2007.08999.

Niedermann, F. and Sloth, M. S. (2021). New Early Dark Energy. *Phys. Rev. D*, 103(4):L041303. doi:10.1103/PhysRevD.103.L041303. arXiv:1910.10739.

Palmese, A., Kaur, R., Hajela, A., Margutti, R., McDowell, A., and MacFadyen, A. (2024). A Standard Siren Measurement of the Hubble Constant Using GW170817 and the Latest Observations of the Electromagnetic Counterpart Afterglow. *Physical Review D*, 109(6):063508. doi:10.1103/PhysRevD.109.063508. arXiv:2305.19914.

Perivolaropoulos, L. (2024). Hubble Tension or Distance Ladder Crisis? *Physical Review D*, 110:123518. doi:10.1103/PhysRevD.110.123518. arXiv:2408.11031.

Pesce, D. W. and et al. (2020). The Megamaser Cosmology Project. XIII. Combined Hubble Constant Constraints. *The Astrophysical Journal*, 891(2):L1. doi:10.3847/2041-8213/ab75f0. arXiv:2001.09213.

Philcox, O. H. E., Farren, G. S., Sherwin, B. D., and Baxter, E. J. (2022). Determining the Hubble Constant without the Sound Horizon: A 3.6% Constraint on H_0 from Galaxy Surveys, CMB Lensing and Supernovae. *Physical Review D*, 106:063530. doi:10.1103/PhysRevD.106.063530. arXiv:2204.02984.

Philcox, O. H. E. and Ivanov, M. M. (2022). The BOSS DR12 Full-Shape Cosmology: ΛCDM Constraints from the Large-Scale Galaxy Power Spectrum and Bispectrum Monopole. *Physical Review D*, 105(4):043517. doi:10.1103/PhysRevD.105.043517. arXiv:2112.04515.

Phillips, M. M. (1993). The Absolute Magnitudes of Type IA Supernovae. *Astrophysical Journal Letters*, 413:L105–L108. doi:10.1086/186970.

Pietrzyński, G., Graczyk, D., Gallenne, A., Gieren, W., Thompson, I. B., and et al. (2019). A Distance to the Large Magellanic Cloud That Is Precise to One Per Cent. *Nature*, 567(7747):200–203. doi:10.1038/s41586-019-0999-4.

Planck Collaboration (2018). Planck 2018 results. VI. Cosmological parameters. *Astronomy & Astrophysics*, 641:A6. doi:10.1051/0004-6361/201833910. arXiv:1807.06209. For the full list of authors please see the original publication.

Pogosian, L., Zhao, G.-B., and Jedamzik, K. (2024). A Consistency Test of the Cosmological Model at the Epoch of Recombination Using DESI BAO and Planck Measurements. *arXiv pre-print*. doi:10.48550/arXiv.2405.20306. arXiv:2405.20306.

Poulin, V., Smith, T. L., and Karwal, T. (2023). The Ups and Downs of Early Dark Energy solutions to the Hubble tension: A review of models, hints and constraints circa 2023. *Physics of the Dark Universe*, 42:101348. doi:10.1016/j.dark.2023.101348. arXiv:2302.09032.

Poulin, V., Smith, T. L., Karwal, T., and Kamionkowski, M. (2019). Early dark energy can resolve the Hubble tension. *Physical Review Letters*, 122:221301. doi:10.1103/PhysRevLett.122.221301. arXiv:1811.04083.

Rasmussen, C. E. and Williams, C. K. I. (2005). *Gaussian Processes for Machine Learning*. The MIT Press. doi:10.7551/mitpress/3206.001.0001. ISBN: 978-0-262-25683-4.

Ratsimbazafy, A. L., Loubser, S. I., Crawford, S. M., Cress, C. M., Bassett, B. A., Nichol, R. C., and Väisänen, P. (2017). Age-dating Luminous Red Galaxies observed with the Southern African Large Telescope. *Monthly Notices of the Royal Astronomical Society*, 467(3):3239–3254. doi:10.1093/mnras/stx301. arXiv:1702.00418.

Reese, E. D. (2004). Measuring the Hubble Constant with the Sunyaev-Zel'dovich Effect. In Freedman, W. L., editor, *Measuring and Modeling the Universe*, volume 2 of *Carnegie Observatories Astrophysics Series*. Cambridge University Press. doi:10.48550/arXiv.astro-ph/0306073. arXiv:astro-ph/0306073.

Refsdal, S. (1964). On the possibility of determining Hubble's parameter and the masses of galaxies from the gravitational lens effect. *Monthly Notices of the Royal Astronomical Society*, 128:307–310. doi:10.1093/mnras/128.4.307.

Reid, M. J., Pesce, D. W., and Riess, A. G. (2019). An improved distance to ngc 4258 and its implications for the hubble constant. *Astrophysical Journal*, 885:8. doi:10.3847/1538-4357/ab4a11.

Renzi, F., Hogg, N. B., and Giaré, W. (2022). The resilience of the Etherington-Hubble relation. *Monthly Notices of the Royal Astronomical Society*, 513(3):4004–4014. doi:10.1093/mnras/stac1030. arXiv:2112.05701.

Renzi, F. and Silvestri, A. (2023). A look at the Hubble speed from first principles. *Physical Review D*, 107(2):023520. doi:10.1103/PhysRevD.107.023520. arXiv:2011.10559.

Riess, A. G., Casertano, S., Yuan, W., Anderson, R. I., Macri, L. M., and Scolnic, D. (2021). Cosmic Distances Calibrated to 1% Precision with *Gaia* EDR3 Parallaxes of Milky Way Cepheids. *The Astrophysical Journal Letters*, 908(1):L6. doi:10.3847/2041-8213/abdbaf. arXiv:2012.08534.

Riess, A. G., Macri, L. M., Hoffmann, S. L., Scolnic, D., Casertano, S., Filippenko, A. V., Tucker, B. E., Reid, M. J., Jones, D. O., Silverman, J. M., Chornock, R., Challis, P., Yuan, W., Brown, P. J., and Foley, R. J. (2016). A 2.4% Determination of the Local Value of the Hubble Constant. *The Astrophysical Journal*, 826(1):56. doi:10.3847/0004-637X/826/1/56. arXiv:1604.01424.

Riess, A. G., Scolnic, D., Anand, G. S., Breuval, L., Casertano, S., Macri, L. M., Yuan, W., and et al. (2024). JWST Validates HST Distance Measurements: Selection of Supernova Subsample Explains Differences in JWST Estimates of Local H_0. *The Astrophysical Journal*, 977(1):120. doi:10.3847/1538-4357/ad8c21. arXiv:2408.11770.

Riess, A. G., Yuan, W., Macri, L. M., Scolnic, D., Brout, D., Casertano, S., Jones, D. O., Murakami, Y., Breuval, L., Brink, T. G., Filippenko, A. V., Hoffmann, S., Jha, S. W., Kenworthy, W. D., Anand, G., Mackenty, J., Stahl, B. E., and Zheng, W. (2022). A Comprehensive Measurement of the Local Value of the Hubble Constant with 1 km/s/Mpc Uncertainty from the Hubble Space Telescope and the SH0ES Team. *The Astrophysical Journal Letters*, 934(1):L7. doi:10.3847/2041-8213/ac5c5b. arXiv:2112.04510.

Sah, A., Rameez, M., Sarkar, S., and Tsagas, C. (2025). Anisotropy in Pantheon+ supernovae. *European Physical Journal C*, 85:596. doi:10.1140/epjc/s10052-025-14222-w. arXiv:2411.10838.

Said, K., Howlett, C., Davis, T., Lucey, J., Saulder, C., Douglass, K., Kim, A. G., Kremin, A., Ross, C., Aldering, G., Aguilar, J. N., Ahlen, S., Ben-Zvi, S., Bianchi, D., Brooks, D., Claybaugh, T., Dawson, K., de la Macorra,

A., Dey, B., Doel, P., Fanning, K., Ferraro, S., Font-Ribera, A., Forero-Romero, J. E., Gaztañaga, E., Gontcho, S. G. A., Guy, J., Honscheid, K., Kehoe, R., Kisner, T., Lambert, A., Landriau, M., Guillou, L. L., Manera, M., Meisner, A., Miquel, R., Moustakas, J., Muñoz-Gutiérrez, A., Myers, A., Nie, J., Palanque-Delabrouille, N., Percival, W., Prada, F., Rossi, G., Sánchez, E., Schlegel, D., Schubnell, M., Silber, J. H., Sprayberry, D., Tarlé, G., Magaña, M. V., Weaver, B. A., Wechsler, R., Zhou, Z., and Zou, H. (2025). DESI Peculiar Velocity Survey – Fundamental Plane. *Monthly Notices of the Royal Astronomical Society*, 539(4):3627–3644. doi:10.1093/mnras/staf700. arXiv:2408.13842.

Schöneberg, N., Lesgourgues, J., and Hooper, D. C. (2019). The BAO+BBN take on the Hubble tension. *Journal of Cosmology and Astroparticle Physics*, 2019(10):029. doi:10.1088/1475-7516/2019/10/029. arXiv:1907.11594.

Schutz, B. F. (1986). Determining the Hubble Constant from Gravitational Wave Observations. *Nature*, 323:310–311. doi:10.1038/323310a0.

Schutz, B. F. (2009). *A First Course in General Relativity*. Cambridge University Press, 2nd edition. doi:10.1017/CBO9780511984181.

Scolnic, D., Brout, D., Carr, A., Riess, A. G., Davis, T. M., Dwomoh, A., Jones, D. O., Ali, N., Charvu, P., Chen, R., Peterson, E. R., Popovic, B., Rose, B. M., Wood, C., Brown, P. J., Chambers, K., Coulter, D. A., Dettman, K. G., Dimitriadis, G., Filippenko, A. V., Foley, R. J., Jha, S. W., Kilpatrick, C. D., Kirshner, R. P., Pan, Y.-C., Rest, A., Rojas-Bravo, C., Siebert, M. R., Stahl, B. E., and Zheng, W. (2022). The Pantheon+ Analysis: The Full Dataset and Light-Curve Release. *The Astrophysical Journal*, 938(2):113. doi:10.3847/1538-4357/ac8b7a. arXiv:2112.03863.

Simon, J., Verde, L., and Jimenez, R. (2005). Constraints on the Redshift Dependence of the Dark Energy Potential. *Physical Review D*, 71:123001. doi:10.1103/PhysRevD.71.123001. arXiv:astro-ph/0412269.

Slipher, V. M. (1917). Nebulae. *Proceedings of the American Philosophical Society*, 56(7):403–409.

Stern, D., Jimenez, R., Verde, L., Kamionkowski, M., and Stanford, S. A. (2010). Cosmic Chronometers: Constraining the Equation of State of Dark Energy. I: $H(z)$ Measurements. *Journal of Cosmology and Astroparticle Physics*, 2010(02):008. doi:10.1088/1475-7516/2010/02/008. arXiv:0907.3149.

Stiskalek, R., Desmond, H., Mazurenko, S., and Banik, I. (2025). Testing the local supervoid solution to the hubble tension with direct distance tracers. *arXiv preprint*. doi:10.48550/arXiv.2506.10518. arXiv:2506.10518.

Szigeti, B. E., Szapudi, I., Barna, I. F., and Barnaföldi, G. G. (2025). Can rotation solve the Hubble Puzzle? *Monthly Notices of the Royal Astronomical Society*, 538(4):3038–3041. doi:10.1093/mnras/staf446. arXiv:2503.13525.

Toda, Y. and Seto, O. (2025). Constraints on the simultaneous variation of the fine-structure constant and electron mass in light of DESI BAO data. *arXiv preprint*. doi:10.48550/arXiv.2504.09136. arXiv:2504.09136.

Tomasetti, E., Moresco, M., Borghi, N., Jiao, K., Cimatti, A., Pozzetti, L., Carnall, A. C., McLure, R. J., and Pentericci, L. (2023). A New Measurement of the Expansion History of the Universe at $z = 1.26$ with Cosmic Chronometers in VANDELS. *Astronomy & Astrophysics*, 679:A96. doi:10.1051/0004-6361/202346992. arXiv:2305.16387.

Tripp, R. and Branch, D. (1998). Determination of the Hubble Constant Using a Two-Parameter Luminosity Correction for Type Ia Supernovae. *Astronomy & Astrophysics*, 331:815–820. doi:10.1086/307883. arXiv:astro-ph/9904347.

Uddin, S. A., Burns, C. R., Phillips, M. M., Suntzeff, N. B., Freedman, W. L., Brown, P. J., Morrell, N., Hamuy, M., Krisciunas, K., Wang, L., Hsiao, E. Y., Goobar, A., Perlmutter, S., Lu, J., Stritzinger, M., Anderson, J. P., Ashall, C., Hoeflich, P., Shappee, B. J., Persson, S. E., Piro, A. L., Baron, E., Contreras, C., Galbany, L., Kumar, S., Shahbandeh, M., Davis, S., Anais, J., Busta, L., Campillay, A., Castellón, S., Corco, C., Diamond, T., Gall, C., Gonzalez, C., Holmbo, S., Roth, M., Serón, J., Taddia, F., Torres, S., Baltay, C., Folatelli, G., Hadjiyska, E., Kasliwal, M., Nugent, P. E., Rabinowitz, D., and Ryder, S. D. (2023). Carnegie Supernova Project-I and -II: Measurements of H_0 Using Cepheid, TRGB, and SBF Distance Calibration to Type Ia Supernovae. *The Astrophysical Journal*, 970(1):1–29. doi:10.3847/1538-4357/ad3e63. arXiv:2308.01875.

Verma, A., Aluri, P. K., Mota, D. F., and Obukhov, Y. N. (2025). Cosmographic constraints on a Gödel-type rotating universe. *arXiv preprints*. doi:10.48550/arXiv.2506.00860. arXiv:2506.03045.

Viets, A. D. e. a. (2018). Reconstructing the calibrated strain signal in the Advanced LIGO detectors. *Classical and Quantum Gravity*, 35:095015. doi:10.1088/1361-6382/aab658. arXiv:1710.09973.

Visser, M. (2004). Jerk, snap, and the cosmological equation of state. *Classical and Quantum Gravity*, 21(11):2603–2615. doi:10.1088/0264-9381/21/11/006. arXiv:gr-qc/0309109.

Vitale, S. and Chen, H.-Y. (2018). Measuring the Hubble Constant with with Neutron Star Black Hole Mergers. *Physical Review Letters*, 121:021303. doi:10.1103/PhysRevLett.121.021303. arXiv:1804.07337.

Vogl, C., Taubenberger, S., Csörnyei, G., Leibundgut, B., Kerzendorf, W. E., Sim, S. A., Blondin, S., Flörs, A., Holas, A., Shields, J. V., Spyromilio, J., Suyu, S. H., and Hillebrandt, W. (2025). No rungs attached: A distance-ladder free determination of the Hubble constant through type II supernova spectral modelling. *Astronomy & Astrophysics*. doi:10.1051/0004-6361/202452910. arXiv:2411.04968. in press.

Wan, J. T., Mantz, A. B., Sayers, J., Allen, S. W., Morris, R. G., and Golwala, S. R. (2021). Measuring H_0 Using X-ray and SZ Effect Observations of Dynamically Relaxed Galaxy Clusters. *Monthly Notices of the Royal Astronomical Society*, 504(2):1900–1916. doi:10.1093/mnras/stab948. arXiv:2101.09389.

Weinberg, Steven (1971). *Gravitation And Cosmology.. Principles And Applications Of The General Theory Of Relativity*. John Wiley & Sons, New York.

Ye, G. and Lin, S. (2025). On the tension between DESI DR2 BAO and CMB in ΛCDM. *arXiv e-prints*. doi:10.48550/arXiv.2505.02207. arXiv:2505.02207.

Zhang, C., Zhang, H., Yuan, S., Liu, S., Zhang, T., and Sun, Y. (2014). Four New Observational $H(z)$ Data From Luminous Red Galaxies of Sloan Digital Sky Survey Data Release Seven. *Research in Astronomy and Astrophysics*, 14(10):1221–1233. doi:10.1088/1674-4527/14/10/002. arXiv:1207.4541.

Zhou, Z., Miao, Z., Bi, S., Ai, C., and Zhang, H. (2025). What Prevents Resolving the Hubble Tension through Late-Time Expansion Modifications? *arXiv e-prints*. doi:10.48550/arXiv.2506.23556. arXiv:2506.23556v1.